Elucidating the Role of Two Inotropic Agents in Cardiac Hypertrophy: the Ceramides and Apelins

Alexandra M. Wiley

A dissertation

submitted in partial fulfillment of the

requirements for the degree of

Doctor of Philosophy

University of Washington

2024

Reading Committee:

Rheem A. Totah, Chair

Qinghang Liu

Allan E. Rettie

Program Authorized to Offer Degree:

Medicinal Chemistry

University of Washington

Abstract

Elucidating the Role of Two Inotropic Agents in Cardiac Hypertrophy: the Ceramides and Apelins

Alexandra M. Wiley

Chair of the Supervisory Committee:
Rheem A. Totah
Department of Medicinal Chemistry

The steady increase in prevalence of cardiovascular diseases (CVDs) globally, necessitates the urgent identification of novel druggable targets to reduce the development and progression of CVD. The inotropic agents, the ceramides and apelins, represent two potential druggable targets that influence cardiovascular function. In this dissertation, we examined the impact of silencing the ceramide synthases (*CERS*) responsible for the production of the putative protective very long-chain (VLC) ceramides 22:0 and 24:0 (*CERS2*) and detrimental long-chain (LC) 16:0 ceramide (*CERS5/6*) on cardiomyocyte health and induced hypertrophy. In this work, we demonstrate that the VLC and LC ceramides play contrasting roles in cardiomyocyte health. The

silencing of *CERS2* in healthy cardiomyocytes leads to pathway changes indicative of a decline in cardiomyocyte health, while *CERS2* knockdown (KD) in cardiomyocytes subjected to hypertrophic conditions displayed an exacerbated response. Interestingly, transcriptional changes in healthy cardiomyocytes with silenced *CERS5/6* resulted in pathway changes suggesting improved cardiomyocyte health, while the hypertrophic response in cardiomyocytes with *CERS5/6* KD appeared tempered compared to controls. These findings suggest that VLC ceramides may be protective against CVD progression, while LC ceramides may contribute to the progression of CVD. Additionally, we probed how the different components of the apelinergic system (AS) affect both healthy cardiomyocytes and cellular hypertrophy progression. Here we show that both the apelin receptor (APJ) and apelin are necessary to elicit a protective response against cardiac hypertrophy, as well as identify many hypertrophic response changes due to the addition of the various AS components. To conclude this project, we present the development of a potential technique to enable the high-throughput screening of compounds against GPCR targets, such as APJ. We discuss the utilization of virus-like particles (VLPs) overexpressing APJ and demonstrate the ability to enrich the binding of positive control apelin, in both simple and complex mixtures containing a mock screening library with over 2500 peptides. The work in this thesis provides mechanistic insight into the impact the ceramides and apelins have on the progression of hypertrophy and proposes a unique technique that can be utilized to more efficiently generate future therapeutics targeting APJ and other GPCRs.

TABLE OF CONTENTS

LIST OF FIGURES

LIST OF ABBREVIATIONS

Abbreviation	Definition
A2A	Adenosine A2a receptor
AA	Amino acid
AC	Adenylyl cyclase
ACE	Angiotensin-converting enzyme
ACE2	Angiotensin-converting enzyme 2
ACTA2	Actin alpha 2 (gene name)
ADORA2A	Adenosine A2a receptor
AKT	Protein kinase B
AngII	Angiotensin II
ANKRD1	Ankyrin repeat domain 1 (gene name)
AP-13	Apelin-13 (13 residues)
AP-77	Preproapelin (77 residues)
APELA	Elabela (gene name)
APLN	Apelin (gene name)
APLNR	APJ (gene name)
ARBs	Angiotensin receptor blockers
AS	Apelinergic system
ASMS	Affinity selection mass spectrometry
AT1	Angiotensin II type-1 receptor
BNP	B-type natriuretic peptide
BSA	Bovine serum albumin
CA	Capsid protein
cAMP	Cyclic adenosine monophosphate
CCK	Cholecystokinin
CCKR	Cholecystokinin receptor
CerS	Ceramide synthase (enzyme)
CERS	Ceramide synthase (gene)
CHS	Cholesteryl-hemisuccinate
CM	Cardiomyopathy
CREB1	cAMP response element binding protein 1
cryo-EM	Cryogenic electron microscopy
CVD	Cardiovascular disease
DDM	N-dodecyl-β-D-maltoside
DEG	Differentially expressed gene
DIA	Data independent acquisition
DMEM	Dulbecco's Modified Eagle's Medium
DMPG	1,2-dimyristoyl-*sn*-glycero-3-PG
DMSO	Dimethyl sulfoxide
ECM	Extracellular matrix
EM	Electron microscopy
ER	Endoplasmic reticulum
FA	Fatty acid

FBS	Fetal bovine serum
FDR	False discovery rate
FITC-AP-13	Fluorescein isothiocyanate labeled apelin-13
GalCer	Galactosylceramide
GDP	Guanosine diphosphate
GlcCer	Glucosylceramide
GnHCl	Guanidine hydrochloride
GPCR	G protein-coupled receptor
GSEA	Gene set enrichment analysis
GTP	Guanosine triphosphate
HCM	Human cardiomyocytes
HEK293T	Human embryonic kidney 293T
HexCer	Hexosylceramide
HF	Heart failure
HPLC-MS/MS	high-performance liquid chromatography - tandem mass spectrometry
HTS	High-throughput screening
KD	Knockdown
LacCer	Lactosylceramide
LC	Long-chain
LDL	Low density lipoprotein
LDLR	Low density lipoprotein receptor (gene name)
LRT	Likelihood ratio rest
MA	Matrix protein
MAPK	Mitogen-activated protein kinase
MEF2	Myocyte enhancer factor 2
MRM	Multiple reaction monitoring
MS	Mass spectrometry
MTBE	Methyl tert-butyl ether
NC	Nucleocapsid protein
NPPB	B-type natriuretic peptide (gene name)
ns-EM	Negative-stain electron microscopy
ORF	Open reading frame
OXPHOS	Oxidative phosphorylation
PAR	Peak area ratio
PBS	Phosphate buffered saline
PCA	Principal component analysis
PKA	Protein kinase A
PKC	Protein kinase C
PLIN2	Perilipin 2 (gene name)
PMA	Phorbol 12-myristate 13-acetate
PS	Protamine sulfate
PTGS2	Prostaglandin-endoperoxide synthase 2 (gene name)
PTMs	Post translational modifications
pyr-AP-13	Pyroglutamyl-apelin-13

RAS	Renin-angiotensin-system
RED	Rapid equilibrium dialysis
RLU	Relative light units
ROS	Reactive oxygen species
SF	Serum free
SM	Sphingomyelin
SNAP-APJ	SNAP-tagged APJ
SP1	Spacer peptide 1
SP2	Spacer peptide 2
SREBP	Sterol regulatory element-binding proteins
STC2	Stanniocalcin 2 (gene name)
TCA	Tricarboxylic acid
VEH	Vehicle
VLC	Very long-chain
VLPs	Virus-like particles

ACKNOWLEDGEMENTS

Somehow, I am finding this section the most difficult to write. To put into words the meaning of all the support I've received over the last 5 years seems to do it a disservice, but here is my attempt at expressing my sincerest appreciation – I thank you with my entire being.

To my graduate student advisor, Dr. Rheem Totah. Wow has it been a fantastic ride. There is so much that I could say, but all of it seems inadequate. Thank you for always supporting me in the way I needed, instead of the way I wanted. Thank you for pushing me to pursue the hard things, and for giving me the skills to make those things possible. Thank you for helping me reach my potential. If I could go back in time I would do it all over again. I hope that you always have beautiful avocados.

To my committee. It takes a village, and I sure surrounded myself with a wonderful one. To Allan Rettie and Qinghang Liu; thank you both for supporting my projects and for providing guidance on how to improve my thesis. To Bill Atkins, Cathy Yeung, and Gaurav Bhardwaj; thanks for the hard questions during our committee meetings and for pushing me to really think beyond my current boundaries. You always made me feel immeasurably supported. Thank you for always being on my team.

To my lab mates, for helping laugh away all the failures. To Christi Cho and Eric Evangelista for helping shape me into the scientist I am today. To Max Zeigler for being a steady and calming presence in the lab, and for always having answers to mass spec related questions. To Drake Russell for the endless laughs. My journey the last two years would not have been the same without you. Thank you for all your experimental insight and for your constant love of

science, it is so great to have a constant in this world full of variables. Now to Jade Yang, thank you for being a ray of sunshine in the lab, and for being a good friend. To Marvin Chau, Taeyoon Jung, Megan Ling, Harrison Hu, and Ian Levasseur, I can't wait to see what the future holds for all of you, thank you for being a part of my journey. Also thank you to all the undergraduate students who I crossed paths with in the lab, I wish you all the best with your future studies and it was great working with you.

To the Departments of Medicinal Chemistry and Pharmaceutics; thank you for always being so friendly and collaborative. To Sarah Lenti for always going the extra mile for the students, it didn't go unnoticed. To Helen Kim, for the great conversations and for all the hard work when it came to tracking down my missing packages. To Robin, Julia, and Erik for all the support and guidance throughout the years.

To my family for always being my biggest support system. To my mom, Lisa Wiley, for always encouraging me to pursue my dreams. Thank you for your constant support. To my grandma Nene (Marie Wild), for always thinking of me and loving me. Your cards helped me push through the hardest days. To my brother, Jared Wiley, for the silly games and goofy chats. Thank you for always keeping my spirits high. To my dad, Matt Wiley, for talking me through all the Thursday Spirals, even if they happened on a Wednesday. Thank you for always knowing what to say.

To my friends for always filling my bucket. To my best friend Claire, thank you for the constant support and for so much more than that. I don't know that I would have gotten through this without you. Thank you for accepting me as the truest version of myself. To my Seattle friends, the Hogs, for always reminding me that there is so much more to focus on than work. Thank you for pushing me to get out of the lab and enjoy every day. Also, to every other friend

who thought of me and checked in. The amount of support I received was unmatched, and I am so grateful for all the people who make up my web.

To Jonathan Palmer, misery loves company. I wouldn't have changed our journey for anything. Thank you for being an automatic friend to work through homework sets and complain about cumulative exams with. On the work side of things, I am so glad that we got to intertwine our skill sets to come up with a really cool project. Thank you for always having such a positive outlook when our GPCR experiments failed and failed again. On the personal side of things, you have truly become a lifelong friend. Thank you for always being a listening ear and for all the laughs. I'm grateful for Season 1 especially, but for every Season after that as well. You were my first friend in Seattle and for that you will always hold a special place in my heart. Thank you for always being unapologetically yourself.

To my cat, Hans, who sits on my lap as I write this. Thank you for bringing joy to each and every day. Thank you for being my home IT, meeting greeter, and scheduler. Thank you for all the love and laughs. You deserve an honorary doctorate.

To some random things that helped make every day better. To Book Outlet, for having a marvelous sale as I was completing my thesis. This gave me the gift of being able to bribe myself into continuing to write. To great music, for the midday jams to help reset. To my Ninja Thirsti, for giving me a sparkling water treat every afternoon to help me keep going.

And finally, to myself. You did it. You are a B.A.B. You are stronger and more resilient than you ever thought you could be. After this anything is possible – time to find a unicorn.

DEDICATION

To my dad, Matt Wiley, for constantly reminding me:

'If it was easy, everyone would do it.'

Chapter 1: Introduction

1.1 Dissertation purpose

The primary objective of this thesis is to determine the effects of two groups of unique inotropic agents on the development of cardiac hypertrophy. The first inotropic group consists of the ceramides, a diverse lipid class whose members are proposed to be associated with the risk of incident heart failure. The second inotropic agents are the apelins, a group of signaling peptides that bind to and activate a G protein-coupled receptor known as APJ in the heart and have protective properties on overall cardiac health. Both the ceramides and apelins are known to play crucial functions in various organs including the heart. We will determine the importance of these two distinct inotropic agents in maintaining the homeostasis of healthy ventricular cardiomyocytes and cardiomyocytes subjected to conditions that induce hypertrophy. The long-term purpose of this dissertation is to identify novel druggable targets related to the ceramides or apelins that would prevent or treat cardiac hypertrophy. To begin to tackle this issue with respect to targeting the apelinergic system, we also present a universal approach that is suitable for screening compounds to identify APJ binders, or other G protein-coupled receptor (GPCR) binders in the future.

1.2 The impact of cardiovascular disease on global health and current biomarkers

Between 2016 – 2019, cardiovascular diseases (CVDs) accounted for roughly one-third of all deaths worldwide, making CVD the leading cause of global morbidity and mortality (1). The proportion of deaths and disabilities due to CVD has been steadily rising across the globe over the past 30 years (1,2) driving a growing urgency to discover and study novel therapeutic targets to combat the rise of CVD and its devastating effect on the quality of life.

Clinical outcomes in patients with CVD witnessed significant improvement with the discovery and development of aspirin, statins, β-blockers, ACE (angiotensin-converting enzyme) inhibitors, and ARBs (angiotensin receptor blockers) (3,4) and highlighted the importance of medical intervention during the development of CVD. Preventive strategies to help minimize risk factors such as hypertension and high cholesterol have been met with major health benefits. Currently, LDL (low density lipoprotein) cholesterol and blood pressure are qualified by the FDA to serve as two of the primary biomarkers for chronic CVD risk, yet these biomarkers are less than ideal as they may have paradoxical effects differing between the time period before and after the onset of CVD (5,6). Additionally, an ideal biomarker is one that falls along the causal path to most correctly reflect disease outcome (6). With this in mind, LDL cholesterol falls into the category of an associated biomarker, indicating that although treatment to lower LDL cholesterol levels may lead to a lower CVD risk it is not always representative of overall survival or quality of life (6). Presently, the natriuretic peptides are the gold standard biomarkers for heart failure (HF), with B-type natriuretic peptide (BNP) representing the most clinically recognized biomarker. BNP levels have been correlated with other measures of cardiac status and HF disease severity and are a strong predictor of risk of adverse cardiac events and death (7). However, the shortcoming of measuring BNP levels is that it rises as the heart becomes stressed, so while BNP level is a suitable indicator of heart disease, it fails to predict the onset of HF. Hence, efforts to identify a clinically relevant biomarker capable of detecting increased risk of CVD before the onset of disease symptoms is timely and necessary, as is elucidating the mechanisms leading to CVD predicted by these potential biomarkers.

While many different agents have been identified as potential biomarkers for CVD progression, there are two that hold immense promise, the ceramides and apelins. Both of these

agents are endogenously expressed, and it is proposed that their plasma levels may correlate with CVD disease progression (8–10). Both ceramides and apelins are signaling inotropic agents. Inotropic agents, such as digoxin and dobutamine, alter the heart's contractility, while chronotropic agents, like atropine and β-blockers, affect heart rate. The ceramides are a class of signaling lipids, while the apelins are a class of signaling peptides. These two targets represent potential druggable and modifiable systems that may be able to report both on the increased risk of incident CVD prior to the onset of disease and to provide avenues for future novel therapeutic design.

1.3 Ceramides: Introduction

1.3.1 Ceramide structure and physiological function

Ceramides fall within the lipid class known as sphingolipids. Sphingolipids are a group of structurally diverse lipids that share a sphingoid base backbone which is N-acylated to fatty acids of various chain lengths (**Figure 1.1**). Within this lipid class, there are three distinct structural subclasses – sphingoid bases and derivatives, ceramides, and complex sphingolipids – of which, ceramides represent the central essential precursor of complex sphingolipids (11). Sphingolipids are amphipathic and as such control many vital cellular functions. Structurally, sphingolipids are crucial components of the plasma membrane, and also contribute to more complex biological roles as bioactive signaling molecules that regulate intercellular interactions, cell proliferation, migration, and cell death, to name a few (12,13). These bioactive molecules are central mediators in several highly complex and interconnected pathways integral to cell function although the exact mechanisms by which they maintain cellular homeostasis are not completely elucidated.

Since sphingolipids play a pivotal role in homeostasis, any disruption or dysregulation in sphingolipid utilization and metabolism may result in detrimental pathophysiological conditions

(14). As ceramides are crucial intermediates in the biosynthesis of complex sphingolipids such as sphingomyelin (SM) and glycosphingolipids, understanding the role ceramides play in homeostasis is important. Notably, ceramides have previously been studied and identified as major regulators in cell death, primarily by arresting the cell cycle thus inhibiting growth, and causing apoptosis (15). Furthermore, many studies suggest a correlation between ceramides and mitochondrial membrane permeabilization, wherein elevated cellular ceramide levels lead to the release of caspases into the cytosol to activate apoptotic pathways (16,17). In general, ceramides are present at low levels within membranes due to their exceptional hydrophobicity, but under conditions of stress, ceramide accumulation in the membrane is postulated to impair membrane dynamics (13,18). As a result, ceramide concentrations in the cell are tightly regulated (14).

Within the sphingolipid metabolic scheme, there are three major pathways that lead to the synthesis of ceramides – the *de novo* pathway, sphingomyelinase pathway, and salvage pathway (**Figure 1.2**) (19,20). Importantly, ceramides generated by any of these pathways are thought to be both spatially and functionally distinct from each other (20). Hydrolysis of SM by sphingomyelinases in the cell membrane may contribute to circulating ceramide and SM levels (21,22). Additionally, circulating sphingolipids are carried by lipoprotein particles and circulating concentrations of sphingolipids may represent a systemic metabolic signature that reflects overall homeostasis (23,24). Today, LDL cholesterol levels represent one of the best predictors for CVD risk, but there is evidence to suggest that plasma ceramides may be more accurate predictors than LDL cholesterol (10,25,26). The Mayo Clinic Laboratories have begun quantifying plasma ceramides to estimate the risk for adverse cardiovascular events. Four different ceramides are measured, ceramides 16:0, 18:0, 24:0, and 24:1, with ceramides 24:0 serving as a normalization factor to account for intra-individual ceramide concentration

variability (27). Although there is an extensive body of literature to support the role of cholesterol in HF, substantial experimental work is needed to understand the role of ceramides in HF disease progression.

1.3.2 Ceramides with variable fatty acid chains have specific functions and are synthesized by different enzymes

There is experimental evidence to suggest that ceramide species with specific saturated fatty acids have distinct biological activities (28). Although we have referred to ceramides thus far as a group, it is important to note that there are over 50 distinct molecular ceramide species, distinguished by their unique acyl chain length, the number and location of hydroxyl groups, and desaturations (13). Additionally, there are at least 26 different enzymes in which ceramides serve as either a substrate or a product, that regulate ceramide levels as well as alter their concentrations and metabolites throughout the cell or body in response to stimuli (13). Ceramide synthases (CerS) are a group of enzymes that reside in the endoplasmic reticulum and are important gatekeepers of ceramide levels. There are six mammalian ceramide synthases (CerS1-6), with each CerS displaying substrate preferences for specific fatty acid chain lengths, resulting in different acyl length ceramides (**Figure 1.3B**) (29–34). In terms of genetic variants of the different ceramide synthases UniProt provides 441, 355, 452, 549, 336, and 377 variants for *CERS1*, *CERS2*, *CERS3*, *CERS4*, *CERS5*, and *CERS6*, respectively (35). Interestingly, none of these variants have been identified as being benign and a few have been directly connected to sphingolipid dysregulation in different disease states such as epilepsy and ichthyosis (35). Two variants of *CERS3* and two variants of *CERS6* have been clinically correlated with elevated plasma ceramides and dihydroceramides in individuals with metabolic syndrome (36), suggesting that alterations in the different CerS can have negative impacts on health.

In general, long-chain (LC) ceramides 16:0 and 18:0 are thought to drive metabolic dysfunction and high levels have been associated with the development or progression of different disease states including diabetes, heart failure, and Alzheimer's disease, while very long-chain (VLC) ceramides including 22:0 and 24:0 have been suggested to be either beneficial or benign (20,34,37–39) depending on cell state. A global *Cers5* knockout mouse demonstrated decreased tissue 16:0 ceramide levels and resulted in reduced insulin insensitivity and glucose intolerance when challenged with a high-fat diet (40). Similarly, knocking out *Cers6* (also responsible for the production of 16:0 ceramide) was protective against glucose intolerance in mice fed a high-fat diet (41). Additionally, Lee et al. reported lower concentrations of 20:0, 24:0, and 24:1 ceramides and increased levels of apoptosis in mice with a cardiomyocyte specific *Sptl2* (rate-limiting step in *de novo* ceramide synthesis) knockout (42). Thus far there has been little *in vitro* and *in vivo* work completed to aid in better understanding the physiological roles the specific ceramide species play in heart failure or cardiac hypertrophy.

1.3.3 Therapies targeting sphingolipid metabolism

In the century between the discovery of sphingolipids in 1874 and the finding that sphingosine contributes to biological activities in 1986, it was thought that sphingolipids were only structural components of cellular membranes (43–45). Since then, targeting sphingolipid metabolism for novel therapies has been a growing research area, especially in terms of anticancer therapeutics. Currently, there are many available pharmacological inhibitors targeting different sphingolipids enzymes that allow for increased characterization of the role specific sphingolipids plays in disease (46). For this dissertation, we will be focusing solely on inhibitors that play a direct role in ceramide homeostasis. Fumonisins B_1, B_2, and B_3 are known mycotoxins that potently inhibit all six of the mammalian CerS enzymes (46,47). Fumonisin

exposure has a negative impact on many different biological processes including mitochondrial function, controlled cell growth, and altered immune function, suggesting that the inhibition of all CerS enzymes is detrimental to cell health (47). The identification and discovery of P053, the first isoform-specific CerS inhibitor, lead to a study that helped define the endogenous role for CerS1, as a regulator of adiposity and inhibitor of mitochondrial fatty acid oxidation (48). Outside of compounds that directly interact with the CerS enzymes, there are many inhibitors that target sphingomyelinases and ceramidases, that inhibit the cleavage of SM to ceramide, and the degradation of ceramide, respectively (43,46).

To date, it appears sphingolipid metabolism has primarily been targeted as a therapeutic strategy in cancer treatment. Many studies have shown that ceramides induce cancer cell death, but due to their intrinsic toxicities and poor pharmacokinetic properties, treatment with ceramides alone does not serve as a viable chemotherapeutic option (46,49). In terms of CVD, targeting sphingolipid metabolism has immense therapeutic potential, but this approach has yet to identify any compound that mediates its effects through direct interactions with the CerS enzymes. Intriguingly, there have been many studies completed on quantifying sphingolipids in human plasma to investigate if specific sphingolipids correlate with risk of adverse cardiac events (10,50–53), but there is a significant gap in knowledge when it comes to a mechanistic understanding of the role these identified sphingolipids play in the development and progression of CVD. One of the goals of this dissertation project is to explore the role CerS enzymes play *in vitro* in order to identify the contributions of the different ceramide species in the development of human cardiac hypertrophy. This novel work will help researchers better understand the potential impact of targeting specific CerS with future CVD therapies.

1.4 The Apelinergic System: Introduction

1.4.1 Components, synthesis, and physiological function

The apelinergic system (AS) is a multifaceted signaling system that regulates many essential physiological processes throughout the body, especially in the cardiovascular system. The AS influences almost all crucial bodily functions, ranging from fluid homeostasis to angiogenesis, energy metabolism, inflammation, and pain management (54–58). The AS is linked to a number of pathological conditions such as heart failure, diabetes, and obesity, and has been probed as a potential druggable target for these conditions (54,55,57). In terms of heart failure, rat models with left ventricular hypertrophy and secondary HF showed downregulated expression of the AS (59). In a second study researchers identified markedly reduced apelin mRNA and protein expression in dogs with advanced chronic HF, as well as showed that exogenous addition of apelin significantly improved left ventricular systolic function (60). Depending on the CVD type, there is contradictory evidence in the literature as to whether expression of the AS increases or decreases, and this could be due to the complexities involved in AS regulation and activation. Although there is increasing interest in understanding the physiology of the AS due to its potential druggability, research in this area is difficult and complex due to challenges in expressing a functional receptor and the intricacies of the activation of multiple different signaling cascades by the endogenous ligands in several organs and in different disease states (56,57,61). With the growing evidence that the AS is a critical mediator of cardiovascular homeostasis, we believe that comprehensive mechanistic work will be crucial to help understand the druggability profile of the AS.

The AS is composed of three unique entities: a single G protein-coupled receptor, APJ, and two peptide ligands, apelin and elabela, each existing in multiple bioactive isoforms

throughout the body (**Figure 1.4**) (56,62). Apelin is a vasoactive peptide that lowers arterial blood pressure, improves cardiac output, and has been shown to be one of the most potent endogenous positive inotropic agents (63–65). Elabela on the other hand, is essential for heart development. *Apela* (gene name for elabela) knockout in zebrafish proved lethal, due to either rudimentary or absent heart formation (66). With the exception of the kidney, it has been shown that *Apela* expression is maximally detected in the early embryonic phase, but through the different developmental phases, *Apela* expression decreases (66–69), for this reason, we will be focusing mainly on apelin and APJ for the remainder of this dissertation.

Both APJ and apelin are widely expressed in many tissues including the heart, endothelium, vascular smooth muscle cells, and adipose (70). The apelin gene, *APLN*, located on the X-chromosome, encodes a preproprotein with 77 amino acids that contains very low levels of activity as well as low levels of genetic variability (56). It is unclear whether dimerization of apelin is a prerequisite step for proper processing, as is the case with other preproproteins like somatostatin-II (71), but due to the finding that only the dimeric form of preproapelin was observed in mice *in vivo* there is reason to believe this is the case (72). It is thought that the 77 residue preproapelin is comprised of a 22-residue secretory signal peptide on the N-terminus, and a C-terminal domain containing a 55 amino acid proprotein (73). Processing of the apelin isoforms is complex, but it is thought apelin isoform synthesis is dependent on the active proteases in the environment, leading to tissue and organ specific apelin isoforms (56). Notably, all apelin isoforms are active, but the shorter isoforms such as apelin-36, -17, and -13, which contain the respective number of amino acids, are thought to be more active (74). Apelin-13 can undergo post translational modification to pyroglutamyl-apelin-13 (pyr-AP-13), and this apelin isoform may represent the predominant form in both the heart and plasma (75,76). Hydrolysis of

the C-terminal phenylalanine of all apelin isoforms by ACE2 (angiotensin-converting enzyme 2) serves as the apelin deactivation pathway and is perhaps the main contributor to the short half-lives (5-8 min) observed for all apelin peptides in circulation (76,77). Computational modeling predicted that this phenylalanine may provide a key apelin-APJ pi-stacking interaction, and mutagenesis studies have shown that alterations in this interaction could alter downstream signaling (76).

Additionally, it is well known that the AS antagonizes the renin-angiotensin-system (RAS), which is the key regulator of blood pressure and overactivity of the RAS is a trigger for cardiovascular dysfunction (78). Angiotensin II signaling can lead to cardiac injury through increased oxidative stress and fibrosis, and decreased heart contractility, while it is thought that APJ signaling counters all of these physiological responses following APJ activation with apelin (79). There are two key enzymes in RAS activation; ACE converts the inactive angiotensin I to the active angiotensin II, and serves as a positive regulator of the RAS, while ACE2 serves as a negative regulator of the RAS by catalyzing the hydrolysis of angiotensin II. Elabela can inhibit ACE (80), while apelin can induce ACE2 (79), both of which result in protection against angiotensin signaling (**Figure 1.5**). Finally, APJ and AT1 (angiotensin II type-1 receptor) can form an apelin-dependent heterodimer, promoting negative allosteric regulation of AT1 function (81). Taken together, in general the AS counters the RAS.

Several rodent models have presented promising data suggesting that apelin can alleviate cardiac hypertrophy, fibrosis, pulmonary arterial hypertension, heart failure, and myocardial infarctions (61,79). Multiple studies have shown that plasma apelin levels appear to increase in early stages of heart failure, but as the disease progresses in severity, apelin levels decrease compared to those in healthy patients, suggesting that apelin may serve as a biomarker for CVD

progression (8,9,82,83). Intravenous administration of pyr-AP-13 increases cardiac output, reduces blood pressure, and reduces peripheral vascular resistance in both healthy individuals and patients with HF (65). In the same study, all but one patient with HF was on either ACE inhibitors or angiotensin blockers suggesting that apelin also plays a role independent of RAS signaling (65). This discovery increases the potential promise of a drug targeting the AS, as this opens an avenue for pharmacological synergism through APJ agonism and inhibition of the RAS.

1.4.2 APJ activation and signaling

Before diving into the specifics of APJ signaling, it is important to address some important generalizations in GPCR signaling. GPCRs are the largest superfamily of membrane bound proteins (84). They have historically been highly successful drug targets due to the fact that they span a large range of physiological functions and lie on the cellular surface, eliminating the issue of drug delivery inside the cell (84). With respect to the G protein, GPCRs are composed of three distinct subunits (α, β, and γ), and a GPCR is functionally classified depending on its associated Gα subunit. There are four families and each family leads to the activation of different signaling cascades (85). To make matters more complex, there are multiple subtypes of Gα subunits within each family that can also modulate signaling responses (**Figure 1.6**) (85,86). Additionally, it is common that GPCRs are associated with multiple Gα subunit families (85,87), meaning that activation with different agonists or with the same agonist under different conditions, can elicit very different signaling responses. It is also important to note that as GPCRs are activated, the Gα subunit releases guanosine diphosphate (GDP) and binds guanosine triphosphate (GTP), then dissociates from the membrane-bound Gβγ dimer. This enables signaling to various cellular pathways with these two separate functional units – Gα and Gβγ (85,88).

In addition to G protein signaling, ligands can also elicit a β-arrestin response. While each GPCR is unique and not all follow this rule, in general G protein activation leads to physiological responses, while β-arrestin activation leads to desensitization and receptor internalization (89). GPCR internalization typically has a negative connotation, but it is a critical regulatory component that has been shown to have a strong connection to prolonged signaling (90), and therefore plays a very important role that is often under appreciated. In terms of drug development, ligands can be biased to activate G protein or β-arrestin signaling (91). Agonists acting on a GPCR can be engineered to stabilize different conformational states and function as biased ligands to elicit the desired downstream signaling while minimizing unwanted side effects (92). The explanation of all of this serves to make one very important point: agonists can act on the same GPCR, but elicit very different signaling responses (54,56), and understanding the physiology of these responses improves the druggability profile of a GPCR system.

Signaling through the AS is very complex since APJ has been shown to associate with three of the four Gα families: $G\alpha_i$, $G\alpha_q$, and $G\alpha_{12/13}$ (**Figure 1.7**) (93). This may explain why the AS can have different physiological functions within the body. APJ mediated $G\alpha_i$ signaling can lead to inhibition of adenylyl cyclase (AC), which is responsible for the production of cAMP (cyclic adenosine monophosphate) and activation of protein kinase A (PKA). cAMP is an important intracellular second messenger in GPCR signaling and is one of the most common assay choices for studying GPCR functionality, though it is not without flaws (94). Through $G\alpha_i$ and $G\alpha_q$ signaling, activation of protein kinase B (AKT), protein kinase C (PKC), and mitogen-activated protein kinase (MAPK) have been detected (93). Additionally, $G\alpha_{12/13}$ signaling results in the activation of MEF2 (myocyte enhancer factor 2) transcription factors which play an imperative role in cardiomyocyte development and differentiation (95,96). While these are the G

protein responses, it is important to also consider that APJ mediated β-arrestin responses can lead to receptor internalization and downregulation of the AS (93,97). APJ is prone to agonist-induced internalization leading to either recycling of the receptor back to the cell surface or degradation by lysosomes, depending on the apelin isoform (97). Taken together, the multiple signaling cascades activated after stimulation of APJ leads to complexity in studying this system. It is important to be aware of the pharmacological differences between G protein and β-arrestin activation, as well as the intricacies of APJ internalization while thinking about the role the AS plays on disease states.

1.4.3 The importance of targeting APJ

In 2015, Brame et al. designed cyclic peptide MM07 (half-life of 17.4 minutes) to specifically activate the G-protein signaling cascade of APJ (92). MM07 showed beneficial cardiac effects in multiple rat studies, as well as increased vasodilation when administered into human forearms compared to pyr-AP-13 infusions (92,98). Additionally, Amgen developed a first-in-class novel APJ agonist, AMG 986, that improved cardiac contractility in animal models (99). AMG 986 was deemed tolerable in a phase 1b study but was ultimately suspended from future clinical trials due to a lack of efficacy and a need to "better define the clinical utility and optimal dosing for this molecule" (99). These examples of APJ agonists recapitulate the potential that targeting the AS has on developing a novel CVD drug and puts into perspective the importance of uncovering the mechanistic role the AS plays in CVD.

1.5 Chapter organization

The introduction chapter provides background information on the importance of the ceramides and apelins, the two inotropic agents investigated in this thesis project. It is important to note that in this dissertation, we chose to investigate cardiac hypertrophy as a surrogate for

heart failure. Cardiac hypertrophy is a disease caused by the thickening of the ventricular walls, and the enlargement of cardiomyocytes, a condition which can be replicated using cardiac cells in culture. Cardiac hypertrophy typically precedes the development of heart failure, due to the increased workload required to retain functionality of the hypertrophic heart (100). In Chapter 3, we will introduce our working hypertrophy model and describe in further detail why studying cardiac hypertrophy serves as a viable option for understanding the role that the ceramides and apelins play in the development of CVD.

In **Chapter 2** we examine the impact of silencing the *CERS* genes responsible for the production of LC (*CERS5/6*) and VLC (*CERS2*) ceramides on the cardiomyocytes' ability to maintain homeostasis. Here we explore the effects that knocking down these genes has on the levels of ceramides and their downstream, complex sphingolipid metabolites. We further dive into the effect these knockdowns have on the overall global cardiomyocyte transcriptome and the corresponding pathways affected. In **Chapter 3**, we use our optimized knockdown system, described in Chapter 2, to interrogate the cardiomyocyte's ability to handle the effects of hypertrophy when *CERS2* or *CERS5/6* are silenced. We begin this chapter by introducing the development of a reliable and robust cardiac hypertrophy model and present a thorough and complex transcriptomic analysis discussing the impact that knocking down either *CERS2* or *CERS5/6* have on the development of cardiac hypertrophy.

Chapter 4 tackles the importance of the apelinergic system. We expand on the role of the different components of the AS on the development of cardiac hypertrophy. We discuss the creation of a SNAP-APJ plasmid accompanied with the validation that this plasmid results in the overexpression of a stable and functional APJ in human embryonic kidney 293T (HEK293T) cells as well as adult ventricular cardiomyocytes. This is followed by viability and transcriptomic

analyses highlighting the importance of the different components of the AS in maintaining cardiomyocyte health before and after the induction of hypertrophy.

Chapter 5 has a slightly different focus where we present the development of a universal method by which high-throughput drug screening can be completed using GPCRs, while focusing on APJ to begin to tackle the identification of novel therapeutics that target this system. Previous methods for GPCR drug screening required labor intensive efforts to optimize conditions for each unique GPCR, significantly delaying or altogether halting progress on the development of drugs against tricky GPCR targets. We sought to develop a method that can be used universally to streamline the process of identifying binders to any GPCR. By utilizing virus-like particles expressing our GPCRs of interest, we were able to identify enriched binding to APJ with pyr-AP-13 in both simple and complex mixtures of thousands of peptides through affinity selection mass spectrometry (ASMS). The purification process and ASMS method development will be presented in this chapter.

In **Chapter 6**, we provide the final discussion and address next steps for future students, concluding this dissertation.

Figures

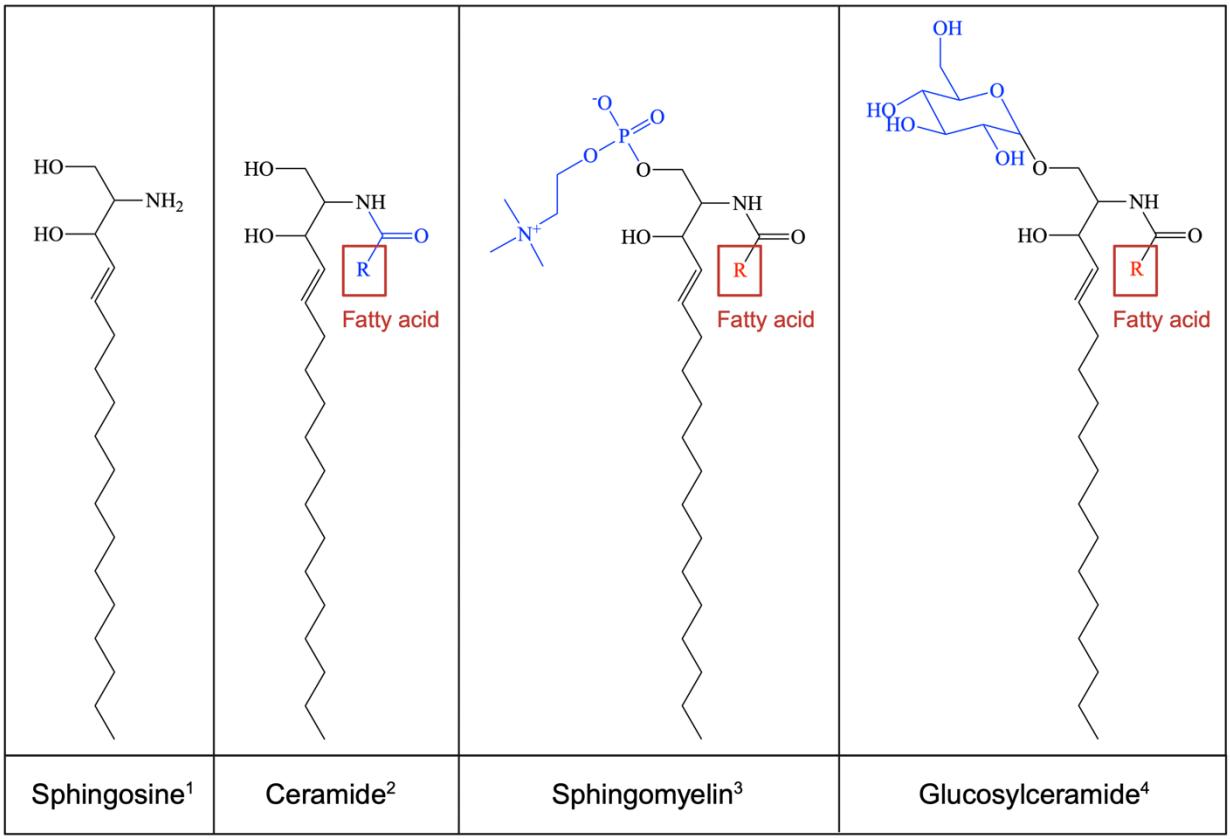

Figure 1.1. General sphingolipid structures.

Sphingolipid metabolites contain a fatty acid of varying chain length and level of saturation that is N-linked to the sphingosine backbone. Additionally, the identifiable factor of each sphingolipid depends on which head group is O-linked to this backbone. The number with the metabolite name correlates to the metabolic scheme found in **Figure 1.2**.

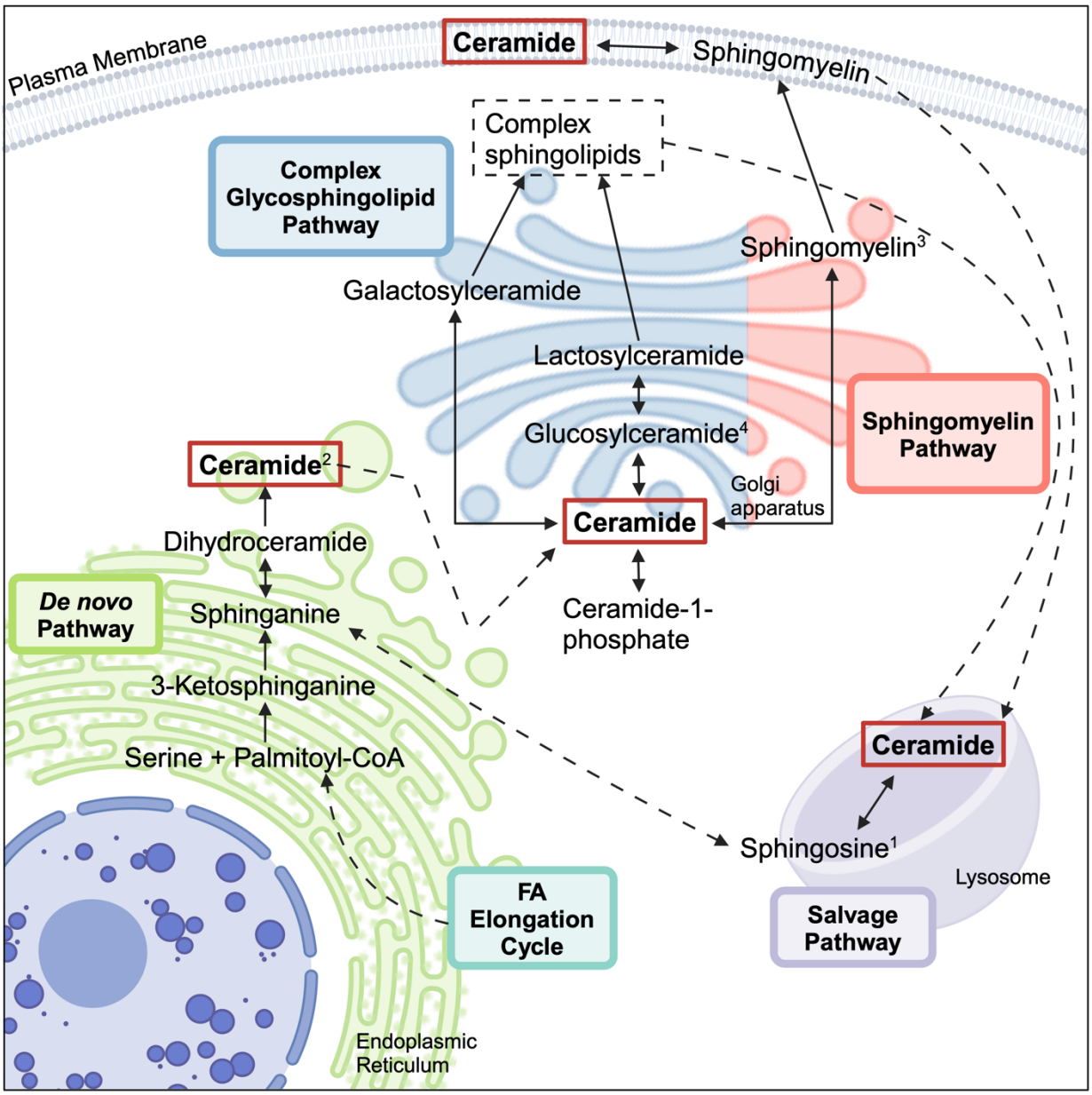

Figure 1.2. Simplified ceramide metabolic scheme.

There are four main pathways through which sphingolipid metabolites are catabolized or anabolized: the *de novo* pathway, salvage pathway, sphingomyelin pathway, and complex glycosphingolipid pathway. Ceramides created through these different pathways are generally thought to be spatially and functionally distinct. Structures of the metabolites with numbers can be found in **Figure 1.1**. FA – fatty acid. Created with BioRender.com

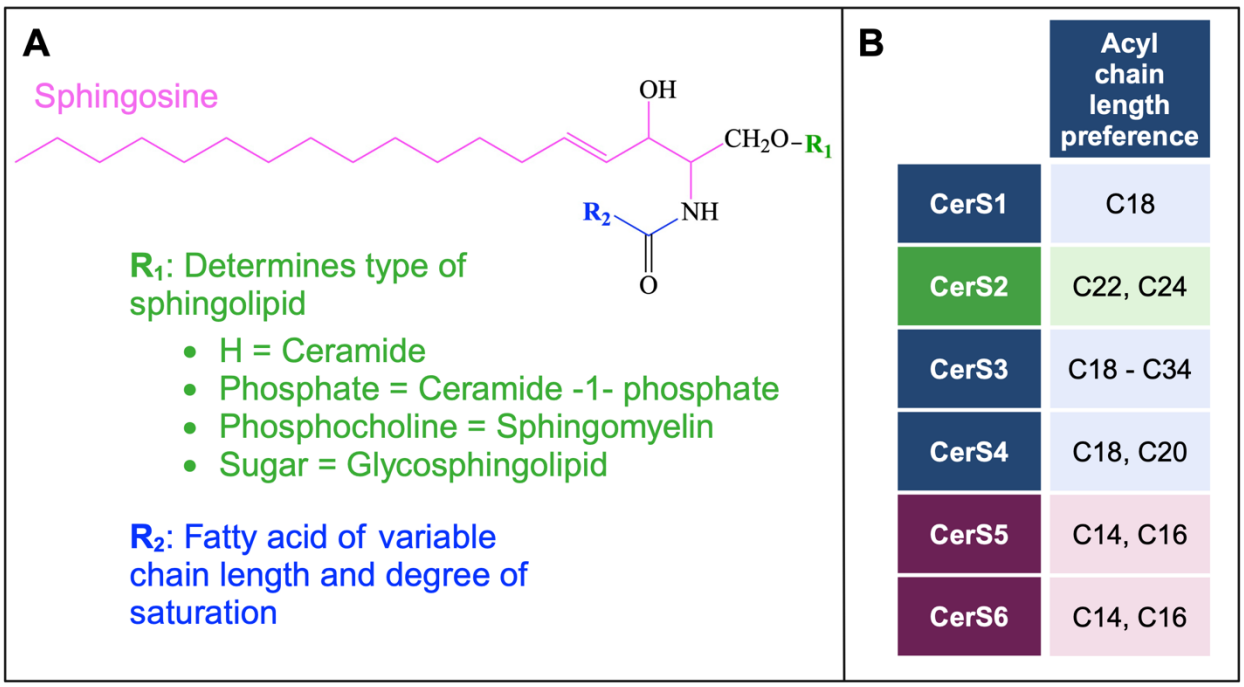

Figure 1.3. Acyl chain length preference of the mammalian CerS enzymes.

(**A**) The general components of a sphingolipid with a sphingosine backbone, varying fatty acid chain lengths and degrees of saturation acylated to this backbone (R_2), and a head group (R_1) determining the relevant sphingolipid class. (**B**) The different ceramide synthases (CerS) and their preferences in acyl chain length resulting in the generation of the corresponding ceramide. CerS2 is selective for the production of very long-chain ceramides (22:0 and 24:0) while CerS5 and CerS6 generate long chain ceramide (16:0). Created with BioRender.com

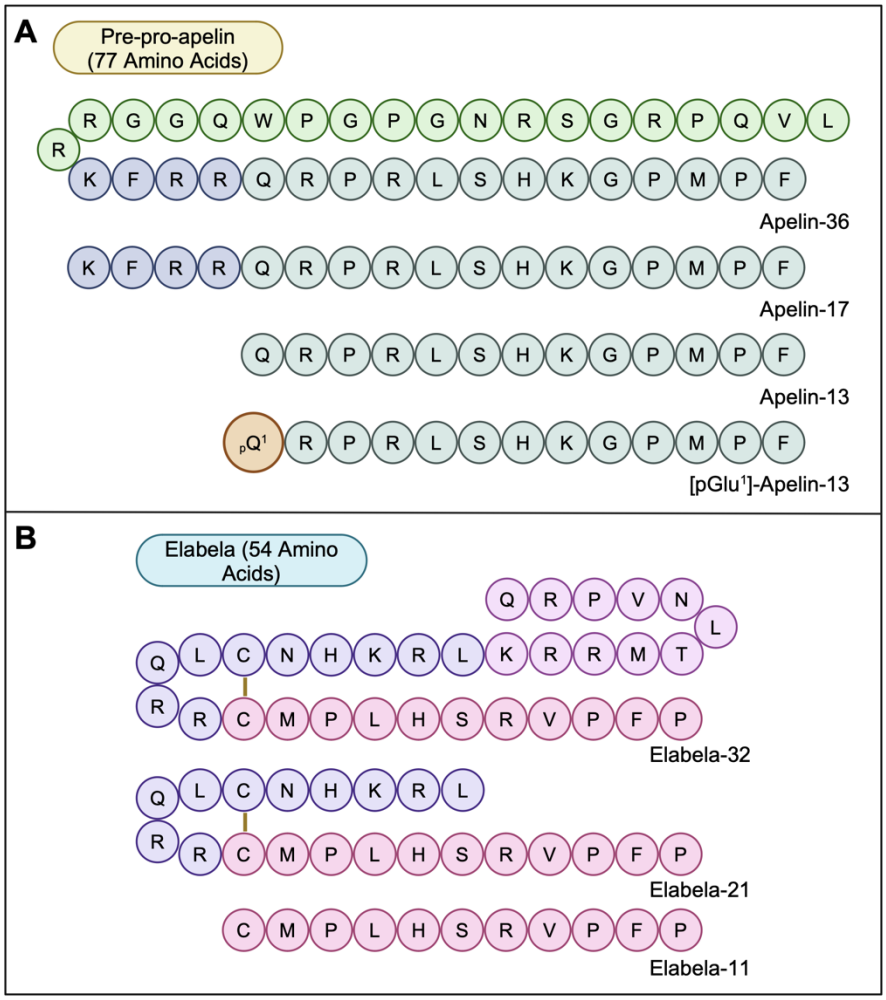

Figure 1.4. Amino acid sequence of the most studied AS peptide isoforms.

(**A**) apelin and (**B**) elabela. Created with BioRender.com

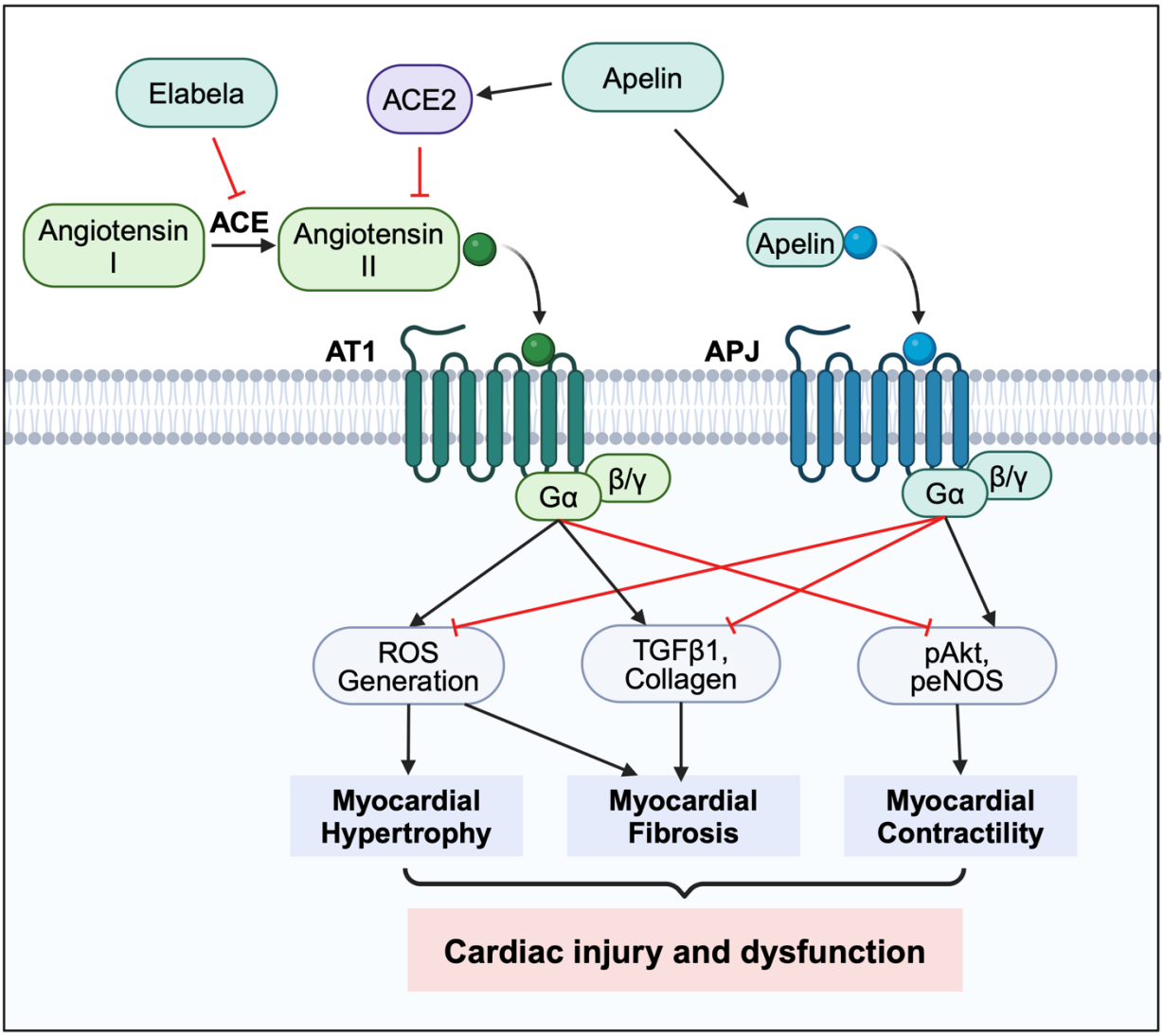

Figure 1.5. Scheme depicting AS antagonism of the renin-angiotensin-system (RAS).

ACE – angiotensin converting enzyme, ROS – reactive oxygen species. Created with BioRender.com

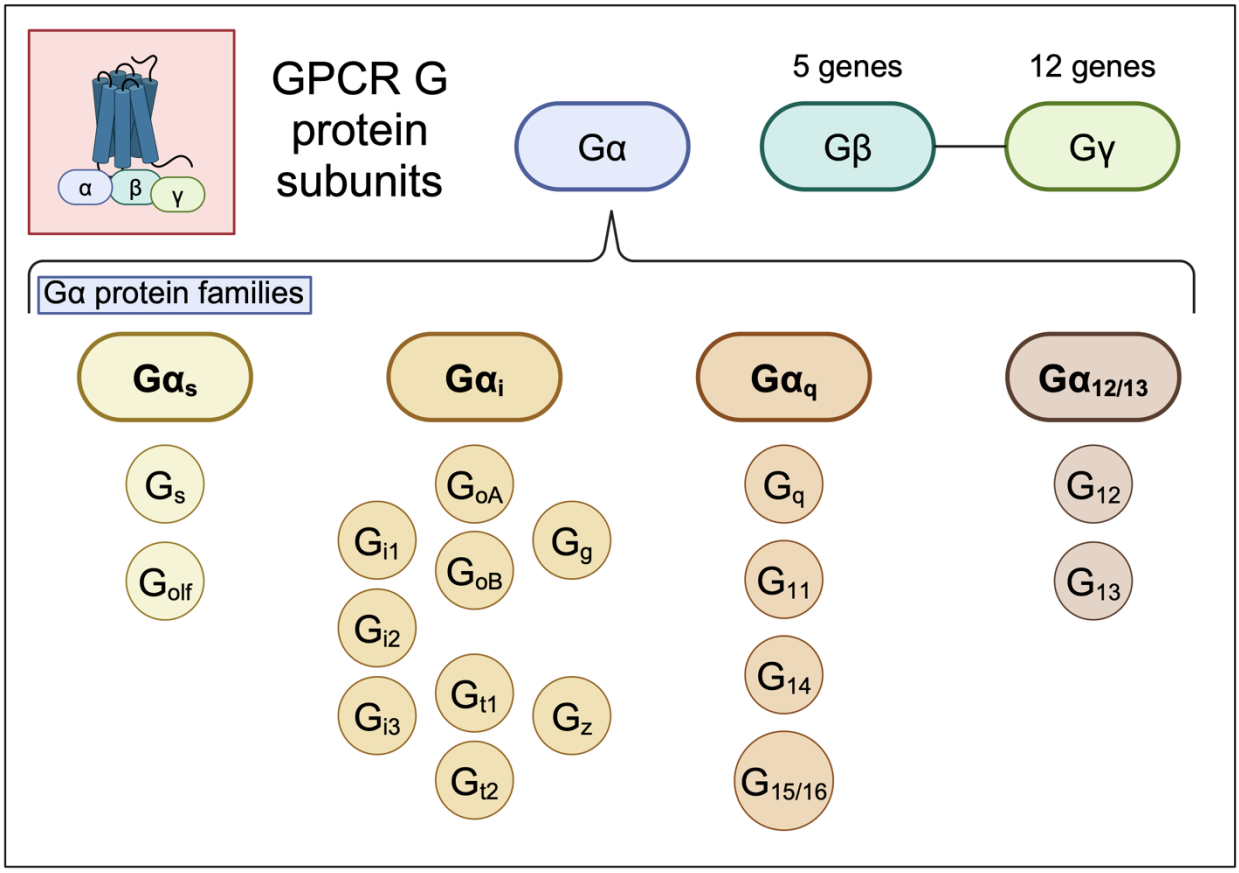

Figure 1.6. Summary of some of the different GPCR Gα subunits.

Created with BioRender.com

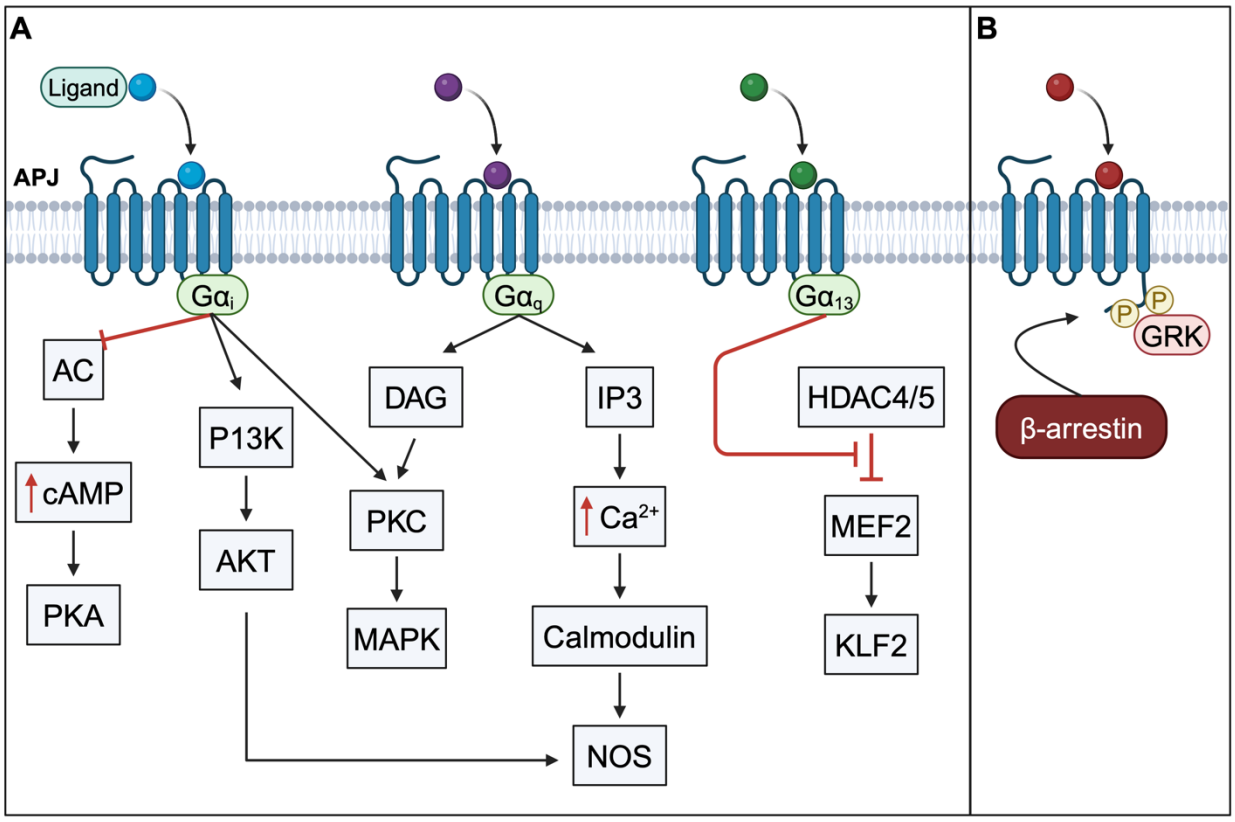

Figure 1.7. Overview of the APJ signaling cascades.

APJ signaling following activation of (**A**) G protein subunits and (**B**) β-arrestin activation. Created with BioRender.com

References

1. Institute for Health Metrics and Evaluations (IHME). GBD Results [Internet]. Seattle, WA: IHME, University of Washington 2024; [cited 2024 Apr 25]. Available from: https://vizhub.healthdata.org/gbd-results/

2. Roth GA, Mensah GA, Johnson CO, Addolorato G, Ammirati E, Baddour LM, et al. Global Burden of Cardiovascular Diseases and Risk Factors, 1990–2019. J Am Coll Cardiol. 2020 Dec;76(25):2982–3021.

3. Fihn SD, Gardin JM, Abrams J, Berra K, Blankenship JC, Dallas AP, et al. 2012 ACCF/AHA/ACP/AATS/PCNA/SCAI/STS Guideline for the Diagnosis and Management of Patients With Stable Ischemic Heart Disease: A Report of the American College of Cardiology Foundation/American Heart Association Task Force on Practice Guidelines, and the American College of Physicians, American Association for Thoracic Surgery, Preventive Cardiovascular Nurses Association, Society for Cardiovascular Angiography and Interventions, and Society of Thoracic Surgeons. Circulation [Internet]. 2012 Dec 18 [cited 2024 Jun 17];126(25). Available from: https://www.ahajournals.org/doi/10.1161/CIR.0b013e318277d6a0

4. McAlister FA, for the Renin Angiotension System Modulator Meta-Analysis Investigators. Angiotensin-converting enzyme inhibitors or angiotensin receptor blockers are beneficial in normotensive atherosclerotic patients: a collaborative meta-analysis of randomized trials. Eur Heart J. 2012 Feb 2;33(4):505–14.

5. DuBroff R. Cholesterol paradox: a correlate does not a surrogate make. Evid Based Med. 2017 Mar;22(1):15–9.

6. Albert MA. Biomarkers and Heart Disease. J Clin Sleep Med [Internet]. 2011 Oct 15 [cited 2024 Jun 17];7(5 Suppl). Available from: http://jcsm.aasm.org/doi/10.5664/JCSM.1342

7. Doust J, Lehman R, Glasziou P. The Role of BNP Testing in Heart Failure. 2006;74(11).

8. Chong KS, Gardner RS, Morton JJ, Ashley EA, McDonagh TA. Plasma concentrations of the novel peptide apelin are decreased in patients with chronic heart failure. Eur J Heart Fail. 2006;8(4):355–60.

9. El Amrousy D, El-Mahdy H. Prognostic Value of Serum Apelin Level in Children with Heart Failure Secondary to Congenital Heart Disease. Pediatr Cardiol. 2018 Aug;39(6):1188–93.

10. Lemaitre RN, Jensen PN, Hoofnagle A, McKnight B, Fretts AM, King IB, et al. Plasma Ceramides and Sphingomyelins in Relation to Heart Failure Risk: The Cardiovascular Health Study. Circ Heart Fail. 2019 Jul;12(7):e005708.

11. Pralhada Rao R, Vaidyanathan N, Rengasamy M, Mammen Oommen A, Somaiya N, Jagannath MR. Sphingolipid Metabolic Pathway: An Overview of Major Roles Played in Human Diseases. J Lipids. 2013;2013:1–12.

12. Kraft ML. Sphingolipid Organization in the Plasma Membrane and the Mechanisms That Influence It. Front Cell Dev Biol [Internet]. 2017 Jan 10 [cited 2024 Apr 15];4. Available from: http://journal.frontiersin.org/article/10.3389/fcell.2016.00154/full

13. Hannun YA, Obeid LM. Principles of bioactive lipid signalling: lessons from sphingolipids. Nat Rev Mol Cell Biol. 2008 Feb;9(2):139–50.

14. Kuo A, Hla T. Regulation of cellular and systemic sphingolipid homeostasis. Nat Rev Mol Cell Biol [Internet]. 2024 Jun 18 [cited 2024 Jul 13]; Available from: https://www.nature.com/articles/s41580-024-00742-y

15. Pettus BJ, Chalfant CE, Hannun YA. Ceramide in apoptosis: an overview and current perspectives. Biochim Biophys Acta BBA - Mol Cell Biol Lipids. 2002 Dec;1585(2–3):114–25.

16. Patwardhan GA, Beverly LJ, Siskind LJ. Sphingolipids and mitochondrial apoptosis. J Bioenerg Biomembr. 2016 Apr;48(2):153–68.

17. Zhu Q y, Wang Z, Ji C, Cheng L, Yang Y l, Ren J, et al. C6-ceramide synergistically potentiates the anti-tumor effects of histone deacetylase inhibitors via AKT dephosphorylation and α-tubulin hyperacetylation both in vitro and in vivo. Cell Death Dis. 2011 Jan 27;2(1):e117–e117.

18. Alonso A, Goñi FM. The Physical Properties of Ceramides in Membranes. Annu Rev Biophys. 2018 May 20;47(1):633–54.

19. Kitatani K, Idkowiak-Baldys J, Hannun YA. The sphingolipid salvage pathway in ceramide metabolism and signaling. Cell Signal. 2008 Jun;20(6):1010–8.

20. Hammerschmidt P, Brüning JC. Contribution of specific ceramides to obesity-associated metabolic diseases. Cell Mol Life Sci. 2022 Aug;79(8):395.

21. Milhas D, Clarke CJ, Hannun YA. Sphingomyelin metabolism at the plasma membrane: Implications for bioactive sphingolipids. FEBS Lett. 2010 May 3;584(9):1887–94.

22. Aureli M, Loberto N, Chigorno V, Prinetti A, Sonnino S. Remodeling of Sphingolipids by Plasma Membrane Associated Enzymes. Neurochem Res. 2011 Sep;36(9):1636–44.

23. Hammad SM. Blood Sphingolipids in Homeostasis and Pathobiology. In: Cowart LA, editor. Sphingolipids and Metabolic Disease [Internet]. New York, NY: Springer New York; 2011 [cited 2024 Apr 16]. p. 57–66. (Advances in Experimental Medicine and Biology; vol. 721). Available from: http://link.springer.com/10.1007/978-1-4614-0650-1_4

24. Calzada C, Vors C, Penhoat A, Cheillan D, Michalski MC. Role of circulating sphingolipids in lipid metabolism: Why dietary lipids matter. Front Nutr. 2023 Jan 11;9:1108098.

25. Summers SA. Could Ceramides Become the New Cholesterol? Cell Metab. 2018 Feb;27(2):276–80.

26. Laaksonen R, Ekroos K, Sysi-Aho M, Hilvo M, Vihervaara T, Kauhanen D, et al. Plasma ceramides predict cardiovascular death in patients with stable coronary artery disease and acute coronary syndromes beyond LDL-cholesterol. Eur Heart J. 2016 Jul 1;37(25):1967–76.

27. CERAM - Overview MI-Heart Ceramides, Plasma [Internet]. Mayo Clinic Laboratories; 2024. Available from: https://www.mayocliniclabs.com/test-catalog/overview/606777#Clinical-and-Interpretive

28. Grösch S, Schiffmann S, Geisslinger G. Chain length-specific properties of ceramides. Prog Lipid Res. 2012 Jan;51(1):50–62.

29. Venkataraman K, Riebeling C, Bodennec J, Riezman H, Allegood JC, Sullards MC, et al. Upstream of Growth and Differentiation Factor 1 (uog1), a Mammalian Homolog of the Yeast Longevity Assurance Gene 1 (LAG1), RegulatesN-Stearoyl-sphinganine (C18-(Dihydro)ceramide) Synthesis in a Fumonisin B1-independent Manner in Mammalian Cells. J Biol Chem. 2002 Sep;277(38):35642–9.

30. Laviad EL, Albee L, Pankova-Kholmyansky I, Epstein S, Park H, Merrill AH, et al. Characterization of Ceramide Synthase 2. J Biol Chem. 2008 Feb;283(9):5677–84.

31. Mizutani Y, Kihara A, Igarashi Y. LASS3 (longevity assurance homologue 3) is a mainly testis-specific (dihydro)ceramide synthase with relatively broad substrate specificity. Biochem J. 2006 Sep 15;398(3):531–8.

32. Lahiri S, Futerman AH. LASS5 Is a Bona Fide Dihydroceramide Synthase That Selectively Utilizes Palmitoyl-CoA as Acyl Donor. J Biol Chem. 2005 Oct;280(40):33735–8.

33. Mizutani Y, Kihara A, Igarashi Y. Mammalian Lass6 and its related family members regulate synthesis of specific ceramides. Biochem J. 2005 Aug 15;390(1):263–71.

34. Ho QWC, Zheng X, Ali Y. Ceramide Acyl Chain Length and Its Relevance to Intracellular Lipid Regulation. Int J Mol Sci. 2022 Aug 26;23(17):9697.

35. The UniProt Consortium, Bateman A, Martin MJ, Orchard S, Magrane M, Ahmad S, et al. UniProt: the Universal Protein Knowledgebase in 2023. Nucleic Acids Res. 2023 Jan 6;51(D1):D523–31.

36. Lee S, Kim SA, Kim Y, Kim J, Hong G, Hong J, et al. Genetic Variants Associated with Elevated Plasma Ceramides in Individuals with Metabolic Syndrome. Genes. 2022 Aug 22;13(8):1497.

37. Zietzer A, Düsing P, Reese L, Nickenig G, Jansen F. Ceramide Metabolism in Cardiovascular Disease: A Network With High Therapeutic Potential. Arterioscler Thromb Vasc Biol. 2022 Oct;42(10):1220–8.

38. Nicholson RJ, Poss AM, Maschek JA, Cox JE, Hopkins PN, Hunt SC, et al. Characterizing a Common CERS2 Polymorphism in a Mouse Model of Metabolic Disease and in Subjects from the Utah CAD Study. J Clin Endocrinol Metab. 2021 Jul 13;106(8):e3098–109.

39. De La Monte SM. Triangulated Mal-Signaling in Alzheimer's Disease: Roles of Neurotoxic Ceramides, ER Stress, and Insulin Resistance Reviewed. Frisardi V, Imbimbo B, editors. J Alzheimers Dis. 2012 Jun 8;30(s2):S231–49.

40. Gosejacob D, Jäger PS, Vom Dorp K, Frejno M, Carstensen AC, Köhnke M, et al. Ceramide Synthase 5 Is Essential to Maintain C16:0-Ceramide Pools and Contributes to the Development of Diet-induced Obesity. J Biol Chem. 2016 Mar;291(13):6989–7003.

41. Turpin SM, Nicholls HT, Willmes DM, Mourier A, Brodesser S, Wunderlich CM, et al. Obesity-Induced CerS6-Dependent C16:0 Ceramide Production Promotes Weight Gain and Glucose Intolerance. Cell Metab. 2014 Oct;20(4):678–86.

42. Lee SY, Kim JR, Hu Y, Khan R, Kim SJ, Bharadwaj KG, et al. Cardiomyocyte Specific Deficiency of Serine Palmitoyltransferase Subunit 2 Reduces Ceramide but Leads to Cardiac Dysfunction. J Biol Chem. 2012 May;287(22):18429–39.

43. Canals D, Perry DM, Jenkins RW, Hannun YA. Drug targeting of sphingolipid metabolism: sphingomyelinases and ceramidases. Br J Pharmacol. 2011 Jun;163(4):694–712.

44. Hannun YA, Loomis CR, Merrill AH, Bell RM. Sphingosine inhibition of protein kinase C activity and of phorbol dibutyrate binding in vitro and in human platelets. J Biol Chem. 1986 Sep;261(27):12604–9.

45. Kleuser B. The Enigma of Sphingolipids in Health and Disease. Int J Mol Sci. 2018 Oct 12;19(10):3126.

46. Janneh AH, Ogretmen B. Targeting Sphingolipid Metabolism as a Therapeutic Strategy in Cancer Treatment. Cancers. 2022 Apr 27;14(9):2183.

47. Riley RT, Merrill AH. Ceramide synthase inhibition by fumonisins: a perfect storm of perturbed sphingolipid metabolism, signaling, and disease. J Lipid Res. 2019 Jul;60(7):1183–9.

48. Turner N, Lim XY, Toop HD, Osborne B, Brandon AE, Taylor EN, et al. A selective inhibitor of ceramide synthase 1 reveals a novel role in fat metabolism. Nat Commun. 2018 Aug 21;9(1):3165.

49. Zhang X, Kitatani K, Toyoshima M, Ishibashi M, Usui T, Minato J, et al. Ceramide Nanoliposomes as a MLKL-Dependent, Necroptosis-Inducing, Chemotherapeutic Reagent in Ovarian Cancer. Mol Cancer Ther. 2018 Jan 1;17(1):50–9.

50. Bockus LB, Jensen PN, Fretts AM, Hoofnagle AN, McKnight B, Sitlani CM, et al. Plasma Ceramides and Sphingomyelins and Sudden Cardiac Death in the Cardiovascular Health Study. JAMA Netw Open. 2023 Nov 17;6(11):e2343854.

51. Bosak K, Sauer A, Meeusen J. Clinical Update: Ceramides As Novel Biomarkers of Cardiovascular Disease Risk. J Nurse Pract. 2024 Jan;20(1):104838.

52. Nwabuo CC, Duncan M, Xanthakis V, Peterson LR, Mitchell GF, McManus D, et al. Association of Circulating Ceramides With Cardiac Structure and Function in the Community: The Framingham Heart Study. J Am Heart Assoc. 2019 Oct;8(19):e013050.

53. Yu J, Pan W, Shi R, Yang T, Li Y, Yu G, et al. Ceramide Is Upregulated and Associated With Mortality in Patients With Chronic Heart Failure. Can J Cardiol. 2015 Mar;31(3):357–63.

54. Castan-Laurell I, Masri B, Valet P. The apelin/APJ system as a therapeutic target in metabolic diseases. Expert Opin Ther Targets. 2019 Mar 4;23(3):215–25.

55. Huang Z, He L, Chen Z, Chen L. Targeting drugs to APJ receptor: From signaling to pathophysiological effects. J Cell Physiol. 2018 Jan 1;234(1):61–74.

56. Shin K, Kenward C, Rainey JK. Apelinergic system structure and function. Compr Physiol. 2018 Jan 1;8(1):407–50.

57. Hu H, He L, Li L, Chen L. Apelin/APJ system as a therapeutic target in diabetes and its complications. Mol Genet Metab. 2016 Sep 1;119(1–2):20–7.

58. Ma Z, Song JJ, Martin S, Yang XC, Zhong JC. The Elabela-APJ axis: a promising therapeutic target for heart failure. Heart Fail Rev. 2020;

59. Iwanaga Y, Kihara Y, Takenaka H, Kita T. Down-regulation of cardiac apelin system in hypertrophied and failing hearts: Possible role of angiotensin II–angiotensin type 1 receptor system. J Mol Cell Cardiol. 2006 Nov;41(5):798–806.

60. Wang M, Gupta RC, Rastogi S, Kohli S, Sabbah MS, Zhang K, et al. Effects of Acute Intravenous Infusion of Apelin on Left Ventricular Function in Dogs With Advanced Heart Failure. J Card Fail. 2013 Jul;19(7):509–16.

61. Yang P, Maguire JJ, Davenport AP. Apelin, Elabela/Toddler, and biased agonists as novel therapeutic agents in the cardiovascular system. Trends Pharmacol Sci. 2015 Sep 12;36(9):560–7.

62. Tatemoto K, Hosoya M, Habata Y, Fujii R, Kakegawa T, Zou MX, et al. Isolation and Characterization of a Novel Endogenous Peptide Ligand for the Human APJ Receptor. Biochem Biophys Res Commun. 1998 Oct;251(2):471–6.

63. Szokodi I, Tavi P, Földes G, Voutilainen-Myllylä S, Ilves M, Tokola H, et al. Apelin, the Novel Endogenous Ligand of the Orphan Receptor APJ, Regulates Cardiac Contractility. Circ Res. 2002 Sep 6;91(5):434–40.

64. Tatemoto K, Takayama K, Zou MX, Kumaki I, Zhang W, Kumano K, et al. The novel peptide apelin lowers blood pressure via a nitric oxide-dependent mechanism. Regul Pept. 2001 Jun;99(2–3):87–92.

65. Japp AG, Cruden NL, Barnes G, Van Gemeren N, Mathews J, Adamson J, et al. Acute Cardiovascular Effects of Apelin in Humans: Potential Role in Patients With Chronic Heart Failure. Circulation. 2010 Apr 27;121(16):1818–27.

66. Chng SC, Ho L, Tian J, Reversade B. ELABELA: A Hormone Essential for Heart Development Signals via the Apelin Receptor. Dev Cell. 2013 Dec;27(6):672–80.

67. Perjés Á, Kilpiö T, Ulvila J, Magga J, Alakoski T, Szabó Z, et al. Characterization of apela, a novel endogenous ligand of apelin receptor, in the adult heart. Basic Res Cardiol. 2016 Jan;111(1):2.

68. Pauli A, Norris ML, Valen E, Chew GL, Gagnon JA, Zimmerman S, et al. Toddler: An Embryonic Signal That Promotes Cell Movement via Apelin Receptors. Science. 2014 Feb 14;343(6172):1248636.

69. Wang Z, Yu D, Wang M, Wang Q, Kouznetsova J, Yang R, et al. Elabela-Apelin Receptor Signaling Pathway is Functional in Mammalian Systems. Sci Rep. 2015 Feb 2;5(1):8170.

70. Wysocka MB, Pietraszek-Gremplewicz K, Nowak D. The Role of Apelin in Cardiovascular Diseases, Obesity and Cancer. Front Physiol. 2018;9.

71. Mitra J, Tang X jun, Almo SC, Shields D. Temperature-induced conformational changes in prosomatostatin-II: implications for processing. Biochem J. 1998 Aug 15;334(1):275–82.

72. Lee DK, Saldivia VR, Nguyen T, Cheng R, George SR, O'Dowd BF. Modification of the Terminal Residue of Apelin-13 Antagonizes Its Hypotensive Action. Endocrinology. 2005 Jan 1;146(1):231–6.

73. Habata Y, Fujii R, Hosoya M, Fukusumi S, Kawamata Y, Hinuma S, et al. Apelin, the natural ligand of the orphan receptor APJ, is abundantly secreted in the colostrum. Biochim Biophys Acta BBA - Mol Cell Res. 1999 Oct;1452(1):25–35.

74. Shin K, Landsman M, Pelletier S, Alamri BN, Anini Y, Rainey JK. Proapelin is processed extracellularly in a cell line-dependent manner with clear modulation by proprotein convertases. Amino Acids. 2019;51(3):395–405.

75. Zhen EY, Higgs RE, Gutierrez JA. Pyroglutamyl apelin-13 identified as the major apelin isoform in human plasma. Anal Biochem. 2013 Nov;442(1):1–9.

76. Zhong JC, Zhang ZZ, Wang W, McKinnie SMK, Vederas JC, Oudit GY. Targeting the apelin pathway as a novel therapeutic approach for cardiovascular diseases. Biochim Biophys Acta BBA - Mol Basis Dis. 2017 Aug;1863(8):1942–50.

77. Wang W, McKinnie SMK, Farhan M, Paul M, McDonald T, McLean B, et al. Angiotensin-Converting Enzyme 2 Metabolizes and Partially Inactivates Pyr-Apelin-13 and Apelin-17: Physiological Effects in the Cardiovascular System. Hypertension. 2016 Aug;68(2):365–77.

78. Mehta JK, Kaur G, Buttar HS, Bagabir HA, Bagabir RA, Bagabir SA, et al. Role of the renin–angiotensin system in the pathophysiology of coronary heart disease and heart failure: Diagnostic biomarkers and therapy with drugs and natural products. Front Physiol. 2023 Feb 23;14:1034170.

79. Zhang ZZ, Wang W, Jin HY, Chen X, Cheng YW, Xu YL, et al. Apelin is a negative regulator of angiotensin II-mediated adverse myocardial remodeling and dysfunction. Hypertension. 2017;70(6):1165–75.

80. Sato T, Sato C, Kadowaki A, Watanabe H, Ho L, Ishida J, et al. ELABELA-APJ axis protects from pressure overload heart failure and angiotensin II-induced cardiac damage. Cardiovasc Res. 2017 Jun 1;113(7):760–9.

81. Siddiquee K, Hampton J, McAnally D, May L, Smith L. The apelin receptor inhibits the angiotensin II type 1 receptor via allosteric trans-inhibition. Br J Pharmacol. 2013 Mar;168(5):1104–17.

82. Koguchi W, Kobayashi N, Takeshima H, Ishikawa M, Sugiyama F, Ishimitsu T. Cardioprotective Effect of Apelin-13 on Cardiac Performance and Remodeling in End-Stage Heart Failure. Circ J. 2012;76(1):137–44.

83. Chen MM, Ashley EA, Deng DXF, Tsalenko A, Deng A, Tabibiazar R, et al. Novel Role for the Potent Endogenous Inotrope Apelin in Human Cardiac Dysfunction. Circulation. 2003;108(12):1432–9.

84. Yang D, Zhou Q, Labroska V, Qin S, Darbalaei S, Wu Y, et al. G protein-coupled receptors: structure- and function-based drug discovery. Signal Transduct Target Ther. 2021 Jan 8;6(1):7.

85. Syrovatkina V, Alegre KO, Dey R, Huang XY. Regulation, Signaling, and Physiological Functions of G-Proteins. J Mol Biol. 2016 Sep;428(19):3850–68.

86. Baltoumas FA, Theodoropoulou MC, Hamodrakas SJ. Interactions of the α-subunits of heterotrimeric G-proteins with GPCRs, effectors and RGS proteins: A critical review and analysis of interacting surfaces, conformational shifts, structural diversity and electrostatic potentials. J Struct Biol. 2013 Jun;182(3):209–18.

87. Okashah N, Wan Q, Ghosh S, Sandhu M, Inoue A, Vaidehi N, et al. Variable G protein determinants of GPCR coupling selectivity. Proc Natl Acad Sci. 2019 Jun 11;116(24):12054–9.

88. Bourne HR, Sanders DA, McCormick F. The GTPase superfamily: conserved structure and molecular mechanism. Nature. 1991 Jan 10;349(6305):117–27.

89. Kee TR, Khan SA, Neidhart MB, Masters BM, Zhao VK, Kim YK, et al. The multifaceted functions of β-arrestins and their therapeutic potential in neurodegenerative diseases. Exp Mol Med. 2024 Jan 11;56(1):129–41.

90. Calebiro D, Godbole A. Internalization of G-protein-coupled receptors: Implication in receptor function, physiology and diseases. Best Pract Res Clin Endocrinol Metab. 2018;32(2):83–91.

91. Whalen EJ, Rajagopal S, Lefkowitz RJ. Therapeutic potential of β-arrestin- and G protein-biased agonists. Trends Mol Med. 2011 Mar;17(3):126–39.

92. Brame AL, Maguire JJ, Yang P, Dyson A, Torella R, Cheriyan J, et al. Design, characterization, and first-in-human study of the vascular actions of a novel biased apelin receptor agonist. Hypertension. 2015 Apr 20;65(4):834–40.

93. Tian Y, Chen R, Jiang Y, Bai B, Yang T, Liu H. The Protective Effects and Mechanisms of Apelin/APJ System on Ischemic Stroke: A Promising Therapeutic Target. Front Neurol. 2020 Mar 3;11:75.

94. Wang T, Li Z, Cvijic ME, Zhang L, Sum CS. Measurement of cAMP for Gαs- and Gαi Protein-Coupled Receptors (GPCRs).

95. Desjardins C, Naya F. The Function of the MEF2 Family of Transcription Factors in Cardiac Development, Cardiogenomics, and Direct Reprogramming. J Cardiovasc Dev Dis. 2016 Aug 11;3(3):26.

96. Kang Y, Kim J, Anderson JP, Wu J, Gleim SR, Kundu RK, et al. Apelin-APJ Signaling Is a Critical Regulator of Endothelial MEF2 Activation in Cardiovascular Development. Circ Res. 2013 Jun 21;113(1):22–31.

97. Pope GR, Tilve S, McArdle CA, Lolait SJ, O'Carroll AM. Agonist-induced internalization and desensitization of the apelin receptor. Mol Cell Endocrinol. 2016;437:108–19.

98. Yang P, Read C, Kuc RE, Nyimanu D, Williams TL, Crosby A, et al. A novel cyclic biased agonist of the apelin receptor, MM07, is disease modifying in the rat monocrotaline model of pulmonary arterial hypertension. Br J Pharmacol. 2019 May;176(9):1206–21.

99. Winkle P, Goldsmith S, Koren MJ, Lepage S, Hellawell J, Trivedi A, et al. A First-in-Human Study of AMG 986, a Novel Apelin Receptor Agonist, in Healthy Subjects and Heart Failure Patients. Cardiovasc Drugs Ther. 2023 Aug;37(4):743–55.

100. Tham YK, Bernardo BC, Ooi JYY, Weeks KL, McMullen JR. Pathophysiology of cardiac hypertrophy and heart failure: signaling pathways and novel therapeutic targets. Arch Toxicol. 2015 Sep;89(9):1401–38.

Chapter 2: The Inverse Role of Cellular Long-Chain and Very Long-Chain Ceramides on Cardiomyocyte Health

2.1 Introduction

Sphingolipids are an important class of signaling lipids that play many significant roles in the body, both structurally and functionally. Within the sphingolipid class, ceramides form the essential structural backbone of the more complex sphingolipids, thus alterations in ceramide levels could dysregulate the entire cellular sphingolipid metabolic pathway (1,2). Specific ceramide species are distinguishable by the fatty acid that is acylated to the sphingosine backbone, leading to distinct biological activities. Generally, it is thought that LC ceramides (16:0 and 18:0) drive metabolic dysfunction resulting in the progression of different disease states, while VLC ceramides (22:0 and 24:0) are thought to be either beneficial against disease progression or benign (3–7). The importance of ceramides is discussed in detail in **Section 1.3**.

In 2019, our collaborators reported that plasma ceramide and SM species with different saturated fatty acids differentially associated with risk of incident heart failure in the Cardiovascular Health Study, that contained a large cohort of older adults with cardiovascular disease (8). They discovered that 16:0 ceramide and SM were associated with an increased risk of incident heart failure, while 22:0 ceramide, and 20:0, 22:0, and 24:0 SM were associated with a decreased risk of heart failure, independent of other risk factors (8). To determine possible mechanisms underlying the associations between ceramide and SM species with incident heart failure, we hypothesized that modulating levels of 16:0, 22:0, and 24:0 ceramide in human adult cardiomyocytes would modify biological processes related to heart failure.

In this chapter, we present reproducible and reliable conditions for the targeted silencing of the ceramide synthases (*CERS2* and *CERS5/6*) responsible for the production of 16:0, 22:0,

and 24:0 ceramide. Since there is overlap in CerS5/6 activity to produce 16:0 ceramide, we decided to knockdown both genes simultaneously to achieve the maximal effect on reducing 16:0 levels. Here, we confirm that knockdown results in LC and VLC cellular ceramide reductions and explore how reducing these ceramide species alters overall cardiomyocyte survival. We conclude this chapter by analyzing the whole genome transcriptional response to identify specific perturbed pathways in adult ventricular cardiomyocytes that could contribute to changes in cardiac homeostasis.

2.1.1 Research Strategy

The data in this chapter is presented following the logical progression of experiments required to validate our *CERS* knockdown (KD) models before evaluating how these model systems alter the cardiomyocyte's ability to maintain homeostasis. Initially we discuss the validation of our selected cell line and findings that led us to adopt this specific experimental approach. We then present on the optimization process for knocking down *CERS2* and *CERS5/6* as well as the verification that these KDs result in reductions of the expected ceramide species. Preceding these sections, we address our transcriptomic analyses and describe our findings on how silencing either *CERS2* or *CERS5/6* affects crucial cardiomyocyte functions. We conclude this chapter by comparing the observed responses following *CERS2* and *CERS5/6* KD. The completion of this work provides a more extensive mechanistic understanding of the role that LC and VLC ceramides play in maintaining cardiomyocyte homeostasis.

2.2 Materials and Methods

2.2.1 Materials

Immortalized human ventricular cardiomyocytes and all their applicable materials including PriGrow I media, penicillin/strep, and extracellular matrix were purchased through Applied Biological Materials (Bellingham, WA). *CERS2* siRNA duplex (#SR323951) was purchased from Origene (Rockville, MD) and the universal scrambled negative control siRNA duplex that came with this product was used as the control. Silencer siRNA for *CERS5* (#AM16708, siRNA ID #131807), *CERS6* (#AM16708, siRNA ID #149485), and the control used for this experimental group, Silencer Negative Control #5 siRNA (#AM4642) were purchased from Invitrogen (Waltham, MA). A small volume protein assay was obtained from Bio-Rad Laboratories (Hercules, CA). Tissue culture treated plates, Lipofectamine 3000 Reagent, dimethyl sulfoxide (DMSO), Opti-MEM media, phosphate buffered saline (PBS), cell scrapers, PrestoBlue Viability Reagent, RNA isolation kits, and High-Capacity RNA-to-cDNA kits were all obtained from Thermo Fisher Scientific (Waltham, MA). Additionally, all RT-qPCR materials were purchased from Thermo Fisher Scientific's TaqMan Line: TaqMan Fast Advanced Master Mix for qPCR and TaqMan human primers: GUSB (Assay ID: Hs00939627_m1), CERS2 (Assay ID: Hs00371958_g1), CERS5 (Assay ID: Hs00908759_m1), and CERS6 (Assay ID: Hs00826756_m1). Methyl tert-butyl ether, methanol, isopropanol, and LC-MS/MS grade water were from Fisher Scientific. A stable isotope-labeled internal standard mixture containing 10 sphingolipids (#LM6002) was purchased from Avanti Polar Lipids (Alabaster, AL).

2.2.2 Cell culture

Immortalized human ventricular cardiomyocytes (HCMs) (#T0519) were maintained with PriGrow I medium (#TM001) supplemented with 10% fetal bovine serum (FBS) and 0.1%

Penicillin/Streptomycin Solution (#G255). Cells were cultured in a humidified incubator at 37ºC with 5% CO_2. All plates were coated with Extracellular Matrix (#G422) according to the manufacturer's protocol.

2.2.3 Silencing *CERS2* and *CERS5/6*

Gene silencing was achieved using a reverse transfection protocol in 6-well plate. Cells (3.5×10^5) were plated with 10 nM of each respective siRNA and 5.9 µL Lipofectamine 3000 (#L3000001) per well. The lipofectamine and siRNA were mixed with Opti-MEM media (#31985070) and allowed to sit at room temperature for 20 min before addition to the cells. The transfection mixture was combined with cells suspended in complete media and a total volume of 2.5 mL was added to each well, with the transfection mixture accounting for 10% of the total volume. After 24h cells either underwent a media change (for mass spectrometry analysis) or a 48h vehicle treatment was initiated in serum-free media (maximum 0.025% DMSO).

2.2.4 Sphingolipid quantification by high-performance liquid chromatography - tandem mass spectrometry (HPLC-MS/MS)

Following transfection for 48h, cells were washed twice with 600 µL ice cold PBS (#10010031), harvested by scraping in ice cold PBS, and pelleted by centrifugation at 300 x *g* for 5 min. The supernatant was then aspirated and the cell pellets were stored at -80ºC until further analysis. Each experiment was performed in triplicate (n=3).

To increase rigor, experiments were repeated three months later (n=6 for each experimental condition). Once cell pellet collection was complete, the samples were thawed on ice and resuspended in PBS. The cells were then lysed by placing them in an iced sonication bath for 30 min. Protein concentration was measured by small volume protein assay (Bio-Rad

Laboratories, #500012; Hercules, CA) and each sample was normalized to 1 mg/mL. Sphingolipids in each cell lysate were quantified using solvent extraction with a methyl tert-butyl ether (MTBE), methanol, isopropanol mixture and liquid chromatography-tandem mass spectrometry, as previously described in detail (9). Statistical significance was determined through multiple unpaired t-tests.

2.2.5 Total RNA isolation and RT-qPCR

Following the 24h siRNA incubation and the completion of the 48h vehicle treatment, cells were rinsed once with ice cold PBS and lysed with TRI Reagent. The cells then underwent total RNA isolation utilizing the MagMax-96 for Microarrays Total RNA Isolation Kit (#AM1839) following the spin procedure. After RNA isolation, RNA was converted to cDNA by reverse transcriptase using the High-Capacity RNA-to-cDNA kit (#4387406). RT-qPCR was then conducted utilizing the Taqman Gene Expression Assay reagents (Thermo Fisher Scientific, FAM dye). Gene expression was normalized to the housekeeping gene, GUSB, and data was analyzed following the comparative delta-Ct method. Unpaired two-tailed t-tests were used to determine statistical significance between samples.

2.2.6 Cell viability

Cell viability was tested in HCMs that underwent a scaled-down transfection with respect to surface area, in a 24-well plate. Every 24h, for a total of 72h post transfection, wells underwent a fresh serum-free media exchange with the vehicle control (maximum 0.025% DMSO). At the 72h mark, HCM viability was measure utilizing the PrestoBlue HS Cell Viability Reagent (#P50201) according to the manufacturer's protocol. HCMs were incubated in the presence of the resazurin-based presto blue reagent for 2h prior to reading the absorbance using the Tecan Spark V3.0. Statistical significance was determined using unpaired two-tailed t-tests.

2.2.7 Library preparation and mRNA-sequencing

After total RNA isolation, samples were sent to Novogene Corporation Inc. (Sacramento, CA) for mRNA-sequencing. Samples were first subjected to a quality control check and library preparation, where samples underwent a polyA capture to enrich mRNA and remove rRNA, then the mRNA was converted into cDNA. The libraries then underwent a second quality control before sequencing with Illumina PE150 technology. Sequencing data was checked for quality a final time before undergoing bioinformatic analysis. The sequence of each sample was aligned to the human reference genome GRCh38 and all samples were confirmed to map to over 90% of the reference genome. One of the scramble controls for the *CERS2* KD did not meet this criterion, hence was excluded from further analysis.

2.2.8 Bioinformatics and pathway analysis

2.2.8.A Gene expression analysis

Once the sequence was mapped to the reference genome, the raw counts were refined by removing any genes that did not have a maximum value of at least 10 between samples. The differentially expressed genes were then identified between the various treatment groups and controls using DESeq2 analysis in R and given a rank order based on DESeq2's test statistic (10).

2.2.8.B Gene set enrichment analysis (GSEA)

To identify biological pathways altered by each *CERS* KD condition, we applied a GSEA (11,12) using two Molecular Signature Database categories: hallmark and canonical pathways (13,14). The preranked DESeq2 files were uploaded and a false discovery rate (FDR) < 0.05 threshold was implemented to analyze significant gene set enrichment following *CERS* KD.

Additionally, the list of genes compiled within the gene set entitled ‘GOBP sphingolipid metabolic process’ was utilized for sphingolipid differentially expressed gene (DEG) investigation. These genes were separated into 6 different groups based on their role within sphingolipid metabolism: fatty acid (FA) elongation cycle, *de novo* pathway, salvage pathway, sphingomyelin pathway, complex sphingolipid pathway, or if the gene did not fit into any of these sectors of the metabolic scheme, it was placed into an “other” sphingolipid pathway group. Following the completion of the GSEA pathway analyses, enrichment maps were created utilizing Cytoscape 3.10.2 with all identified pathways FDR < 0.05 (15) for both *CERS2* and *CERS5/6* KDs. The distinct biological modules that emerged were used to label the volcano plots demonstrating pathway changes due to each KD.

2.3 Results

2.3.1 Validation of the adult immortalized human ventricular cardiomyocytes

Initially, studies for this project were completed using three separate cell lines: a pseudo primary human ventricular cardiomyocyte cell line purchased from Celprogen (#36044-15; Torrance, CA), an immortalized human ventricular cardiomyocyte cell line, called AC-16 cells, purchased from ATCC (#CRL-3568; Manassas, VA), and immortalized HCMs purchased from Applied Biological Materials (#T0519; Bellingham, WA). In all of the cardiomyocyte cell lines, *CERS* KDs were performed and optimized to achieve > 80% KD efficiency. Sphingolipids were also quantified, and the results suggested that all the KDs led to the expected reductions in ceramide species. Results between cell lines were comparable, so we leaned on RNA-sequencing results to aid in selecting the most biologically relevant model.

Initial comparisons between Celprogen’s cardiomyocytes, validated by Evangelista et al. (16), and AC-16 cells suggested that the Celprogen cells contained more of our expected cardiac

markers, leading us to believe the AC-16 cells had more of a cardiac fibroblast phenotype. Our main concern with Celprogen's cells began when attempting to develop a cardiac hypertrophy model, as these cells lacked the expression of any reliable hypertrophy marker, and treatment with the hypertrophy inducing compounds resulted in severe day-to-day inconsistencies. This ultimately led us to search for a new cardiomyocyte cell line. At this point we found the immortalized HCMs supplied by Applied Biological Materials that had been previously validated by two separate groups (17,18). An RNA-sequencing analysis between these cells and Celprogen's cardiomyocytes suggested that the new cells had a healthier ventricular cardiomyocyte phenotype as indicated by a more physiologically relevant expression of cardiac markers: *GATA4*, *ACTB*, *SMAD2*, *VEGFB*, *NPPB*, *CAMK2D*, and *CLCN3*. Additionally, the baseline expression of *NPPB*, allowed us to use this clinical biomarker to indicate hypertrophic cells, thus giving us the ability to compare results between sample types prior to sending samples for RNA-sequencing. For all these reasons, we deemed the HCMs from Applied Biological Materials to be the most biologically relevant cardiomyocyte model to study cardiac hypertrophy and all subsequent experiments were completed with this cell line only.

From the preliminary RNA-sequencing work, we were able to confirm the expression of the different *CERS* in the HCMs (**Figure 2.1**). Notably, as was the case with the *CERS* expression in all of the cardiomyocyte cell lines we examined, *CERS2* expression was the highest, followed by *CERS5* and *CERS6* expression. Since CerS2 is responsible for the production of the proposed protective (22:0 and 24:0) ceramides, and CerS5/CerS6 are both responsible for the generation of the suggested detrimental (16:0) ceramide, we divided the experimental groups up as such combining the knockdown of CerS5/6. Importantly, there are a few points that are worth discussing before presenting the results, the first being that it is known

that exogenous ceramide addition may redistribute in a non-physiological manner in the cell (19–21), therefore, we only considered conducting experiments to genetically alter ceramide levels. Also of note, preliminary testing with CerS2 and CerS5/6 overexpression yielded no change in the cellular ceramide species. For this reason, we will only be presenting the data generated following the silencing of the relevant *CERS* in HCMs.

2.3.2 Ceramide synthase 2 (*CERS2*) knockdown

Silencing *CERS2* by 80% leads to significant reductions in the expected VLC ceramide levels. Knockdown conditions were optimized to maximize differences observed in the cellular response therefore we aimed for an average of ~80% *CERS2* KD (**Figure 2.2A**), which was consistent over time. Throughout the effort of optimizing the *CERS2* KD, we observed significant cell death with 80% KD (**Figure 2.2B**). Of note, to minimize cell death, conditions were optimized to achieve a 40-50% *CERS2* KD, which resulted in less cell death, but no changes in the VLC ceramide levels upon sphingolipid quantification. For this reason, we decided to proceed with the 80% KD despite the high percentage of cell death since we observed reductions in the expected ceramide species (**Figure 2.3**) and were able to isolate sufficient mRNA for sequencing.

A closer look at the different sphingolipid species measured suggests overall reductions in 22:0 and 24:0 sphingolipids with *CERS2* KD. As expected, we observed significant decreases in 22:0 and 24:0 ceramide as well as other sphingolipid species connected with a 22:0 or 24:0 FA. We also detected increased amounts of 16:0 and 18:0 hexosylceramides in *CERS2* KD compared to controls.

2.3.3 Global transcriptomic changes following *CERS2* knockdown

To assess the global effects of *CERS2* KD in HCMs, we began by applying DESeq2 analysis to the HCM transcriptome across *CERS2* KD and scramble controls. We observed clear separation between the *CERS2* KD and scramble controls using a principal component analysis (PCA), indicative of large transcriptome changes in the HCM gene expression profiles due to KD (**Figure 2.4**). By applying a statistical threshold (FDR < 0.01) we identified just over 3,400 DEGs. **Figure 2.5** highlights the important DEGs that fall within the sphingolipid metabolic scheme divided up by specific sectors, ranging from the FA elongation cycle to complex sphingolipid metabolism. More information on the sphingolipid metabolic scheme can be found in **Figure 1.2**.

To further elucidate the transcriptional consequences of *CERS2* KD in HCMs, we applied a GSEA to systematically identify transcriptome perturbations due to *CERS2* KD. GSEA is a powerful tool used to extract biological insight from gene expression data. This tool is unique among others, as it not only focuses on groups of genes that share a common function, but it takes into consideration the significance of each gene change within each respective treatment (11,12). A comprehensive look at the hallmark and canonical pathways uncovered 420 upregulated and 328 downregulated pathways (FDR < 0.05). **Figure 2.6** depicts a volcano plot that is representative of the diverse pathways altered due to *CERS2* KD in HCMs. Many of these highlighted pathways are important for both proper cardiac function and cellular homeostasis. Of note, following *CERS2* KD, we observed increases in pathways involved in development and remodeling, fibrosis development, and lipid dysregulation. Furthermore, we detected downregulations in genes involved in mitochondrial biogenesis, cholesterol biosynthesis, and the cell cycle.

2.3.4 Ceramide synthase 5 and 6 (*CERS5/6*) knockdown

To reduce the concentrations of cellular 16:0 ceramide, a double KD, using *CERS5* and *CERS6* siRNA was optimized, as the two proteins encoded by these genes are responsible for the production of 16:0 ceramide and both genes are observed in HCMs. Dual KD of *CERS5* and *CERS6* at ~80% each (**Figure 2.7A**) leads to a significant reduction in 16:0 ceramide and a 25% reduction in cell viability (**Figure 2.7B**). With this KD, as expected, we observed significant decreases in the LC 14:0 and 16:0 ceramides when compared to controls (**Figure 2.8**). Notably, we detected overall reductions in the measured 14:0 and 16:0 sphingolipids, as well as increased VLC 24:0 ceramide and SM.

2.3.5 Global transcriptomic changes following *CERS5/6* knockdown

Similar to *CERS2* KD, we began by applying a DESeq2 analysis to the HCM transcriptome across the *CERS5/6* KD and scramble controls. As with silencing *CERS2*, we observed large changes in the transcriptome indicated by the clear separation of sample groups in a PCA plot (**Figure 2.9**). Application of an FDR < 0.01 led to identification of about 3,700 DEGs. Important DEGs in sphingolipid metabolism identified between the *CERS5/6* KD and scramble control samples are depicted in **Figure 2.10**, and reference can be made to **Figure 1.2** to visualize this sphingolipid metabolic scheme.

GSEA pathway analysis uncovered many changes in pathways necessary for cellular homeostasis following *CERS5/6* KD. A closer look at the transcriptome alterations with GSEA revealed 275 upregulated and 212 downregulated pathways (FDR < 0.05). A representative volcano plot is depicted in **Figure 2.11**, showcasing representative labels for many of the observed pathway changes. Interestingly, there are increases in the expression of genes and

pathways involved in DNA repair, cell cycle, and p53 signaling, while pathways for development and remodeling and cardiomyopathy were downregulated with *CERS5/6* KD.

2.3.6 Comparison between different *CERS* knockdowns

There is marked overlap in the DEGs and pathways observed between the *CERS2* and *CERS5/6* KDs compared to their respective controls but with inverse directionality. Of the DEGs (FDR < 0.01) observed in both the *CERS2* and the *CERS5/6* KD datasets, 60% were found to be inversely related **(Figure 2.12A),** where the gene was upregulated following *CERS2* KD, but downregulated with *CERS5/6* KD, or vice versa. A similar observation was made when comparing the GSEA results from both *CERS* KDs. Following GSEA analysis, 228 pathways were observed as being changed in both the *CERS2* and the *CERS5/6* KD datasets, 87% of which had opposite trends (**Figure 2.12B**). Taken together, these changes suggest that the different ceramide species contribute to cellular functions and homeostasis in an opposing fashion.

2.4 Discussion

2.4.1 Summary of results

In this study, we explored the consequences of altered sphingolipid homeostasis in the heart by silencing *CERS2* and *CERS5/6* in human ventricular cardiomyocytes to reduce cellular levels of 22:0 and 24:0 ceramides, and 16:0 ceramide, respectively. The key finding in this study is that the knockdown of *CERS2* and *CERS5/6* inversely modulate critical pathways that contribute to heart functionality. This study further supports that LC and VLC sphingolipids contribute differently to essential biological functions. We will start this discussion by addressing the *CERS* optimization process and the validation of the reduction in the respective ceramide

species. We will then break down the results from the transcriptomic pathway analyses and compare the HCM response to both *CERS2* and *CERS5/6* KD.

2.4.2 *CERS* knockdown leads to expected intracellular ceramide reductions

Initially, we began this study by silencing the specific ceramide synthases responsible for producing ceramides with a particular fatty acid chain length, as ceramides are the central metabolites in sphingolipid metabolism and, therefore should affect downstream sphingolipid species. Since *CERS2* is responsible for the production of VLC ceramides, 22:0 and 24:0, and *CERS5* and *CERS6* are both responsible for the generation of 16:0 ceramide, we chose these three gene targets to comprise our two different experimental groups. For this study, we chose to explore the most biologically relevant cardiomyocytes of the three initially tested in order to draw the most physiologically relevant conclusions, and we confirmed the expression of the *CERS* in these cells (**Figure 2.1**). Conditions were optimized to observe an 80% KD of both *CERS2* and *CERS5/6*, but notably, both experimental groups led to a reduction in HCM viability. *CERS2* KD appeared to be the more toxic genetic manipulation, since the silencing of *CERS2* resulted in a 70% reduction in viability.

To confirm that 80% KD led to biological changes, we quantified sphingolipid species using HPLC-MS/MS following *CERS2* and *CERS5/6* KD and detected widespread changes with both experimental conditions. With the KD of *CERS2*, as expected, we observed reductions in the potentially protective VLC ceramides, 22:0 and 24:0. Since ceramide is the central mediator of sphingolipid metabolism, it is not surprising that we observed similar reductions in the VLC complex sphingolipids: lactosylceramide (LacCer), hexosylceramide (HexCer), and SM. Interestingly, we observed a potential compensatory increase in LC HexCer following *CERS2* KD. In 2011, Mullen et. al provided evidence that the different CerS are tightly interregulated in

MCF-7 cells and that *CERS2* KD resulted in potential compensatory increases in LC sphingolipids to help maintain overall cellular sphingolipid levels (22) providing further support of our findings. Overall, with *CERS2* KD we observed the most changes in the HexCer species, which encompasses both glucosylceramide (GlcCer) and galactosylceramide (GalCer). There is experimental evidence suggesting that GlcCer levels in the heart are crucial for maintaining HCM membrane lipids, and slight alterations in GlcCer composition can contribute to reduced heart function (23). Therefore, it is possible that the drastic cell death is, in part, a consequence of altered HexCer concentrations. Of note, we did attempt to alter the KD conditions to get roughly 40% KD of *CERS2* following RT-qPCR analysis, but there was no observed change in any of the ceramide species. Additionally, we attempted to shorten the KD time to 48h, but this led to minimal changes in cell viability when compared to the 72h KD. For this reason, we chose to continue with the 72h 80% KD for further analysis despite the observed large degree of cell death since we can still measure changes in the different sphingolipids and isolate adequate quantities of RNA for sequencing.

A closer look at the sphingolipid changes with *CERS5/6* KD detected the expected reduction in 16:0 ceramide, as well as reduction in all measured 16:0 sphingolipids: LacCer, HexCer, and SM. Interestingly, we also saw a potential compensatory increase in the VLC sphingolipids, 24:0 ceramide and SM, while 24:0 LacCer was reduced. Notably, SM concentrations were the most extensively altered sphingolipid species measured following *CERS5/6* KD. These changes in SM species may suggest an alteration in plasma membrane composition and fluidity (24–26).

2.4.3 Pathway changes within the cardiomyocytes due to *CERS* knockdown

Our transcriptomic analysis with the *CERS* KDs suggests that ceramides play many vital biological roles within the HCMs. Following DESeq2 analyses, we observed a significant number of DEGs and importantly noted many changes in the sphingolipid metabolic scheme. In support of our findings that the VLC and LC ceramides may undergo compensatory interregulation, with *CERS2* KD, we observe an significance increase in *CERS5* expression (**Figure 2.5**), while with *CERS5/6* KD, we observed a significant increase in *CERS2* expression (**Figure 2.10**).

The GSEA pathway analyses pointed to many contrasting results with *CERS2* KD (**Figure 2.6**) compared to *CERS5/6* KD (**Figure 2.11**). With *CERS2* KD, we observed increases in HCM extracellular matrix (ECM) organization and lipid metabolism. Furthermore, we detected reduced activation of pathways that regulate mitochondrial biogenesis, cholesterol metabolism, and the cell cycle. Intriguingly, although these cells have not been treated with any external compounds aside from the siRNA, it appears the HCMs with silenced *CERS2* are developing an unhealthy cardiomyocyte phenotype. ECM organization is indicative of cardiac remodeling (27), a hallmark for CVD pathophysiology, and dysregulations in lipid and energy metabolism may suggest the HCMs are struggling to meet the same energy requirements as healthy cardiac cells (28–31). Taken together, these findings suggest that *CERS2* silencing has very negative impacts on HCM health. Interestingly, we observed the opposite effect with *CERS5/6* KD, with increases in the cell cycle and energy metabolism and decreases in development and remodeling. These changes suggest that while *CERS2* KD may be detrimental to HCM health, *CERS5/6* KD may provide positive changes in HCM health and functionality. Notably, we also observed increases in cardiovascular disease pathways with *CERS2* KD and

decreases in cardiovascular disease pathways following *CERS5/6* KD. Taken together, these findings bolster the hypothesis that 16:0 ceramide plays a negative role in heart failure progression, while VLC ceramides 22:0 and 24:0 may play a more protective role against heart failure development.

Although we address changes observed to the hypertrophic response with *CERS2* and *CERS5/6* KD in **Chapter 3**, there are a few key points to discuss about the observed changes to cardiomyocyte homeostasis resulting from the knockdowns. First, when a single gene is silenced, the number of crucial genes or pathways altered are usually not this large. Although it appears that with *CERS5/6* KD, the observed changes may be indicative of better functioning cardiomyocytes, the vast number of gene changes observed could be suggestive that a long-term treatment with a CerS inhibitor could potentially cause toxicity. Furthermore, since it appears the CerS proteins are so complexly interregulated, caution is warranted when inhibiting any of the individual CerS enzymes, as this could have negative consequences in other bodily function aspects, similar to the fumonisins (32,33). For this reason, these findings are promising in the sense that we could develop a CerS2 inducer or activator, which could yield more positive results as opposed to inhibiting the CerS5/6 enzymes. Altogether, increasing the potentially protective VLC ceramides could be a viable treatment to explore in the future. Due to the large amount of observed cell death with 80% *CERS2* KD, it is possible that increasing VLC ceramides could be protective beyond CVD.

2.5 Conclusions

We have demonstrated that altering sphingolipid composition in HCMs leads to vastly different cellular responses, with opposing changes in cellular remodeling and energy metabolism, suggesting that *CERS2* KD and *CERS5/6* KD led to detrimental and protective

responses in HCMs, respectively. The findings in this study suggest that since modifying ceramides species leads to alterations in the respective downstream sphingolipid species, more work is necessary to characterize the effect of each ceramide species on cardiomyocyte homeostasis. This work lays the foundation for investigating if altering the ceramide species through compounds directed at specific sphingolipid producing enzymes could represent a viable treatment option to combat heart disease. Further experimentation on how altering the sphingolipid levels in HCMs change the cellular response to cardiac hypertrophy, a hallmark of heart failure progression, is necessary and will be presented in **Chapter 3**.

Figures

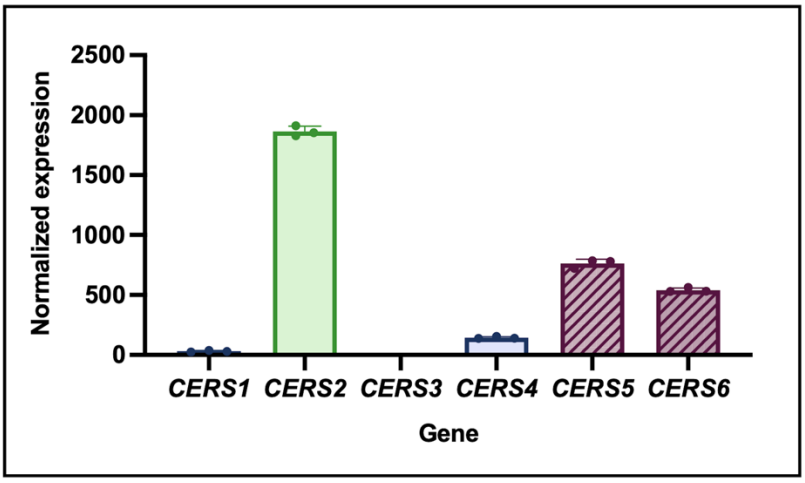

Figure 2.1. CERS gene expression in HCMs from RNA-sequencing data.

Normalized CERS expression confirming the expression of the different *CERS* in immortalized human ventricular cardiomyocytes, n=3.

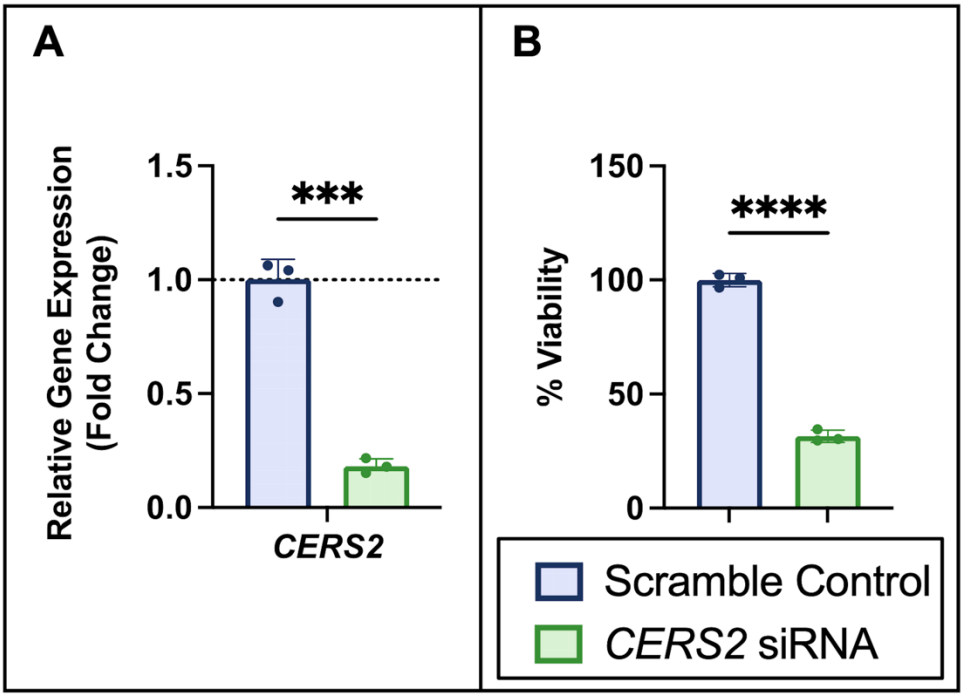

Figure 2.2. Optimized ~ 80% *CERS2* KD leads to significant cell death.

(**A**) Treatment with *CERS2* siRNA leads to 82% KD of *CERS2*. (**B**) Cell viability following 72h knockdown of *CERS2* compared to the scramble control. n=3, **** P <0.0001, *** P < 0.001

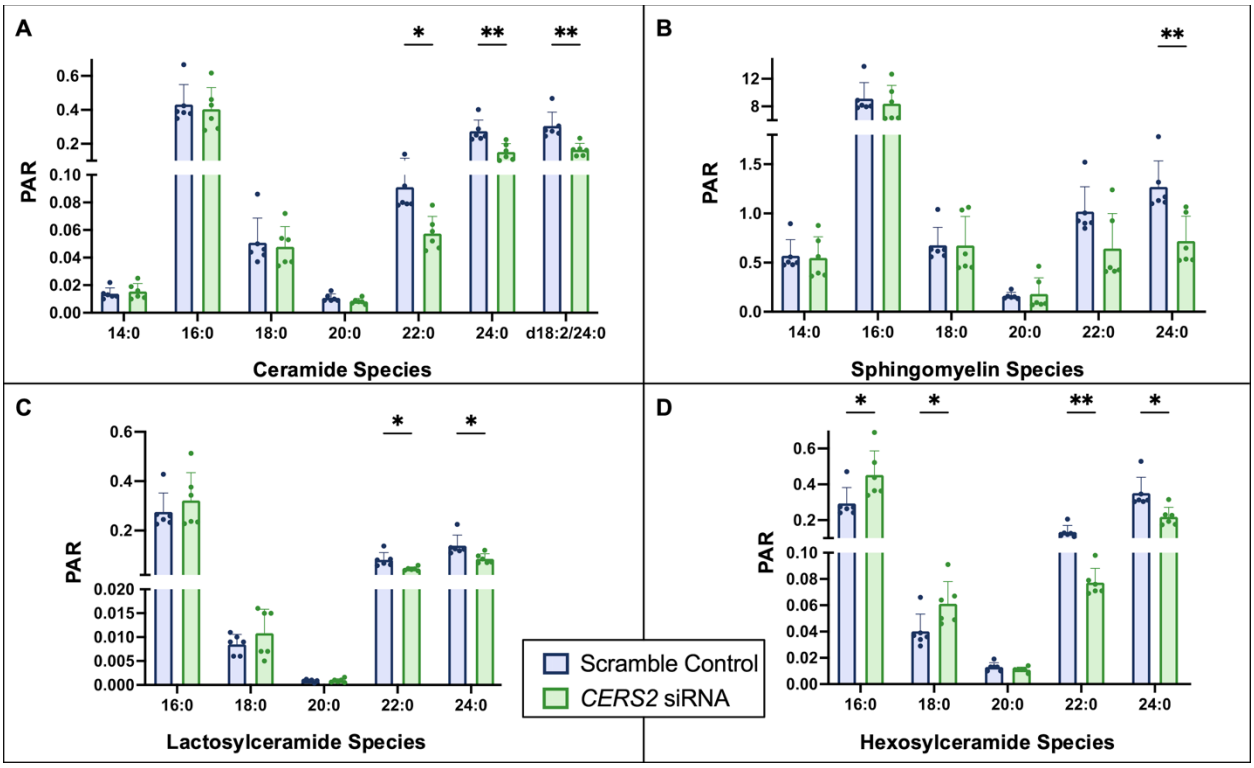

Figure 2.3. Quantification of sphingolipid species changes with 72h *CERS2* KD according to class.

(**A**) ceramide, (**B**) sphingomyelin, (**C**) lactosylceramide, and (**D**) hexosylceramide. Unless otherwise noted, all species had an 18:1 sphingosine backbone. Two sets of n=3 sample collections resulting in an n=6, ** $P < 0.01$, * $P < 0.05$

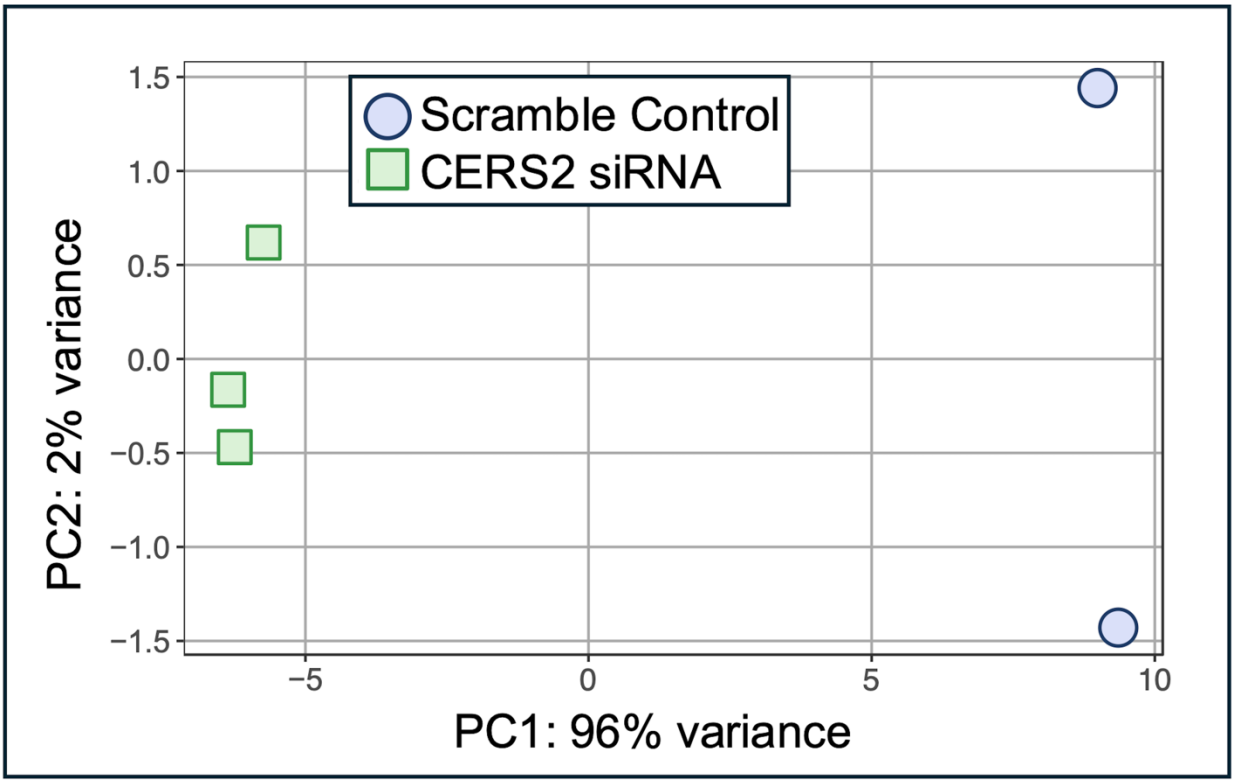

Figure 2.4. Transcriptome variation between *CERS*2 KD and scramble control samples.

PCA plot across the HCM transcriptome in *CERS2* KD samples (green boxes) and scramble control (blue circles).

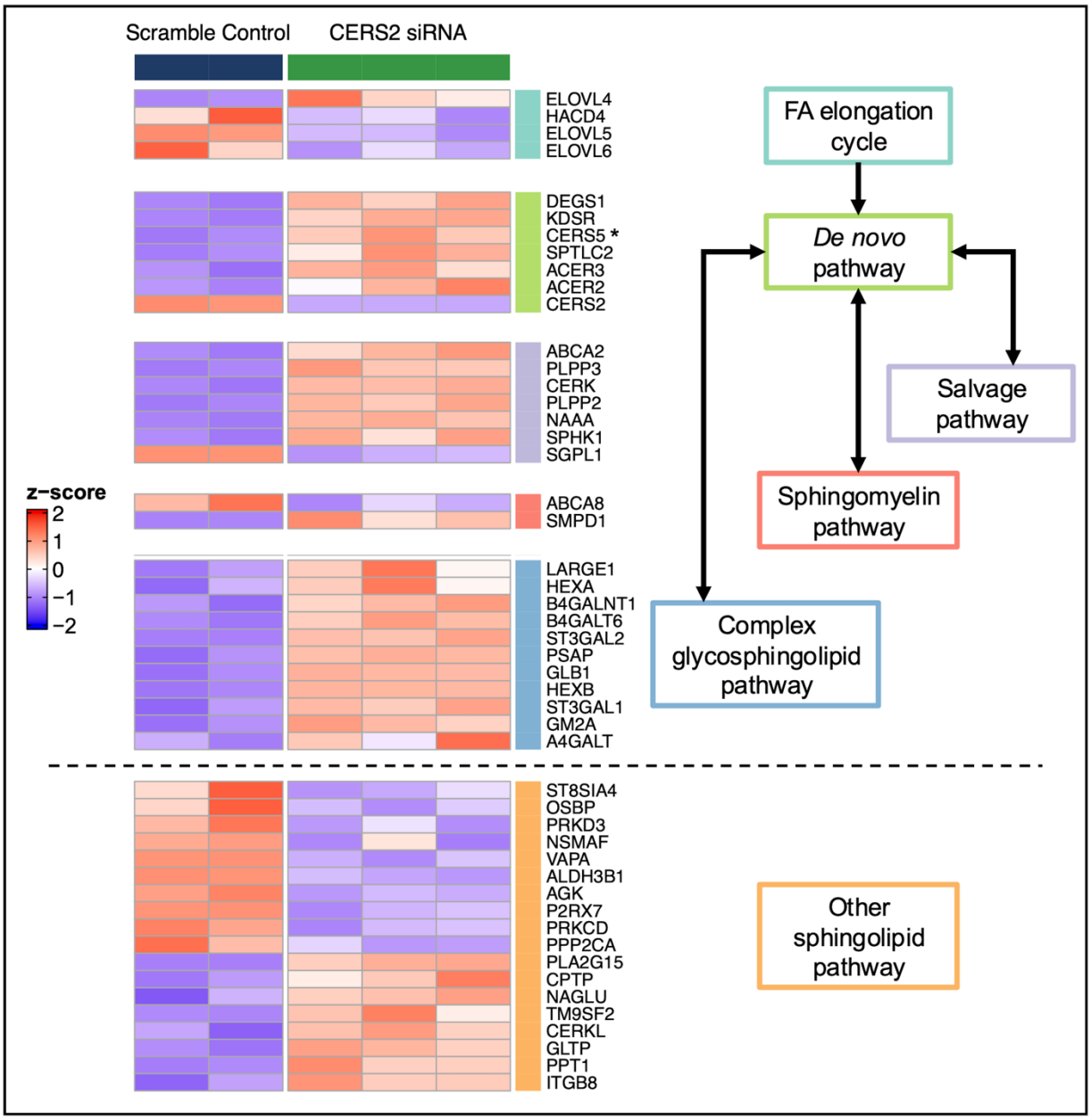

Figure 2.5. DEGs within the sphingolipid metabolic scheme identified with *CERS2* KD.

Genes important to sphingolipid metabolism (FDR < 0.05) highlighted due to *CERS2* KD. A positive z-score (red) indicates higher expression, while a lower z-score (blue) indicates lower expression. * Signifies potential interregulation within the *CERS.* FA – fatty acid

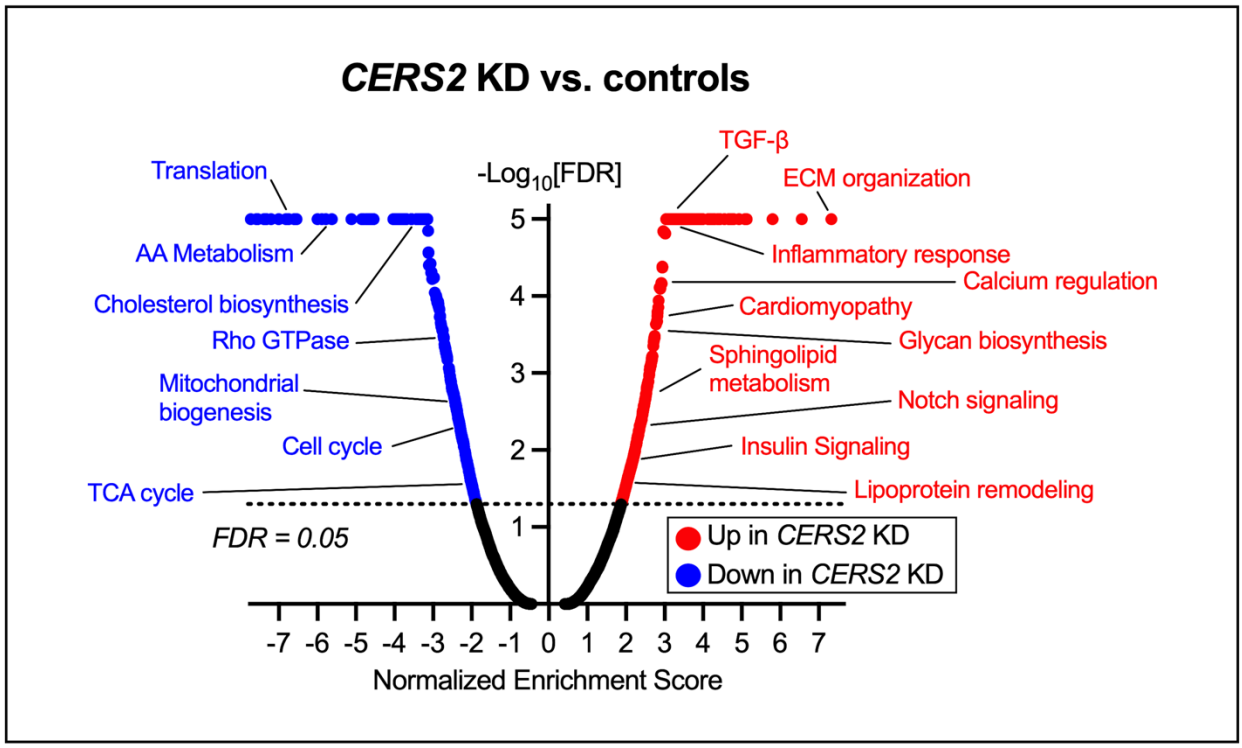

Figure 2.6. Volcano plot with labels encompassing several pathways altered due to *CERS2* KD in HCMs.

The highlighted pathways are representative of the vast changes observed in the *CERS2* KD and further represent important pathways for heart function and cellular homeostasis. AA – amino acid, TCA – tricarboxylic acid, ECM – extracellular matrix

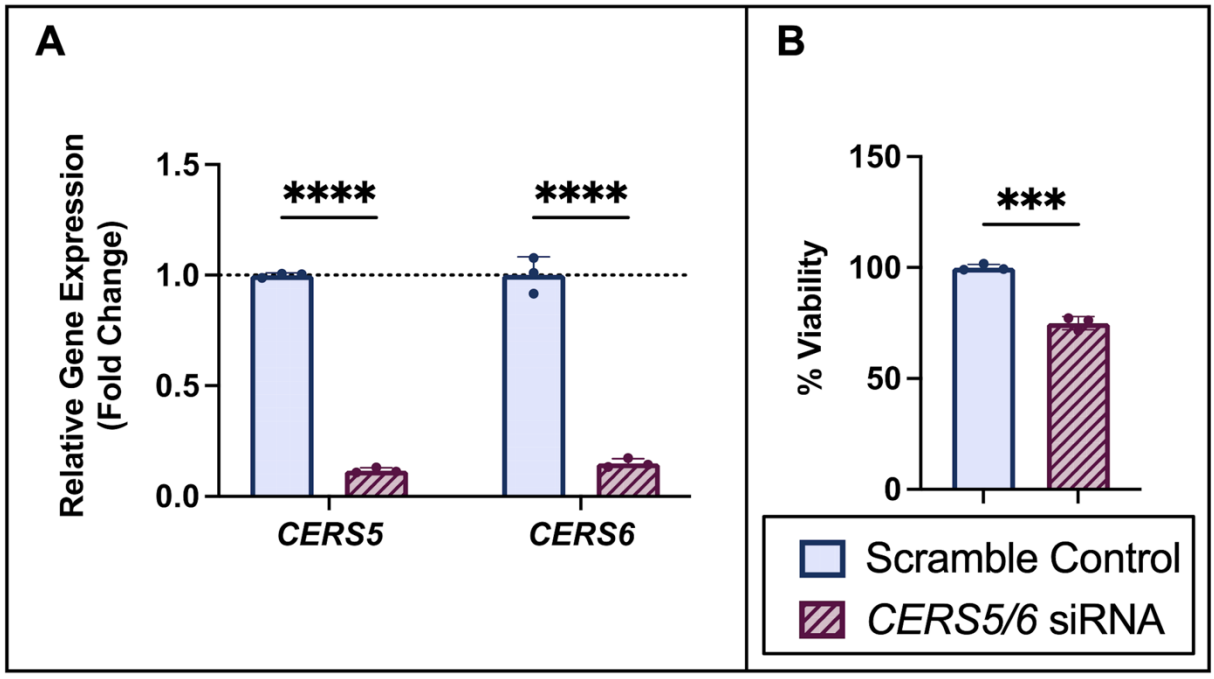

Figure 2.7. Optimized ~80% *CERS5/6* KD leads to small amounts of cell death.

(**A**) Treatment with *CERS5* and *CERS6* siRNA leads to 88% KD of *CERS5* and 85% KD of *CERS6*. (**B**) HCM viability declines to 75% following 72h *CERS5* and *CERS6* KD. n=3, **** $P < 0.0001$, *** $P < 0.001$

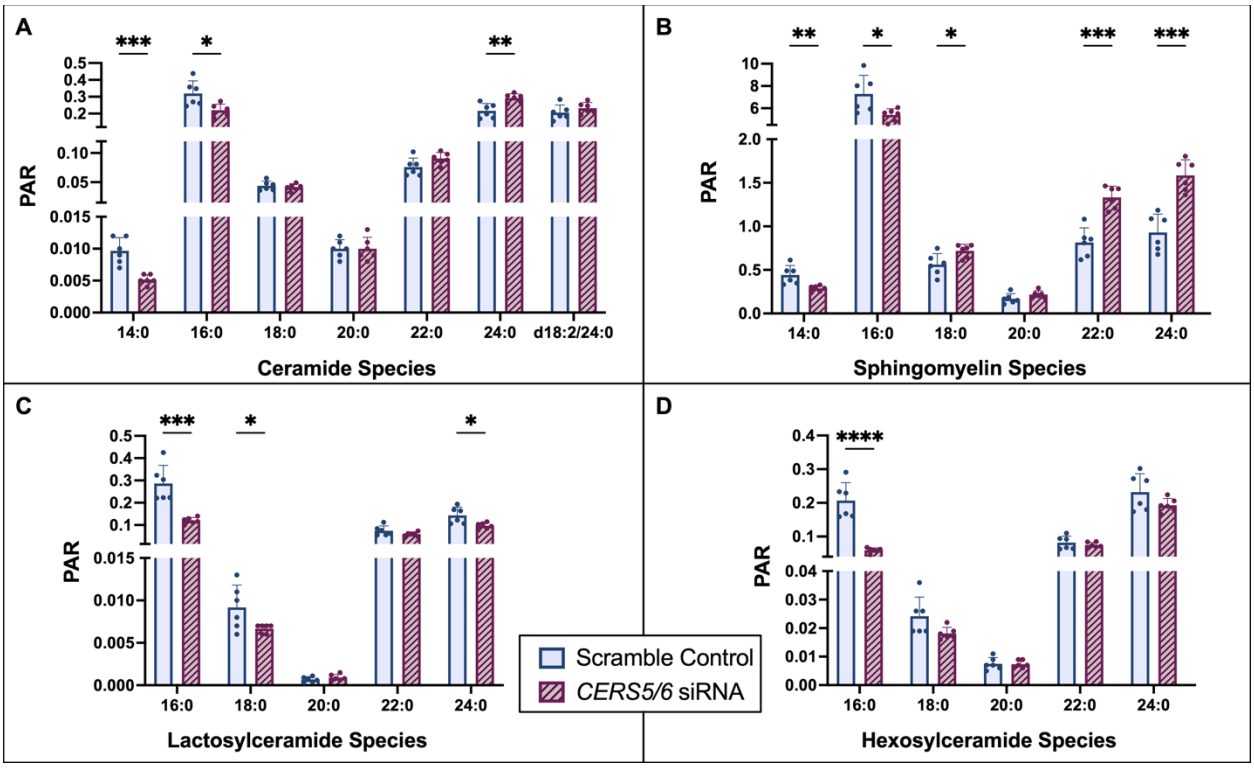

Figure 2.8. Quantification of sphingolipid species changes with 72h *CERS5/6* KD grouped by species.

(**A**) ceramide, (**B**) sphingomyelin, (**C**) lactosylceramide, and (**D**) hexosylceramide. Unless otherwise noted, all species had an 18:1 sphingosine backbone. Two sets of n=3 sample collections resulting in an n=6, **** $P < 0.0001$, *** $P < 0.001$, ** $P < 0.01$, * $P < 0.05$

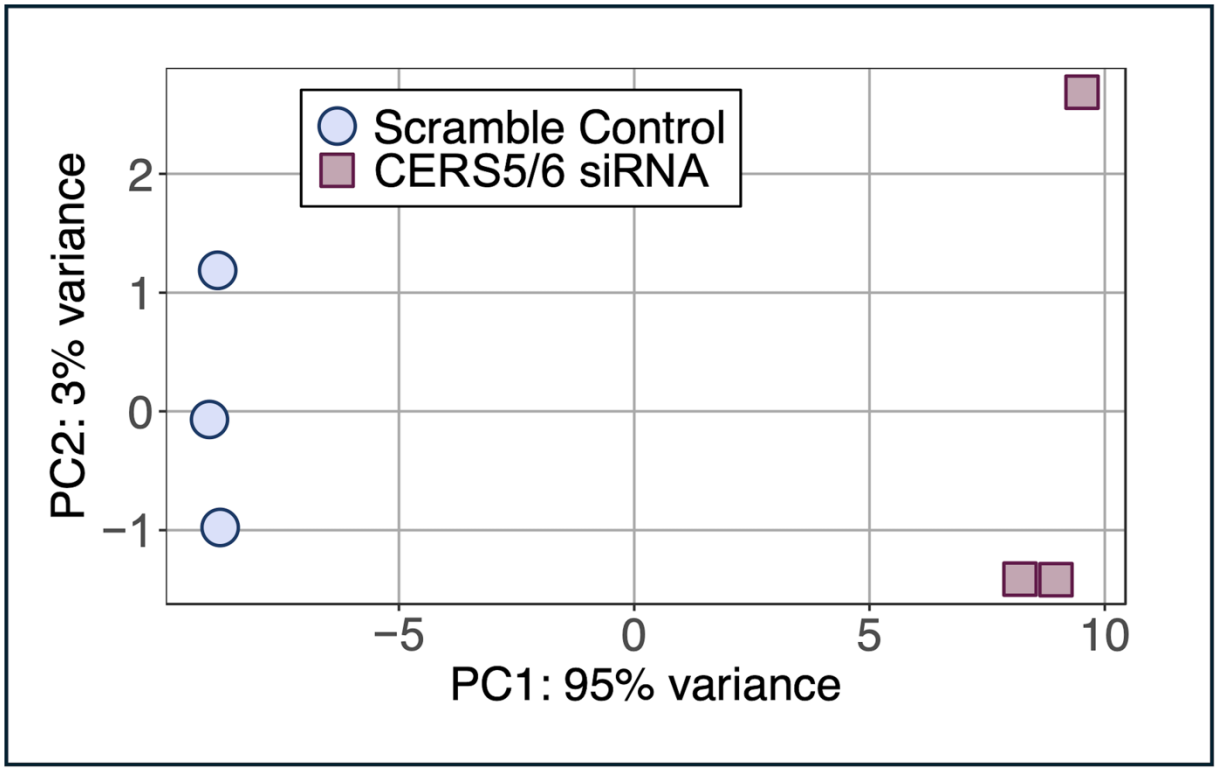

Figure 2.9. Transcriptome variation between *CERS*5/6 KD and scramble control samples.

PCA plot across the HCM transcriptome in *CERS5/6* KD samples (purple boxes) and scramble control (blue circles).

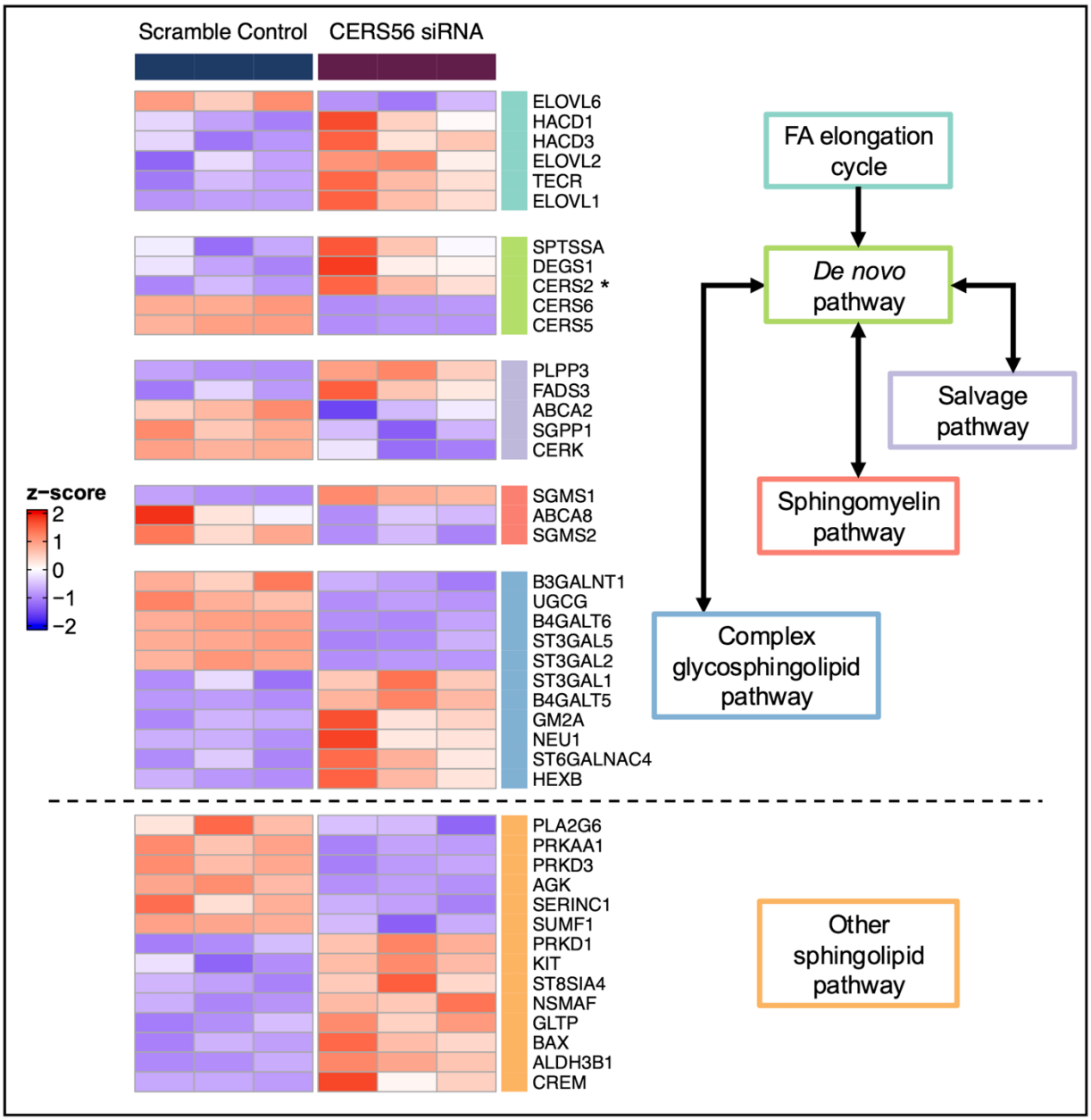

Figure 2.10. DEGs within the sphingolipid metabolic scheme identified with *CERS5/6* KD.

Genes important to sphingolipid metabolism (FDR < 0.05) highlighted due to *CERS5/6* KD. A positive z-score (red) indicates higher expression, while a lower z-score (blue) indicates lower expression. * Signifies potential interregulation within the *CERS*. FA – fatty acid

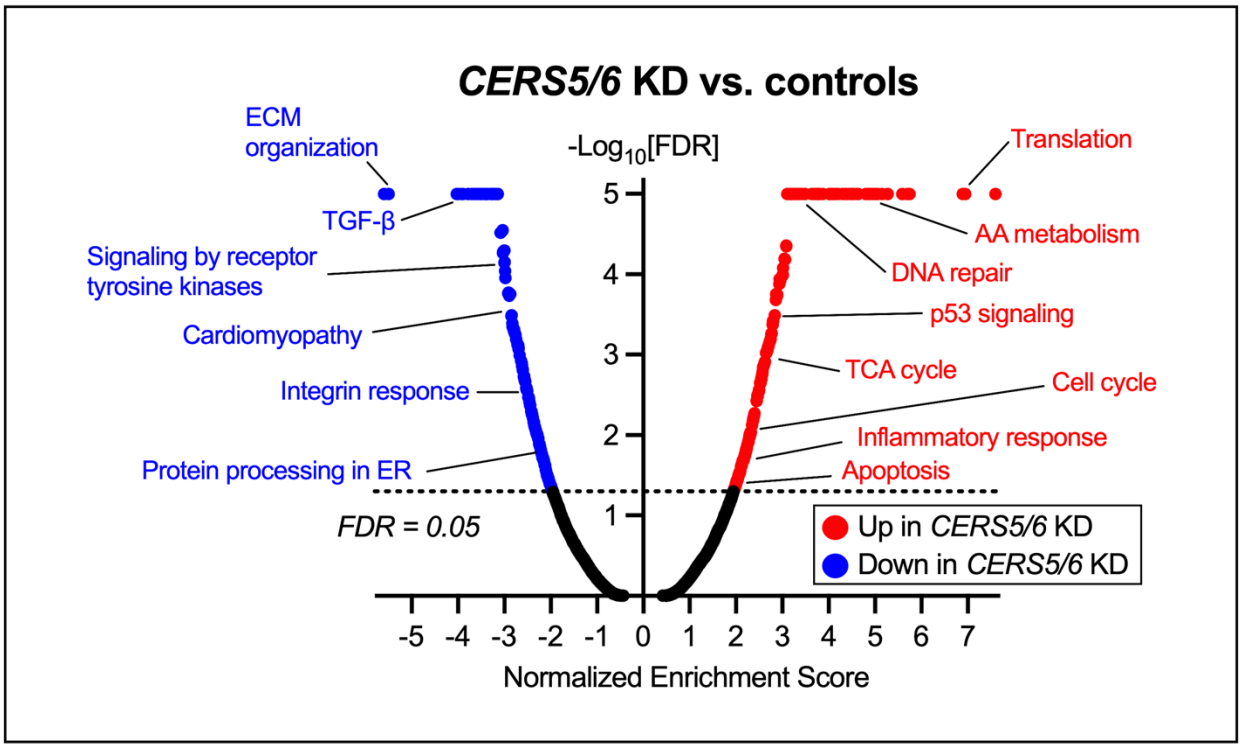

Figure 2.11. Volcano plot labeling representative pathways altered due to *CERS5/6* KD in HCMs.

Many of the observed pathway changes are important for cellular homeostasis and heart function. ECM – extracellular matrix, ER – endoplasmic reticulum, AA – amino acid, TCA – tricarboxylic acid

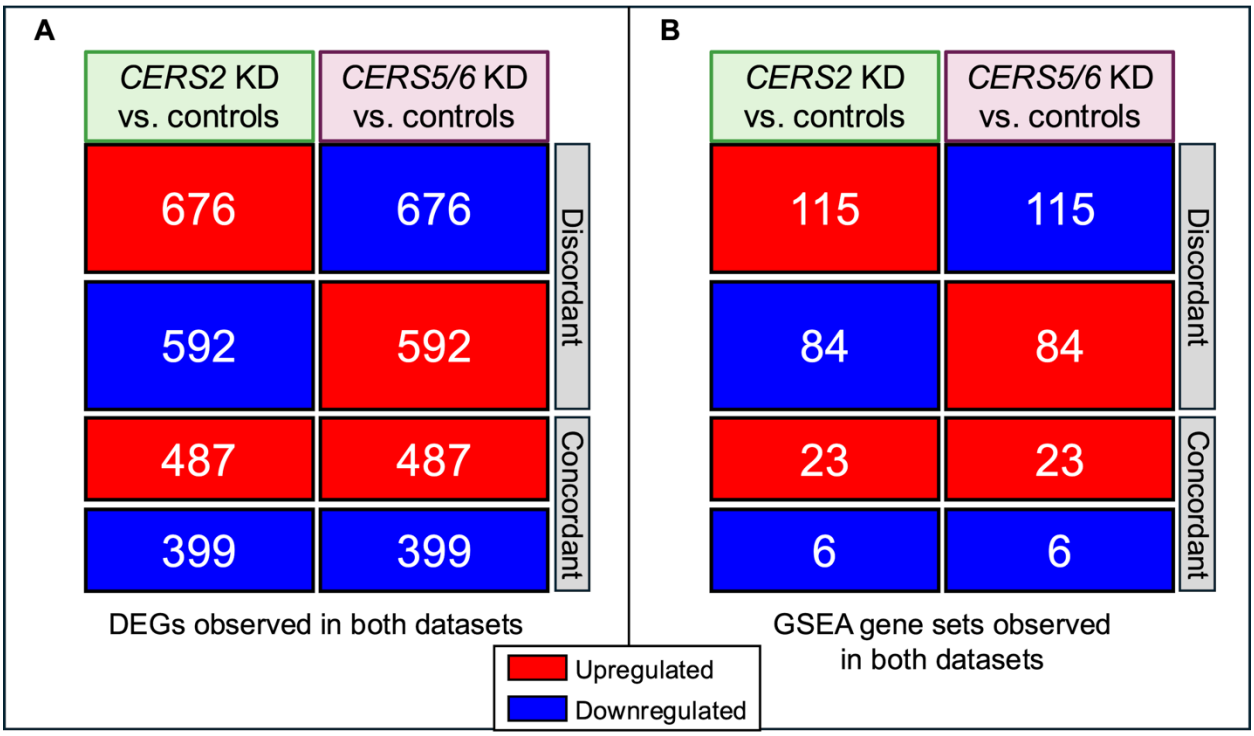

Figure 2.12. Comparison of the observed changes following either *CERS2* or *CERS5/6* KD.

Comparison of the identical up and downregulated (**A**) DEGs and (**B**) GSEA gene sets independently identified with *CERS2* and *CERS5/6* KDs.

References

1. Pralhada Rao R, Vaidyanathan N, Rengasamy M, Mammen Oommen A, Somaiya N, Jagannath MR. Sphingolipid Metabolic Pathway: An Overview of Major Roles Played in Human Diseases. J Lipids. 2013;2013:1–12.

2. Kuo A, Hla T. Regulation of cellular and systemic sphingolipid homeostasis. Nat Rev Mol Cell Biol [Internet]. 2024 Jun 18 [cited 2024 Jul 13]; Available from: https://www.nature.com/articles/s41580-024-00742-y

3. Ho QWC, Zheng X, Ali Y. Ceramide Acyl Chain Length and Its Relevance to Intracellular Lipid Regulation. Int J Mol Sci. 2022 Aug 26;23(17):9697.

4. Zietzer A, Düsing P, Reese L, Nickenig G, Jansen F. Ceramide Metabolism in Cardiovascular Disease: A Network With High Therapeutic Potential. Arterioscler Thromb Vasc Biol. 2022 Oct;42(10):1220–8.

5. Hammerschmidt P, Brüning JC. Contribution of specific ceramides to obesity-associated metabolic diseases. Cell Mol Life Sci. 2022 Aug;79(8):395.

6. Nicholson RJ, Poss AM, Maschek JA, Cox JE, Hopkins PN, Hunt SC, et al. Characterizing a Common CERS2 Polymorphism in a Mouse Model of Metabolic Disease and in Subjects from the Utah CAD Study. J Clin Endocrinol Metab. 2021 Jul 13;106(8):e3098–109.

7. De La Monte SM. Triangulated Mal-Signaling in Alzheimer's Disease: Roles of Neurotoxic Ceramides, ER Stress, and Insulin Resistance Reviewed. Frisardi V, Imbimbo B, editors. J Alzheimers Dis. 2012 Jun 8;30(s2):S231–49.

8. Lemaitre RN, Jensen PN, Hoofnagle A, McKnight B, Fretts AM, King IB, et al. Plasma Ceramides and Sphingomyelins in Relation to Heart Failure Risk: The Cardiovascular Health Study. Circ Heart Fail. 2019 Jul;12(7):e005708.

9. Lemaitre RN, Yu C, Hoofnagle A, Hari N, Jensen PN, Fretts AM, et al. Circulating Sphingolipids, Insulin, HOMA-IR, and HOMA-B: The Strong Heart Family Study. 2018;67.

10. Love MI, Huber W, Anders S. Moderated estimation of fold change and dispersion for RNA-seq data with DESeq2. Genome Biol. 2014 Dec;15(12):550.

11. Subramanian A, Tamayo P, Mootha VK, Mukherjee S, Ebert BL, Gillette MA, et al. Gene set enrichment analysis: A knowledge-based approach for interpreting genome-wide expression profiles. Proc Natl Acad Sci. 2005 Oct 25;102(43):15545–50.

12. Mootha VK, Lindgren CM, Eriksson KF, Subramanian A, Sihag S, Lehar J, et al. PGC-1α-responsive genes involved in oxidative phosphorylation are coordinately downregulated in human diabetes. Nat Genet. 2003 Jul;34(3):267–73.

13. Liberzon A, Birger C, Thorvaldsdóttir H, Ghandi M, Mesirov JP, Tamayo P. The Molecular Signatures Database Hallmark Gene Set Collection. Cell Syst. 2015 Dec;1(6):417–25.

14. Liberzon A, Subramanian A, Pinchback R, Thorvaldsdóttir H, Tamayo P, Mesirov JP. Molecular signatures database (MSigDB) 3.0. Bioinformatics. 2011 Jun 15;27(12):1739–40.

15. Cline MS, Smoot M, Cerami E, Kuchinsky A, Landys N, Workman C, et al. Integration of biological networks and gene expression data using Cytoscape. Nat Protoc. 2007 Oct;2(10):2366–82.

16. Evangelista EA, Kaspera R, Mokadam NA, Jones JP, Totah RA. Activity, Inhibition, and Induction of Cytochrome P450 2J2 in Adult Human Primary Cardiomyocytes. Drug Metab Dispos. 2013 Dec;41(12):2087–94.

17. Durham KK, Chathely KM, Mak KC, Momen A, Thomas CT, Zhao YY, et al. HDL protects against doxorubicin-induced cardiotoxicity in a scavenger receptor class B type 1-, PI3K-, and Akt-dependent manner. Am J Physiol-Heart Circ Physiol. 2018 Jan 1;314(1):H31–44.

18. Kono K, Sawada R, Kuroda T, Yasuda S, Matsuyama S, Matsuyama A, et al. Development of selective cytotoxic viral vectors for concentration of undifferentiated cells in cardiomyocytes derived from human induced pluripotent stem cells. Sci Rep. 2019 Mar 6;9(1):3630.

19. Grösch S, Schiffmann S, Geisslinger G. Chain length-specific properties of ceramides. Prog Lipid Res. 2012 Jan;51(1):50–62.

20. Ogretmen B, Pettus BJ, Rossi MJ, Wood R, Usta J, Szulc Z, et al. Biochemical Mechanisms of the Generation of Endogenous Long Chain Ceramide in Response to Exogenous Short Chain Ceramide in the A549 Human Lung Adenocarcinoma Cell Line. J Biol Chem. 2002 Apr;277(15):12960–9.

21. Kitatani K, Idkowiak-Baldys J, Hannun YA. The sphingolipid salvage pathway in ceramide metabolism and signaling. Cell Signal. 2008 Jun;20(6):1010–8.

22. Mullen TD, Spassieva S, Jenkins RW, Kitatani K, Bielawski J, Hannun YA, et al. Selective knockdown of ceramide synthases reveals complex interregulation of sphingolipid metabolism. J Lipid Res. 2011;52(1):68–77.

23. Andersson L, Cinato M, Mardani I, Miljanovic A, Arif M, Koh A, et al. Glucosylceramide synthase deficiency in the heart compromises b1-adrenergic receptor trafficking.

24. Milhas D, Clarke CJ, Hannun YA. Sphingomyelin metabolism at the plasma membrane: Implications for bioactive sphingolipids. FEBS Lett. 2010 May 3;584(9):1887–94.

25. Dorrance A. Increased membrane sphingomyelin and arachidonic acid in stroke-prone spontaneously hypertensive rats. Am J Hypertens. 2001 Nov;14(11):1149–53.

26. Shinitzky M, Barenholz Y. Dynamics of the Hydrocarbon Layer in Liposomes of Lecithin and Sphingomyelin Containing Dicetylphosphate. J Biol Chem. 1974 Apr;249(8):2652–7.

27. Kehat I, Molkentin JD. Molecular Pathways Underlying Cardiac Remodeling During Pathophysiological Stimulation. Circulation. 2010 Dec 21;122(25):2727–35.

28. Gandoy-Fieiras N, Gonzalez-Juanatey JR, Eiras S. Myocardium Metabolism in Physiological and Pathophysiological States: Implications of Epicardial Adipose Tissue and Potential Therapeutic Targets. Int J Mol Sci. 2020 Apr 10;21(7):2641.

29. Goldberg IJ, Trent CM, Schulze PC. Lipid Metabolism and Toxicity in the Heart. Cell Metab. 2012 Jun;15(6):805–12.

30. Schulze PC, Drosatos K, Goldberg IJ. Lipid Use and Misuse by the Heart. Circ Res. 2016 May 27;118(11):1736–51.

31. Yamamoto T, Sano M. Deranged Myocardial Fatty Acid Metabolism in Heart Failure. Int J Mol Sci. 2022 Jan 17;23(2):996.

32. Riley RT, Merrill AH. Ceramide synthase inhibition by fumonisins: a perfect storm of perturbed sphingolipid metabolism, signaling, and disease. J Lipid Res. 2019 Jul;60(7):1183–9.

33. Janneh AH, Ogretmen B. Targeting Sphingolipid Metabolism as a Therapeutic Strategy in Cancer Treatment. Cancers. 2022 Apr 27;14(9):2183.

Chapter 3: The Impact of Altering Long-Chain and Very Long-Chain Ceramides on the Cardiomyocyte's Hypertrophic Response

3.1 Introduction

Ceramides are members of the sphingolipid class and constitute the central metabolite essential for the formation of more complex sphingolipids, such as SM. Ceramides contain a sphingosine backbone with an acylated fatty acid of varying chain lengths that have been linked to a multitude of biological functions (1). Additionally, ceramides play a role in several processes of relevance to HF pathophysiology including promoting apoptosis, oxidative stress, endothelial dysfunction, inflammation, lipotoxicity, and insulin resistance (2–4). That said, in most experimental studies pertaining to ceramides thus far, researchers have been focused on studying the general ceramide backbone, instead of pinpointing one of over fifty distinct molecular ceramide species (5) and investigating the specific roles that each ceramide plays in health. More recent research efforts have focused on defining the roles that the ceramides with different fatty acid lengths play in cardiovascular disease CVD. It is important to note that since ceramide synthesis and metabolism is so complex and involves several compensatory pathways as portrayed in **Figure 1.2**, elucidating the distinct functions of different acyl-chain length ceramides is arguably a more robust question than examining the ceramide species together. This also helps tackle convolution in data interpretation since ceramides can be formed by different mechanisms in distinct cellular compartments and hence exert different functions.

In 2019, our colleagues published a manuscript describing the association of 16:0 plasma ceramide and SM with an increased risk of incident HF, while VLC 22:0 ceramide, and 20:0, 22:0, and 24:0 SM were associated with a decreased risk (6). This led us to hypothesize that altering these sphingolipid species would influence CVD progression and alter the biological

processes related to HF. In **Chapter 2**, we presented evidence that silencing the distinct ceramide synthases, *CERS2* and *CERS5/6*, responsible for the generation of 22:0 plus 24:0 ceramide, or 16:0 ceramide, respectively, resulted in vast changes to the transcriptome of immortalized human cardiomyocytes. In this chapter, we evaluate the effect of silencing *CERS2* and *CERS5/6* on the cardiomyocyte's hypertrophic response to probe our hypothesis that the lipid products generated by CerS2 are protective against cardiac hypertrophy, while the products of CerS5/6 are detrimental to the progression and development of hypertrophy.

3.1.1 Research Strategy

Here, we use cardiac hypertrophy as a surrogate for HF, since it is not feasible to induce HF in a cardiac cell model. This is a viable option given that hypertrophy is the hallmark of HF. We begin this chapter by introducing and validating our working hypertrophy model. We then utilize this model and run global transcriptomics to investigate how silencing the different *CERS* genes may impact the HCM response to hypertrophy. Throughout this chapter, we walk through two different computational approaches to tease out transcriptome changes specific to the hypertrophic response due to *CERS2* and *CERS5/6* KD – a likelihood ratio test (LRT) and a cluster analysis. This work is an important first step to uncovering the importance of the different ceramide species in the progression of heart failure.

3.2 Materials and Methods

3.2.1 Materials

The immortalized human ventricular cardiomyocytes and all consumables needed to maintain the myocytes including PriGrow I media, penicillin/strep, and extracellular matrix were supplied by Applied Biological Materials (Bellingham, WA). CERS2 siRNA and the universal

scramble control (#SR323951) were purchased from Origene (Rockville, MD). Silencer siRNA for CERS5 (#AM16708, siRNA ID #131807), CERS6 (#AM16708, siRNA ID #149485), and Silencer Negative Control #5 siRNA (#AM4642) were obtained through Invitrogen (Waltham, MA). Tissue culture treated plates, Lipofectamine 3000 Reagent, DMSO, Opti-MEM media, PBS, formaldehyde, Hoechst 33342 (#62249), Alexa Fluor 488 Phalloidin (#A12379), cell scrapers, RIPA lysis buffer, Halt protein and phosphatase inhibitor cocktail, BCA reagents and standards, dithiothreitol, electrophoresis system, PageRuler Plus Prestained Protein Ladder, NuPAGE 4-12% Bis-Tris gels, MOPS SDS Running Buffer, iBlot Transfer System, nitrocellulose transfer stacks, and RNA isolation kits were all obtained from Thermo Fisher Scientific (Waltham, MA). The anti-BNP antibody was purchased from Bioss Antibodies (Woburn, MA), while the anti-β-actin antibody was purchased from Cell Signaling (Danvers, MA). The secondary antibodies were obtained through LI-COR (Lincoln, NE). Phorbol 12-myristate 13-acetate was purchased from Cayman Chemicals (Ann Arbor, MI). Triton X-100 was purchased from Sigma Aldrich (Burlington, MA).

3.2.2 Cell culture

Immortalized human ventricular cardiomyocytes were cultured and passaged in an identical manner to that described in detail in **Chapter 2, Section 2.2.2**.

3.2.3 Hypertrophy treatment with *CERS2* and *CERS5/6* KDs

Gene silencing was accomplished following the same protocol and materials described in **Chapter 2, Section 2.2.3**. Cells were treated with 4 μM phorbol 12-myristate 13-acetate (PMA) or a comparative vehicle control (0.025% DMSO) in serum-free media 24h after the reverse transfection. With the *CERS5/6* combo KD and its respective control, HCMs were retreated with 2 μM PMA 24h after the start of the initial treatment, leading to a total 48h hypertrophy

treatment, while the initial PMA treatment was left as is in the *CERS2* KD to minimize cell death. After the completion of the 48h PMA treatment, the cells were used for further analyses described below.

3.2.4 Cell imaging

After the 48h PMA treatment, cells were washed and fixed with 4% methanol-free formaldehyde for 20 min (#FB002). Cells were then permeabilized with 0.1% Triton X-100 (#T8787) in PBS prior to being stained for 45 min in the dark. The stain solution consisted of Hoechst 33342 to stain for the nucleus, and Alexa Fluor 488 Phalloidin to stain for F-actin, using the manufacturer's recommended dilutions. Images were obtained at random using an EVOS M7000 Microscope at 40x. Following image procurement, images were analyzed using Celleste Image Analysis Software Version 6.0. An automated method for obtaining cell area was created where the sum of the membrane area was divided by the number of nuclei present, generating an average cell area for each respective image.

3.2.5 Western blotting

Following hypertrophy treatment, samples were lysed utilizing RIPA lysis buffer (#89901) and Halt Protease and Phosphatase Inhibitor Cocktail (#78440). To protein normalize the samples, BCA protein reagents (Reagent A, # 23228; Reagent B, #23224) and the Bovine Serum Albumin Pre-Diluted Standard Set (#23208) were used. Samples were reduced with 50 mM dithiothreitol (#A39255) and left to incubate at room temperature for 15 min. NuPAGE 4-12% Bis-Tris gels (#NP0336) were used with the XCell SureLock Mini-Cell Electrophoresis system, PageRuler Plus Prestained Protein Ladder (#26619), and MOPS SDS Running Buffer (#NP0001). The gel was transferred to a nitrocellulose transfer stack (#IB301001) using an iBlot Transfer System. For 90 min, the blot was blocked in blocking buffer consisting of: 5% w/v milk

powder, 5% w/v BSA, 0.1% v/v Tween 20, and 0.1% w/v sodium azide in PBS. A primary antibody incubation with a 1:1000 dilution of rabbit anti-β-actin antibody (#4970) and a 1:500 dilution of mouse anti-BNP antibody (#bsm-4579M-A647) was conducted overnight. This was followed by an hour-long room temperature incubation with secondary IRDye 680RD goat anti-rabbit (#926-68071) and IRDye 680RD goat anti-mouse (#926-68070) antibodies the next morning. Western blots were scanned using an Odyssey CLx gel scanner and images were visualized using Image Studio Version 4.0 software.

3.2.6 Total RNA isolation and mRNA-sequencing

RNA isolation and mRNA sequencing were run in an identical manner to that described in **Chapter 2, Sections 2.2.5** and **2.2.7**, respectively. To reiterate a note made in **Section 2.2.7**, based on the failure of one of the quality controls checks, one of the *CERS2* KD scramble controls was excluded from further analysis.

3.2.7 Bioinformatics and pathway analyses

3.2.7.A Gene expression analysis

The gene expression analysis was performed as described in **Chapter 2, Section 2.2.8.A**.

3.2.7.B Gene set enrichment analysis

GSEA analysis was conducted as detailed in **Chapter 2, Section 2.2.8.B**.

3.2.7.C LRT/Cluster analysis

To investigate the genes associated with the interaction between PMA treatment and genotype, we employed LRT within DESeq2 (7). Specifically, we compared the full model, including the interaction term, to a reduced model, without the interaction term. Genes exhibiting similar expression patterns across experimental conditions were subsequently clustered using k-

means analysis. The number of clusters were chosen to reduce the intra-group variance while maximizing the silhouette score.

3.2.7.D WebGestalt

In order identify pathway changes due to hypertrophy treatment with *CERS* KD, we utilized WebGestalt's over-representation analysis software (8). Using the default parameters, with a selected FDR < 0.05 and the functional pathway databases: KEGG, Panther, and Reactome, enrichment results were generated for the entirety of the LRT gene lists for both *CERS2* and *CERS5/6* KD. Additionally, analyses were performed with each gene list encompassed by the identified clusters. Any cluster that was not assigned a pathway in either **Figure 3.5B** or **Figure 3.7B** returned no significant biological pathways.

3.3 Results

3.3.1 Establishing a cardiac hypertrophy model

Cardiac hypertrophy is a disease characterized by enlarged cardiomyocytes and ventricular wall thickening, a condition that can be mimicked using cultured cardiac cells. Cardiac hypertrophy results in a decreased ability to pump blood throughout the body and an increased workload of the heart in order to maintain functionality. As a result, cardiac hypertrophy typically precedes the onset of HF (9). For this reason, we chose to develop a cardiac hypertrophy model to serve as our means to investigate HF, since HF cannot be reproduced in a cell culture model. We believed this represented a viable and testable way to investigate our research question; how do the 16:0, 22:0, and 24:0 ceramide species alter the heart's response to CVD progression?

Our experimental workflow began where we left off in **Chapter 2**; we silenced either *CERS2* or *CERS5/6*, then introduced a hypertrophy inducing compound to the genetically manipulated cells in order to investigate how endogenously modifying different levels of ceramide species in the cardiomyocyte altered the HCM's hypertrophic response. As mentioned in **Chapter 2, Section 2.3.1**, one of the reasons we selected to use the HCMs purchased from Applied Biological Materials was because these cells had a baseline level of *NPPB* that could serve as a biochemical marker to quantify hypertrophy levels within the cells. *NPPB* is the gene the encodes a protein known as BNP, which is currently the clinical gold standard biomarker for HF. Having a biochemical marker for this assay was imperative, since imaging experiments analyzing cell size are not conducive to comparison between experimental groups.

Initial experiments consisted of running dose-response curves with a panel of known hypertrophy inducing compounds: PMA, endothelin-1, isoproterenol, and angiotensin II. Preceding RT-qPCR analysis investigating *NPPB* expression, we decided to focus solely on PMA treatment since it produced a dose-dependent and consistent increase in *NPPB*. Additionally, it is worth mentioning that experiments were completed with myriocin, a potent inhibitor of the enzyme that catalyzes the first step of sphingolipid biosynthesis, serine palmitoyltransferase (10). With myriocin incubation, we observed no change in the hypertrophic response with PMA treatment. For this reason, we will be presenting only on the impact that silencing *CERS2* and *CERS5/6* had on the hypertrophic response induced by PMA treatment.

3.3.2 Confirming a hypertrophic response

To increase rigor in our hypertrophy model, we used three methods to ensure the HCMs developed a hypertrophic phenotype following 48h PMA treatment. HCMs were treated with PMA, or a respective vehicle control, fixed, stained, and imaged to analyze changes in cell size

(**Figure 3.1A**). PMA treatment increased the average cell size by approximately 33% (**Figure 3.1B**). Additionally, PMA treatment increased both BNP protein expression (**Figure 3.1C**) and mRNA (**Figure 3.1D**). Taken together, this experimental evidence supports that PMA treatment induces a consistent cardiac hypertrophy response in our HCM model.

3.3.3 RNA sequencing sample overview

Our two experimental groups comprise silencing of the ceramide synthases responsible for the generation of the proposed protective VLC ceramides (*CERS2*), and detrimental LC 16:0 ceramide (*CERS5/6*). Using methods optimized and discussed in **Chapter 2**, we have demonstrated that knockdown of *CERS2* and *CERS5/6* both result in the reduction of the expected ceramides and downstream sphingolipids. Furthermore, we have demonstrated that with *CERS* KD alone, we observe many pathway changes and interestingly, the trends with these pathway changes are primarily discordant with one another, suggesting that LC and VLC ceramides play contrasting roles in HCM homeostasis. To continue exploring the hypothesis that altering LC and VLC sphingolipid species in HCMs will influence CVD progression we silenced the respective *CERS* enzymes, then induced cardiac hypertrophy with PMA. This resulted in four different experimental conditions (n=3) for each *CERS* KD that were subjected to global mRNA sequencing: (1) KD treated with PMA, (2) KD treated with vehicle, (3) scramble control treated with PMA, (4) scramble control treated with vehicle. In **Chapter 2**, we presented data for the KD and scramble controls treated with vehicle, but in this chapter, we will analyze all four experimental conditions. A PCA plot displays separation between the different conditions with *CERS2* KD (**Figure 3.2A**) and *CERS5/6* KD (**Figure 3.2B**), suggesting that both KD and PMA treatments alone lead to significant alterations in the transcriptome.

3.3.4 Hypertrophy response pathway changes

Treatment with PMA for 48h leads to many HF relevant pathway changes in HCMs. Since both experimental groups had controls treated with PMA and the respective vehicle, it is crucial to compare the PMA response of the controls to ensure we are observing comparable results from day-to-day experiments. A DESeq2 analysis was completed on both datasets to generate the DEGs and rank all the genes in terms of significance. This preranked DESeq2 file was analyzed through GSEA to identify transcriptome perturbations that map onto biologically relevant pathways due to PMA treatment. With a preset FDR < 0.05, we observed over 60% DEG and specific pathway overlap, demonstrating that these analyses are very similar, as small variations in biological replicates are to be expected. Because of this, we chose a single dataset to demonstrate the DEG and pathway changes observed due to PMA addition in HCMs, focusing solely on pathway alterations observed in both datasets (**Figure 3.3**). With PMA treatment, we observed an upregulation in ECM organization, the interferon response, hypoxia, sphingolipid and metal metabolism, and steroid biosynthesis. Additionally, we observed an upregulation in cardiomyopathy pathways, suggesting that the changes observed due to PMA treatment render similar changes to those observed in HF. Furthermore, we saw downregulations in translation, apoptosis, energy metabolism, rho GTPase, and the cell cycle.

3.3.5 Hypertrophic response changes due to ceramide synthase 2 (*CERS2*) knockdown

Reducing the expression of *CERS2* altered the PMA induced hypertrophic response. In order to tease out the hypertrophic response changes due to *CERS* KD, we had to control for both gene silencing and PMA treatment effects. To achieve this, we ran an interaction analysis known as an LRT, which identified 560 genes that were significantly altered with an FDR < 0.05

(**Figure 3.4**). These 560 genes represent the changes observed in the hypertrophic response due to *CERS2* KD, a few of which have been highlighted to indicate their changes with respect to *CERS2* KD and PMA treatment. Importantly, none of the *CERS* were identified, validating that with the KD and PMA treatment, *CERS* expression stayed consistent.

We then performed k-means clustering on the 560 genes identified by the DESeq2 LRT analysis. We found that the gene expression patterns across the four experimental conditions were well-differentiated by 7 clusters as shown for all the genes in **Figure 3.4** and the cluster expression means in **Figure 3.5A**. While k-means is an unsupervised method, we attempted to add some biological interpretation to the clusters. Each gene cluster underwent a WebGestalt analysis to assign biologically relevant functional categories to the observed expression change patterns. This analysis allowed us to compare physiological responses to cluster expression patterns to provide a more thorough understanding of the biological processes altered in response to hypertrophy induction due to *CERS2* KD. Initially, all 560 identified genes were subjected to a WebGestalt over-representation analysis, which is a popular tool that assists in turning gene lists into biologically relevant functional categories (8). Then, the gene lists comprising each cluster were subjected to this same analysis, and any identified overlapping functions were labeled according to the respective cluster (**Figure 3.5B**). The gene list encompassed in cluster 7 did not map onto any biologically relevant pathways. This is not concerning and indicates that the list of genes that made up this cluster did not strongly correlate with any biological processes, hence is unlabeled in the volcano plot. Interestingly, we observed hypertrophic response changes in cholesterol and lipid metabolism, the immune response, and ECM organization due to *CERS2* KD. We will address the particular patterns observed in the discussion section, but alterations in

these pathways suggests that silencing *CERS2* leads to alterations in important processes relevant to CVD pathophysiology.

3.3.6 Hypertrophic response alterations due to ceramide synthase 5 and 6 (*CERS5/6*) knockdown

Similar to the *CERS2* KD interaction analysis, we completed a *CERS5/6* KD interaction analysis to identify the hypertrophic response changes due to genetic manipulation of *CERS5/6*. Controlling for both *CERS5/6* KD and PMA treatments alone identified 405 genes (FDR < 0.05) as being different in the hypertrophic response due to *CERS5/6* KD (**Figure 3.6**). Notably, none of the *CERS* were identified within these 405 genes of interest, again verifying that with KD and PMA treatment *CERS* expression stayed consistent. *LDLR* (low density lipoprotein receptor), *ACTA2* (actin alpha 2), *PLIN2* (perilipin 2), and *ANKRD1* (ankyrin repeat domain 1) constitute a few of these observed gene changes.

A cluster analysis was completed on these identified genes and their cluster expression patterns can be found in **Figure 3.7A**. These gene sets were assigned biologically relevant functions using WebGestalt and are mapped onto all the observed changes (FDR < 0.05) with the identified LRT genes (**Figure 3.7B**). Notably the gene sets that make up clusters 7 and 8 did not map onto any biological processes, so they are excluded from the volcano plot. Similar to what was found with *CERS2* KD, we observed hypertrophic response changes in cholesterol biosynthesis, the immune system, and ECM organization due to *CERS5/6* KD. These results suggest that *CERS5/6* KD also perturbs pathways important to the hypertrophic response and could further impact CVD progression.

3.4 Discussion

3.4.1 Summary of results

In this study, we investigated the effect of silencing ceramide synthases responsible for the production of VLC 22:0 and 24:0 ceramides (*CERS2*) and LC 16:0 ceramide (*CERS5/6*), on the hypertrophic response in human cardiomyocytes. In **Chapter 2**, we successfully demonstrated that knocking down *CERS2* and *CERS5/6* in HCMs reduced the cellular level of their respective ceramides and downstream complex sphingolipids as expected. Additionally, we were able to demonstrate that *CERS2* and *CERS5/6* KD had contrasting effects on various transcriptomic pathways, which is further evidence that VLC and LC sphingolipids play different roles in cardiovascular homeostasis. In this study, we expanded on our previous work by exploring how altering these ceramide synthases could impact pathways crucial for cardiovascular disease progression by utilizing a cardiac hypertrophy model. The key finding in this study is that the VLC and LC ceramides play opposite roles in important pathways linked to the cell's response to hypertrophy which mimics the progression of HF. *CERS2* KD leads to pathway changes that support a more advanced HF progression while *CERS5/6* KD leads to less aggressive changes in pathways crucial to cardiac hypertrophy progression. These findings support our hypothesis that products of *CERS2* may be protective against cardiac hypertrophy, while products of *CERS5/6* may worsen CVD progression.

3.4.2 PMA treatment leads to a cardiac hypertrophy phenotype

In order to test how the different *CERS* impact the progression of heart disease, we initially had to develop a CVD model in HCMs. We chose to target cardiac hypertrophy since hypertrophy typically precedes more advanced stages of HF and is a disease that can be mimicked in cell culture. We used the PKC activator, PMA (11), as our hypertrophy inducer.

PKC plays a multifaceted role in many different CVDs, including cardiac hypertrophy, where it regulates apoptosis, endothelial function, cardiac ion channels, mitochondrial function, and the inflammatory response (12). Furthermore, in 2012 Russo et al. demonstrated that *CERS5* KD was sufficient to prevent myristate induced hypertrophy in feline cardiomyocytes (13), supporting that PMA induced hypertrophy would be a relevant model for studying how different ceramide species contribute to the hypertrophic response. We were able to confirm the characteristic increase in HCM size with PMA treatment (**Figure 3.1A**), as well as demonstrate an increase in both mRNA (**Figure 3.1D**) and protein expression (**Figure 3.1C**) of BNP, the clinical HF biomarker.

PMA treatment alters crucial pathways consistent with cardiac hypertrophy (**Figure 3.3**). When benchmarking DEG and pathways changes within the two different transcriptomic batches of PMA treatment vs controls, we noted minimal day-to-day variability. With both datasets, we observed marked increases in pathways involved in ECM organization and hypoxia, suggesting the PMA treated HCMs are undergoing cardiac remodeling, a signature of cardiac hypertrophy (14,15). Additionally, we noted increases in sphingolipid and metal metabolism as well as steroid biosynthesis. All these changes are characteristic of CVD pathophysiology, which is further validated by the observation of increases in pathways like cardiomyopathy, suggesting that similar gene changes are observed in our PMA treated HCMs as those observed in human heart disease. Observed declines in pathways involved in energy metabolism like oxidative phosphorylation (OXPHOS) and the tricarboxylic acid (TCA) cycle, suggest the PMA treated HCMs may be struggling to reach the energy requirements essential for healthy HCMs, and further supports a hypertrophic phenotype. Additionally, adult HCMs typically do not reenter the cell cycle when exposed to growth signals, and instead respond to these signaling by increasing

cardiac mass through hypertrophy (16). The observed decline in pathways involved in the cell cycle and translation may suggest that the HCMs are struggling to maintain homeostasis compared to their untreated controls. Ultimately, it is important to remember that cardiovascular diseases are complex, and pathophysiology changes based on the afflicted CVD indication. That said, all the observed dysregulations following PMA treatment are indicative of stressed and unhealthy HCMs. The observed pathway changes suggest that PMA treatment is changing the transcriptome in our cultured HCMs in a similar manner to what is observed in human cardiac hypertrophy, validating the use of this model to study HF disease progression.

3.4.3 Hypertrophy response changes due to *CERS* KD

There were a handful of changes in the hypertrophic response due to both *CERS* KDs. To tease out hypertrophy response changes due to *CERS* KD, we ran an LRT analysis to control for isolated changes due to both *CERS* KD and PMA treatment. Notably, although this analysis is limited to a small number of genes within each pathway, it directed us to the most important changes in the hypertrophic response due to *CERS* KD. With the silencing of *CERS2* and *CERS5/6*, we identified 560 and 405 genes altered, respectively, that represent the hypertrophy response changes due to reduced *CERS* expression. The genes were clustered using k-means to minimize the sum-of-squares differences among the clusters, but without respect to the underlying biology. The gene sets that composed each cluster were subjected to WebGestalt analyses to assign biologically relevant functional categories to each cluster expression pattern.

3.4.3.A The effect of *CERS2* KD on the hypertrophic response

Before breaking down these patterns and biological functions to better understand what is occurring within the HCMs, we must first reiterate the findings that were made in **Chapter 2**. Looking at just *CERS2* KD alone, we observed changes in many pathways crucial for cardiac

hypertrophy, leading us to believe that *CERS2* KD and the corresponding reduction of cellular levels of VLC sphingolipids, by itself, can influence a HF phenotype within these cells. That said, with *CERS2* KD and PMA treatment, these cells are being stressed twice; both with treatments that we have evidence to believe increase hypertrophy. We would also like to reemphasize that all 560 genes identified in the interaction analysis are changed due to the hypertrophic response because *CERS2* was silenced.

The hypertrophy response with *CERS2* KD differs by observed increases in lipid metabolism and cardiomyocyte remodeling and decreases in the immune response (**Figure 3.5B**). Cluster 1 represents cholesterol and lipid metabolism. As discussed in **Chapter 2**, *CERS2* KD alone results in decreases in pathways involved in cholesterol biosynthesis and lipid metabolism compared to control cells. With this gene list, we see a marked increase in gene expression related to cholesterol biosynthesis and lipid metabolism with *CERS2* KD and PMA treatment, but this pattern is not observed in the scramble control, suggesting that with *CERS2* KD and PMA treatment, the cells are undergoing further lipid dysregulation. Additionally, we observe an increase in ECM organization, denoted by a higher gene expression profile with PMA treatment and *CERS2* KD in cluster 3, indicating increased cardiac remodeling and hypertrophy (15). The immune response is also greatly influenced by *CERS2* KD and PMA treatment. Examining cluster 2 closer, we observe lower gene expression changes with PMA treatment in the *CERS2* KD samples, compared to the controls, leading us to conclude that there is less of an immune response due to *CERS2* KD following PMA treatment. Overall, the hypertrophy response changes due to *CERS2* KD are very suggestive of increased cardiac dysfunction, but these findings need to be further explored experimentally.

3.4.3.B The effect of *CERS5/6* KD on the hypertrophic response

Contrasting the *CERS2* KD, in **Chapter 2** we discussed how *CERS5/6* KD appeared to have less of a HF phenotype compared to controls, suggesting that *CERS5/6* and their gene products could play fundamental roles in the development and progression of HF. If *CERS5/6* KD is protective, and PMA treatment is detrimental, it is interesting to consider which hypertrophy responses are augmented due to a decline in 16:0 sphingolipid products. Again, it is important to point out that all 405 identified genes are altered due to both *CERS5/6* KD and PMA treatment.

The hypertrophic response with *CERS5/6* KD differs by observed increases in the immune response and decreases in cholesterol biosynthesis and cardiomyocyte remodeling (**Figure 3.7B**). Clusters 2 and 3 contain gene sets imperative to the cellular immune response. With both these clusters, we observe a larger change in gene expression following PMA treatment with *CERS5/6* KD compared to controls. Additionally, we observe a very significant decline in cholesterol biosynthesis, encompassed by the gene set linked to cluster 1. Finally, we note less expression following PMA treatment with *CERS5/6* KD samples compared to controls in cluster 4, which is representative of ECM organization and remodeling. Overall, the hypertrophy response changes due to *CERS5/6* KD are compelling in that the hypertrophy treatment appeared to be less severe in samples with *CERS5/6* KD compared to controls, but these findings need to be explored further experimentally.

Although it appears that *CERS5/6* KD leads to protection against the severity of PMA treatment, I will reiterate some of the points made in **Chapter 2**. Due to the vast amount of changes observed due to *CERS5/6* KD alone, caution should exercised if developing inhibitors targeting these ceramide synthases. It is possible that inhibition of any single *CERS* could result

in increased toxicity and cell death based on the role the ceramides play in regulated cell death like apoptosis. For this reason, I believe a better therapeutic approach would be to increase the concentration of VLC ceramide species by developing a compound that either induces or activates *CERS2*. This work is important as it presents a first look at the role specific ceramide synthases play in the development of cardiac hypertrophy. Understanding the physiology of the different ceramide species is crucial as more efforts go into developing therapeutic agents targeting modifiable pathways in the sphingolipid metabolic scheme.

3.5 Conclusions

In conclusion, we see contrasting changes in the *CERS2* and *CERS5/6* hypertrophic responses. When HCMs experienced silenced *CERS2* expression and reduced VLC ceramide cellular content and were then subjected to hypertrophy, we observed increases in HCM remodeling, cholesterol biosynthesis, and lipid metabolism, and decreases in the immune response, indicative of more advanced CVD progression. While, following *CERS5/6* KD, HCMs that had reduced 16:0 ceramide and the corresponding sphingolipid products underwent pathway changes suggesting an increase in the immune response and a decline in HCM remodeling, cholesterol biosynthesis, and lipid metabolism, reflective of a reduced hypertrophic response following PMA treatment and potentially healthier cells. These findings support our hypothesis that *CERS2* and VLC ceramides may play a protective role against CVD progression, while *CERS5/6* and 16:0 ceramide could have a harmful effect and contribute to the development and progression of CVD. These findings emphasize the importance of research that will characterize the role that VLC and LC sphingolipid species play in both the development and progression of cardiovascular disease.

Figures

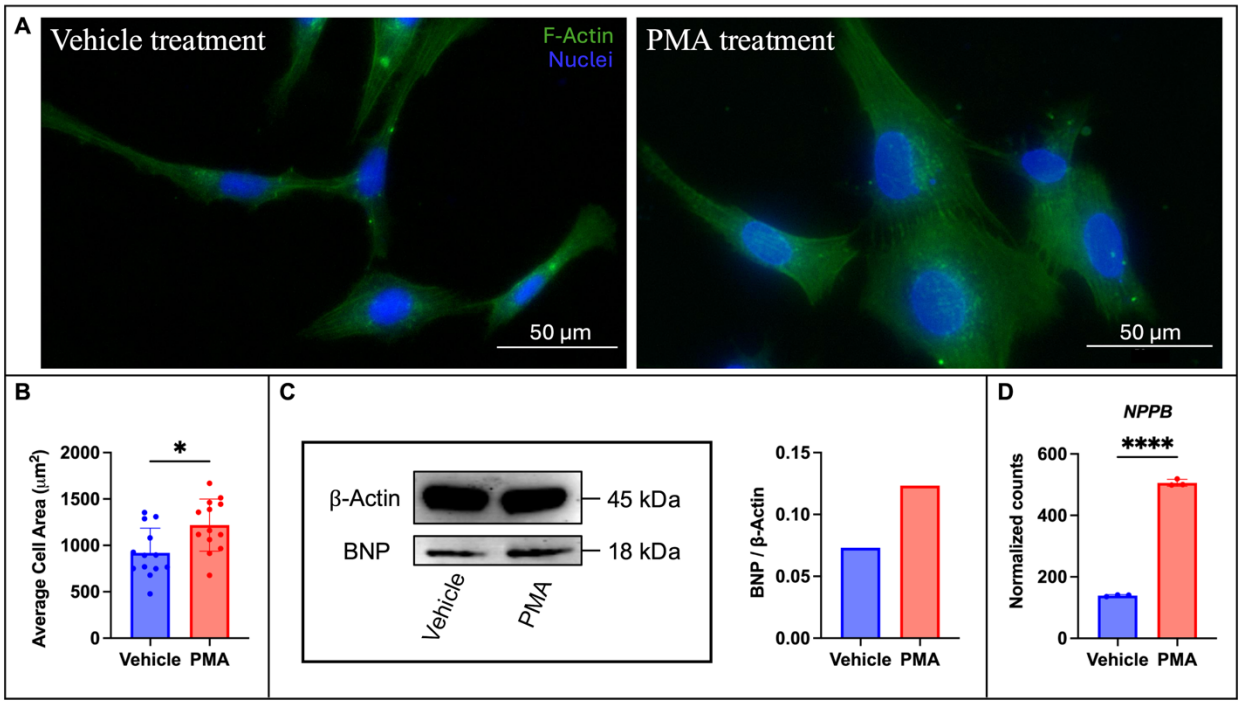

Figure 3.1. PMA treatment for 48h induces a hypertrophic response in HCMs.

(**A**) An increase in HCM cell size is observed with 40x images and F-actin staining and the (**B**) average cell area from 13 individual images depicts a roughly 33% increase in HCM size. (**C**) A western blot and the respective band intensity quantification showing increased BNP protein expression (n=6, technical replicates) and (**D**) *NPPB* (gene encoding for BNP) normalized gene expression (from RNA-sequencing results) increases following PMA treatment, n=3. **** $P < 0.0001$, * $P < 0.05$

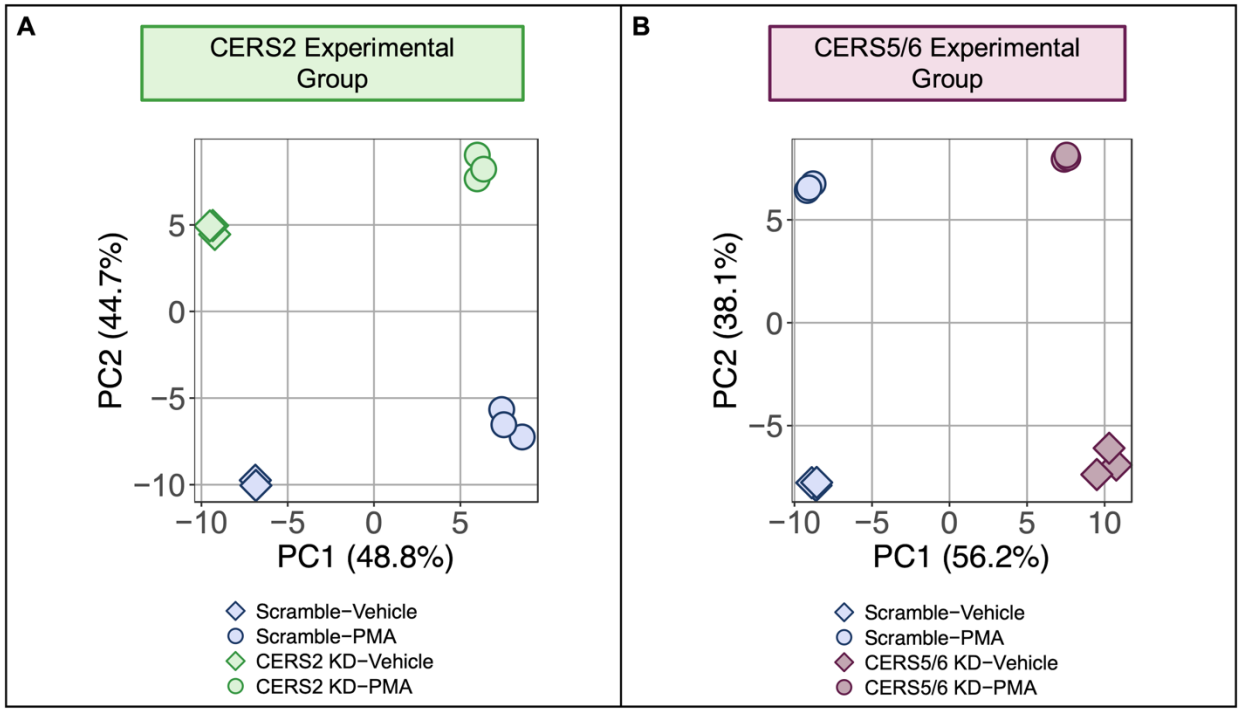

Figure 3.2. Transcriptome variation between the different *CERS* experimental groups treated with PMA vs controls.

PCA plot across the cardiomyocyte transcriptome with the samples from the (**A**) *CERS2* KD and (**B**) *CERS5/6* KD demonstrates clear separation between all the different sample conditions within each experimental group.

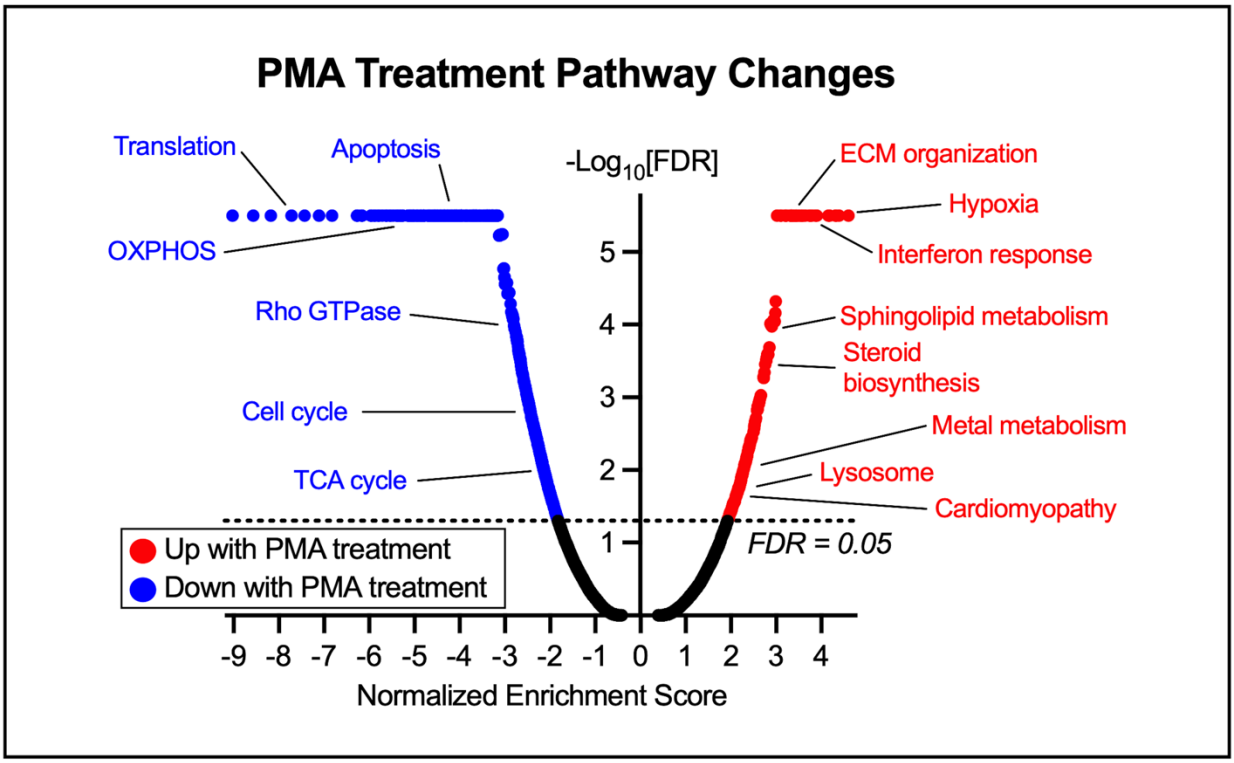

Figure 3.3. Volcano plot displaying pathway changes due to 48h PMA treatment.

The highlighted pathways are representative of the major changes in HCMs observed in scramble controls treated with PMA compared to treated with vehicle controls. OXPHOS – oxidative phosphorylation, TCA – tricarboxylic acid.

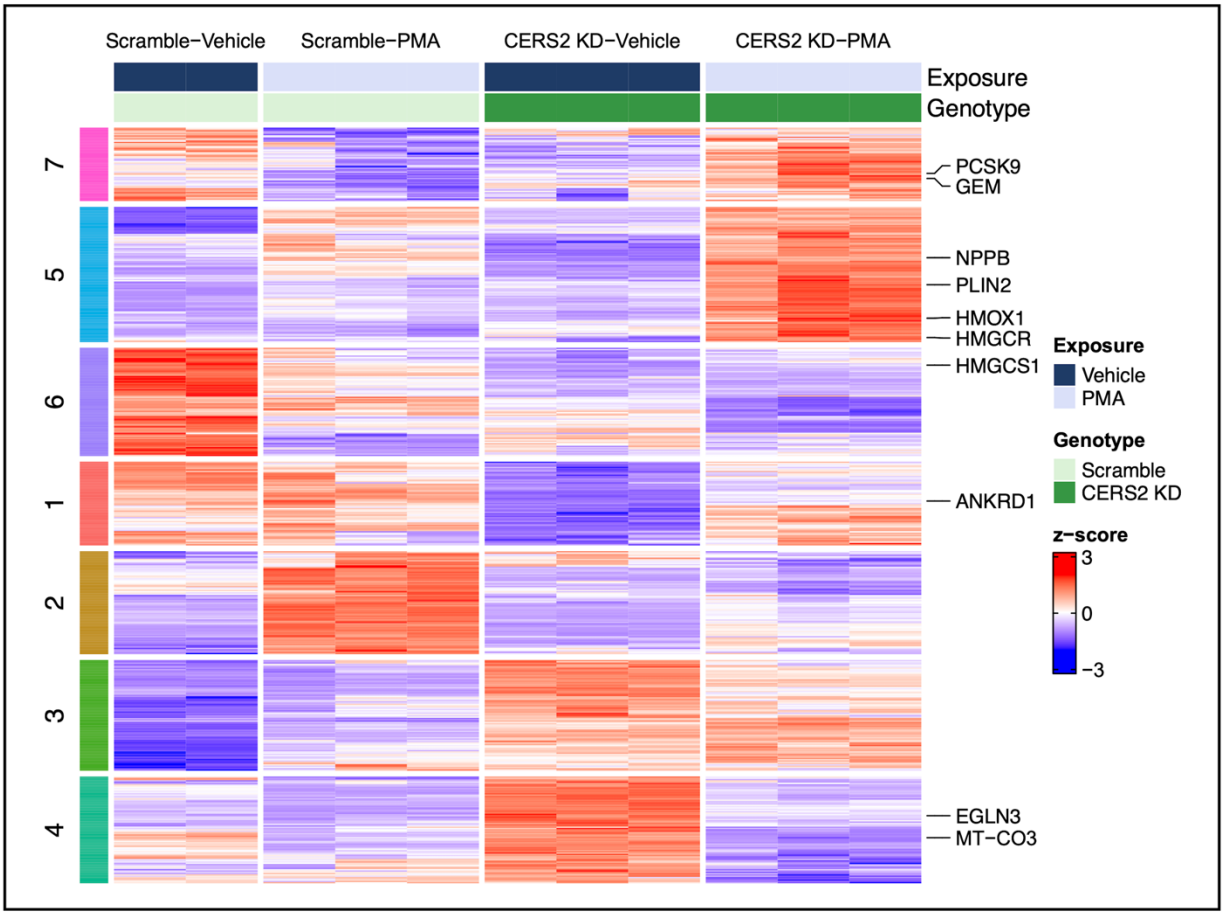

Figure 3.4. DEG heat map highlighting gene changes in the hypertrophic response due to *CERS2* KD.

The color coding and numbers on the left map onto the specific gene clusters presented in **Figure 3.5** below.

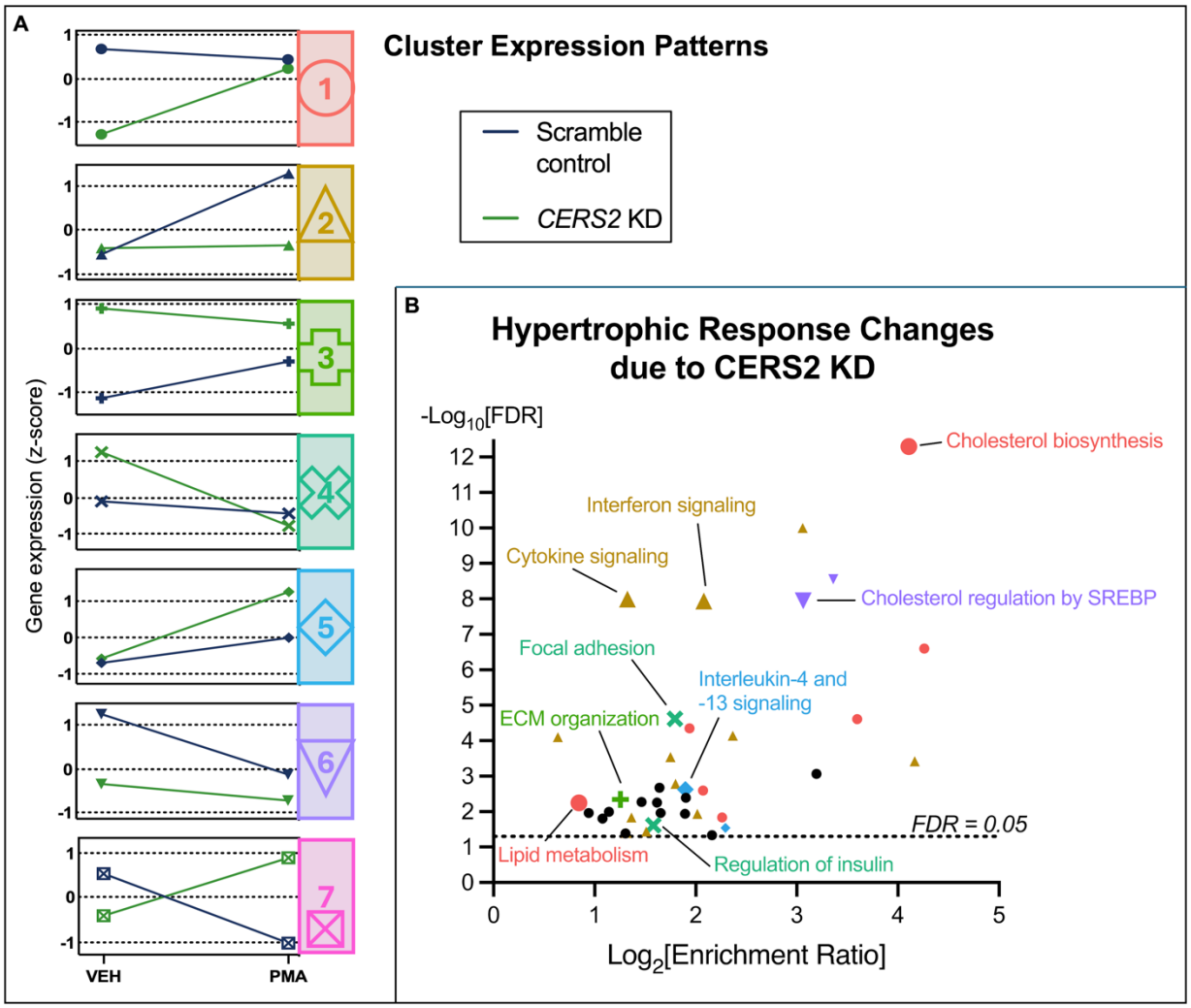

Figure 3.5. Biological functions assigned to each gene cluster identified as being significantly different in the *CERS2* KD hypertrophy response.

(A) Identified cluster expression patterns for all the gene changes due to PMA treatment and *CERS2* KD. **(B)** WebGestalt analysis using all 560 genes identified as different in the hypertrophic response due to *CERS2* KD. Representative biological functions were assigned to each cluster, with the symbol and color coordinating to the respective cluster (FDR < 0.05). Unlabeled points did not correspond to any individual cluster. ECM – extracellular matrix, SREBP – sterol regulatory element-binding proteins

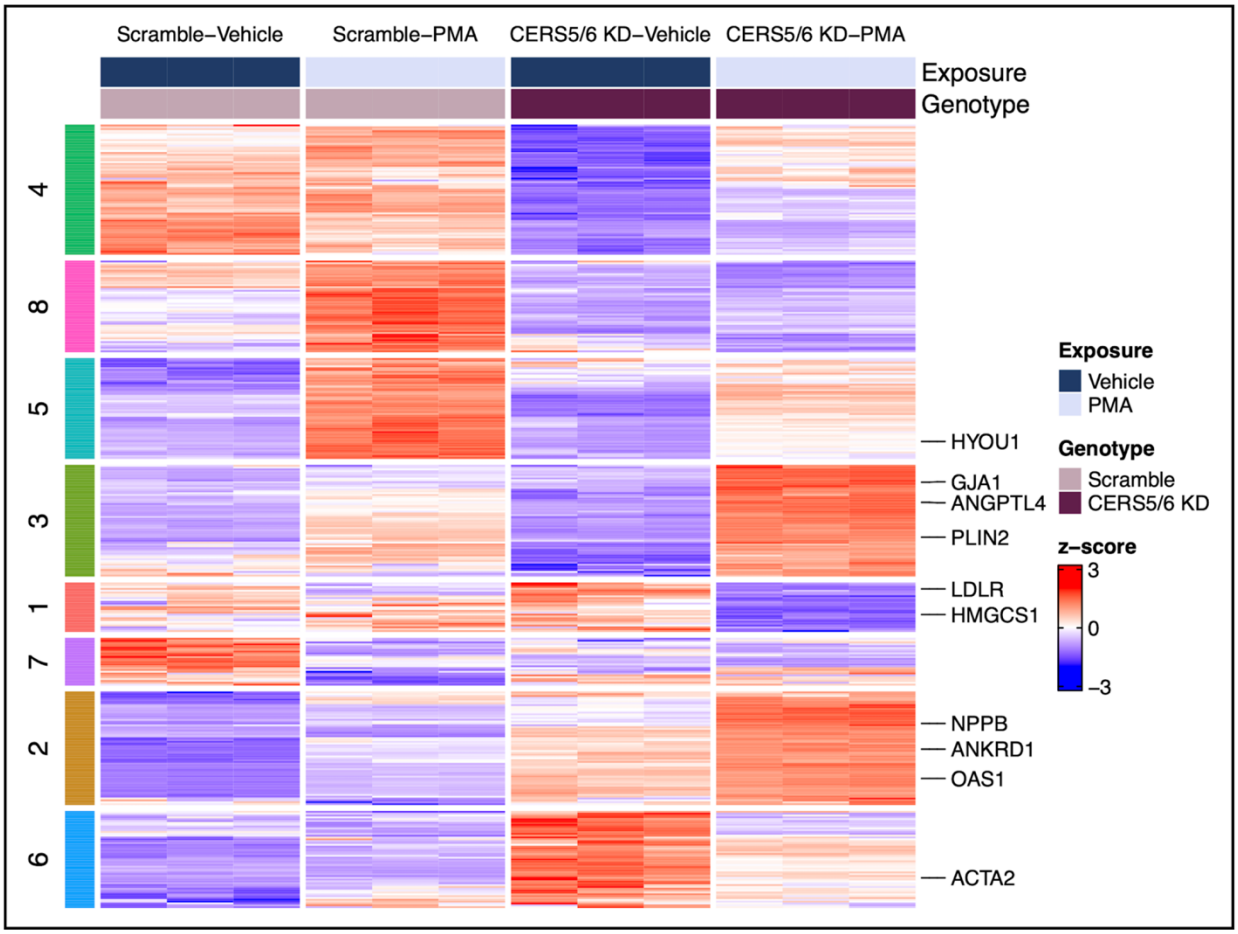

Figure 3.6. DEG heat map highlighting identified gene changes in the hypertrophic response due to *CERS5/6* KD.

The breakup of the genes on the left-hand side corresponds to each respective gene cluster presented in **Figure 3.7**.

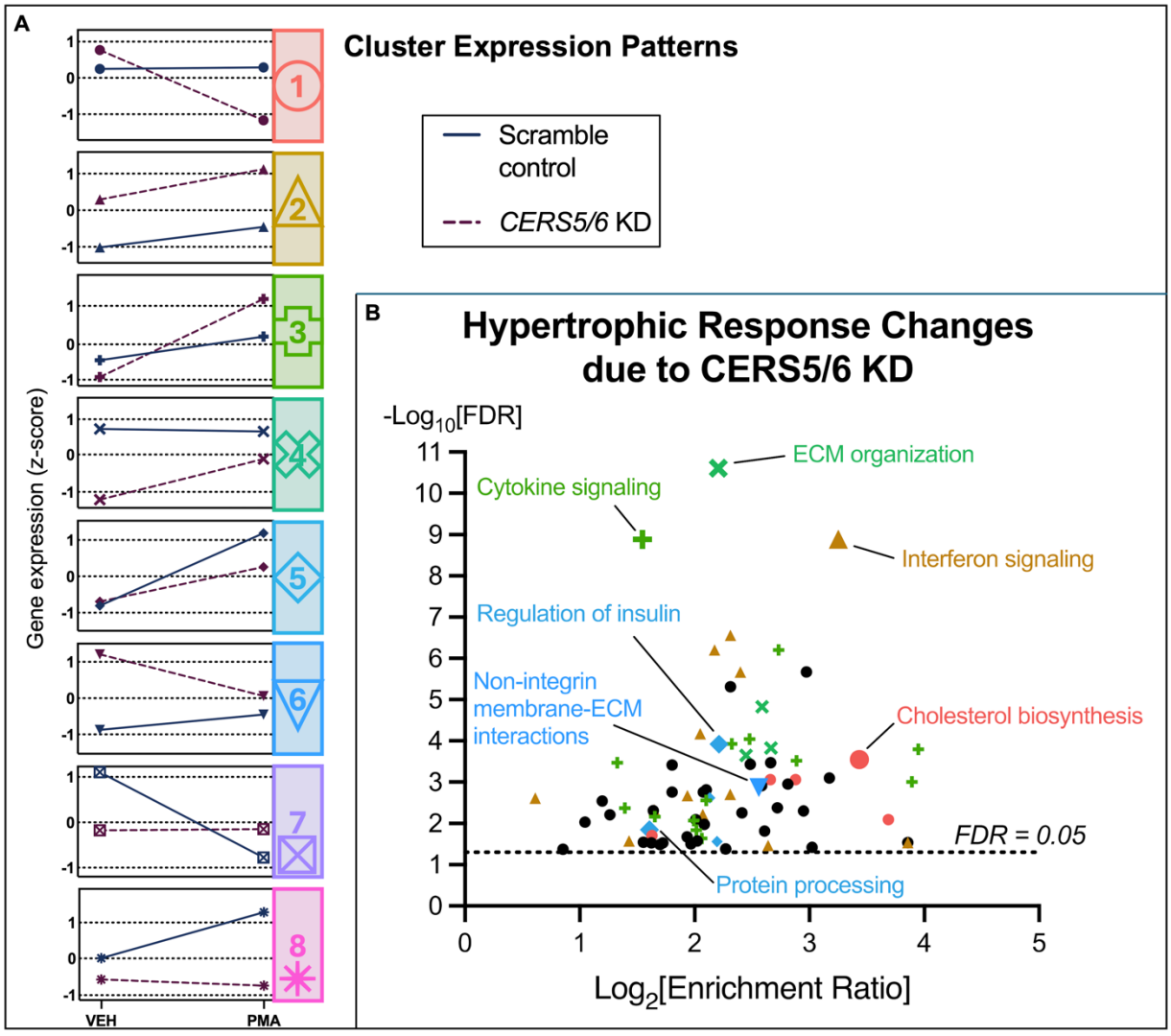

Figure 3.7. Biological functions assigned to each gene cluster identified as being significantly different in the *CERS5/6* KD hypertrophy response.

(A) Identified cluster expression patterns for all the gene changes due to both *CERS5/6* KD and PMA treatment. (**B**) WebGestalt analysis using all 405 genes identified as different (FDR < 0.05) in the hypertrophic response due to *CERS5/6* KD. Unlabeled points did not correspond to an individual cluster. ECM – extracellular matrix

References

1. Grösch S, Schiffmann S, Geisslinger G. Chain length-specific properties of ceramides. Prog Lipid Res. 2012 Jan;51(1):50–62.

2. Pettus BJ, Chalfant CE, Hannun YA. Ceramide in apoptosis: an overview and current perspectives. Biochim Biophys Acta BBA - Mol Cell Biol Lipids. 2002 Dec;1585(2–3):114–25.

3. Gulbins E, Li PL. Physiological and pathophysiological aspects of ceramide. Am J Physiol-Regul Integr Comp Physiol. 2006 Jan;290(1):R11–26.

4. Summers S. Ceramides in insulin resistance and lipotoxicity. Prog Lipid Res. 2006 Jan;45(1):42–72.

5. Hannun YA, Obeid LM. Principles of bioactive lipid signalling: lessons from sphingolipids. Nat Rev Mol Cell Biol. 2008 Feb;9(2):139–50.

6. Lemaitre RN, Jensen PN, Hoofnagle A, McKnight B, Fretts AM, King IB, et al. Plasma Ceramides and Sphingomyelins in Relation to Heart Failure Risk: The Cardiovascular Health Study. Circ Heart Fail. 2019 Jul;12(7):e005708.

7. Love MI, Huber W, Anders S. Moderated estimation of fold change and dispersion for RNA-seq data with DESeq2. Genome Biol. 2014 Dec;15(12):550.

8. Liao Y, Wang J, Jaehnig EJ, Shi Z, Zhang B. WebGestalt 2019: gene set analysis toolkit with revamped UIs and APIs. Nucleic Acids Res. 2019 Jul 2;47(W1):W199–205.

9. Tham YK, Bernardo BC, Ooi JYY, Weeks KL, McMullen JR. Pathophysiology of cardiac hypertrophy and heart failure: signaling pathways and novel therapeutic targets. Arch Toxicol. 2015 Sep;89(9):1401–38.

10. Miyake Y, Kozutsumi Y, Nakamura S, Fujita T, Kawasaki T. Serine Palmitoyltransferase Is the Primary Target of a Sphingosine-like Immunosuppressant, ISP-1/Myriocin. Biochem Biophys Res Commun. 1995 Jun;211(2):396–403.

11. Vega RB, Harrison BC, Meadows E, Roberts CR, Papst PJ, Olson EN, et al. Protein Kinases C and D Mediate Agonist-Dependent Cardiac Hypertrophy through Nuclear Export of Histone Deacetylase 5. Mol Cell Biol. 2004 Oct 1;24(19):8374–85.

12. Miao L na, Pan D, Shi J, Du J peng, Chen P fei, Gao J, et al. Role and Mechanism of PKC-δ for Cardiovascular Disease: Current Status and Perspective. Front Cardiovasc Med. 2022 Feb 15;9:816369.

13. Russo SB, Baicu CF, Van Laer A, Geng T, Kasiganesan H, Zile MR, et al. Ceramide synthase 5 mediates lipid-induced autophagy and hypertrophy in cardiomyocytes. J Clin Invest. 2012 Nov 1;122(11):3919–30.

14. Dai Z, Cheng J, Liu B, Yi D, Feng A, Wang T, et al. Loss of Endothelial Hypoxia Inducible Factor-Prolyl Hydroxylase 2 Induces Cardiac Hypertrophy and Fibrosis. J Am Heart Assoc. 2021 Nov 16;10(22):e022077.

15. Kehat I, Molkentin JD. Molecular Pathways Underlying Cardiac Remodeling During Pathophysiological Stimulation. Circulation. 2010 Dec 21;122(25):2727–35.

16. Ahuja P, Sdek P, MacLellan WR. Cardiac Myocyte Cell Cycle Control in Development, Disease, and Regeneration. Physiol Rev. 2007 Apr;87(2):521–44.

Chapter 4: The Role of the Inotropic Agent Apelin and its Receptor in Cardiac Hypertrophy

4.1 Introduction

Apelin and APJ constitute two major members of the AS. Apelin isoforms are peptides that have multiple bioactive forms in the body that activate APJ signaling to regulate important cardiovascular functions. All apelin isoforms have some levels of activity, from the 77 residue preproapelin (AP-77) to the 13 residue apelin (AP-13) (1,2). The most studied and considered to be the most active apelin isoforms (in inverse order) are AP-36, AP-17, AP-13, and the post-translationally modified pyr-AP-13, but there are apelin isoforms beyond these (1,2).

Interactions within APJ with the different apelin isoforms lead to different phosphorylation patterns on APJ which selectively influence distinct signaling pathways and downstream cellular effects (2–4). A more in-depth description of APJ signaling can be found in **Chapter 1, Section 1.4.2**. In 2018, Shin et al. summarized a group of APJ mutation studies suggesting that there are specific amino acid residues within APJ that lead to certain downstream signaling responses (1). An example of this was demonstrated by Iturrioz et al. where site-directed mutagenesis of the tryptophan in APJ's CWXP motif were still capable of apelin binding and $G\alpha_i$ signaling, but were unable to induce receptor internalization with AP-17, despite AP-17 binding (5). Additionally, Jiang et al. conducted a thorough investigation to determine how the different apelin isoforms impact APJ's signaling pathways, concluding that all the ligands exhibit distinct signaling profiles (4). The crystal structure of APJ bound to AP-17 mimetic peptide AMG3054, suggests that ligand-APJ interactions may involve a two-site binding mode (6). Based off of the mutagenesis work this group completed, they further hypothesized that apelin isoforms of different lengths may interact with APJ in a different manner, with AP-36 reaching

deeper into APJ's binding pocket while the shorter apelin isoforms may rely more on electrostatics and surface level grooves within the APJ structure (6). This theory could help further explain the longer lasting effects of AP-36 compared to AP-13 (6). As there are many physiological functions that can be activated following stimulation of APJ with the different apelin peptides, it is important to differentiate between the effects of the different apelin species on heart disease. To our knowledge, no study has been conducted exploring the different roles the apelin isoforms play on cardiac health and in response to cardiac hypertrophy. If the mechanisms through which the different apelin isoforms exhibit distinct functions were better understood, it could be beneficial to try and mimic those interactions with future cardiovascular therapies.

In this chapter for the first time, we will treat adult human cardiomyocytes with different forms of apelin and determine their effect on overall cell survival. We will then perform an unbiased transcriptomic analysis to measure global gene changes due to apelin treatment. Additionally, we explore how the human cardiomyocyte hypertrophy response is modulated following treatment with two apelin isoforms both with and without the overexpression of APJ. We selected pyr-AP-13, as it is the most studied apelin isoform and is currently thought to be the most important in maintaining cardiac function (7,8). We also explored the consequences of adding exogenous AP-17, since this apelin isoform has the greatest deviation in signaling effects compared to pyr-AP-13 (4). We hypothesized that pyr-AP-13 and AP-17 would activate separate downstream pathways leading to different mechanisms of protection against PMA treatment.

4.1.1 Research Strategy

We begin this project by completing work in HEK293T cells, as these cells are widely used to characterize GPCRs (9). We report on the construction of a plasmid that results in the

overexpression of APJ. We further characterize this plasmid by looking at APJ half-life and activity in HEK293T cells, before switching to experimentation in an immortalized adult human ventricular cardiomyocyte cell line. Since APJ is not endogenously expressed at high enough levels in our HCMs, or any other cardiac cell line we investigated, our only option was to overexpress the receptor. This is still a physiologically relevant occurrence, as we observed a significant increase in *APLNR* (gene for APJ) expression in cardiac tissue from patients diagnosed with cardiomyopathy compared to subjects free of cardiovascular disease diagnoses (**Figure 4.1**). Initially, validation had to be repeated in HCMs to ensure transfection with the APJ plasmid resulted in overexpression of APJ mRNA and protein. We then explored the cellular consequences of exogenous apelin treatment as well as APJ overexpression on the overall homeostasis of the HCM. We conclude this chapter by analyzing the hypertrophic transcriptional response due to the addition of a single or multiple AS components following PMA treatment.

4.2 Materials and Methods

4.2.1 Materials

HEK293T cells, DMEM media, and Penicillin-Streptomycin solution were purchased through ATCC (Manassas, VA). Immortalized human ventricular cardiomyocytes and all their corresponding materials: PriGrow I medium, Penicillin/Streptomycin solution, and extracellular matrix were purchased through Applied Biological Materials (Bellingham, WA). The APJ plasmid was purchased from Origene (Rockville, MD). pSNAP vector and SNAP substrate BG-782 were obtained through New England Biolabs (Ipswich, MA). The SNAP-APJ cDNA construct was created using Takara's (San Jose, CA) In-Fusion Molecular Cloning Kit and Stellar competent cells and purified using the HiSpeed Plasmid Maxi Kit purchased from QIAGEN (Germantown, MD). The sequences were validated through Eurofins Genomics (Seattle, WA).

Apelin-13, pyrogluamyl-apelin-13, cycloheximide, forskolin, Ro 20-1724, IBMX, and phorbol 12-myristate 13-acetate were obtained through Cayman Chemical (Ann Arbor, MI). Apelin-17 was purchased from Abcam (Boston, MA). The pMAPK and GAPDH antibodies were obtained through Cell Signaling (Danvers, MA) and the APJ antibody was purchased from Proteintech (Rosemont, IL). The secondary antibody was obtained from LI-COR (Lincoln, NE). Tissue culture treated plates, Lipofectamine 3000 Reagent, DMSO, Opti-MEM media, PBS, protamine sulfate, RIPA lysis buffer, Halt protease and phosphatase inhibitor cocktail, simply-safe stain, BCA protein assay materials and bovine serum albumin standards, dithiothreitol, electrophoresis system, PageRuler Plus Prestained Protein Ladder, NuPAGE 4-12% Bis-Tris gels, MOPS SDS Running Buffer, iBlot Transfer System, nitrocellulose transfer stacks, PrestoBlue Viability Reagent, RNA isolation Kits, and High-Capacity RNA-to-cDNA kits were all purchased from Thermo Fisher Scientific (Waltham, MA). Additionally, all RT-qPCR materials were obtained from Thermo Fisher Scientific's TaqMan Reagents: TaqMan Fast Advanced Master Mix for qPCR and TaqMan human primers: GUSB (Assay ID: Hs00939627_m1), APLNR (Assay ID: Hs00270873_s1), APLN (Assay ID: Hs00175572_m1), and NPPB (Assay ID: Hs00173590_m1). The cAMP assay was obtained from Promega (Madison, WI). Novogene (Sacramento, CA) completed the RNA sequencing.

4.2.2 Cell culture

HEK293T cells (#CRL-3216) were purchased through ATCC (Manassas, VA) and maintained in Dulbecco's Modified Eagle's Medium (DMEM) supplemented with 10% FBS and 0.1% Penicillin-Streptomycin Solution. Cells were cultured in a 37°C humidified incubator with 5% CO_2. BioLite Microwell Plates (#130184) were purchased from Thermo Fisher Scientific (Waltham, MA) and used for all cell experiments.

Immortalized human ventricular cardiomyocytes were maintained as described in **Chapter 2, Section 2.2.2**.

4.2.3 SNAP-APJ plasmid construction and purification

The open reading frame (ORF) of the purchased APJ plasmid (#RC207576) was excised and subcloned into New England Biolab's pSNAPf vector (#N9183) utilizing Takara Bio's In-Fusion HD Cloning Kit (#639650) according to the manufacturer's protocol. The restriction enzymes XhoI and NotI were used to linearize pSNAPf, and the ORF of APJ was inserted, resulting in the SNAP-tag being located on the N-terminus of APJ. The SNAP-APJ plasmid and Empty-SNAP plasmids were transformed into Stellar competent cells (#636766) and purified using the HiSpeed Plasmid Maxi Kit (#12662) following the manufacturer's protocol. All sequences were validated through Eurofins Genomics (Seattle, WA).

4.2.4 Transient *APLNR* overexpression

Reverse transfection conditions were optimized using the Lipofectamine 3000 Transfection Reagent (#L3000001) for both cell lines used in this study – HEK293T and HCMs. The specific amounts of each reagent will be described in the following paragraph. In general, this procedure starts with two separate solutions being prepared: one containing lipofectamine 3000, and the other a mixture of DNA and P3000 reagent. These solutions were mixed well and combined in a 1:1 ratio to achieve a DNA-lipid complex that equilibrated at room temperature for 20 min while the cells were passaged and counted. The DNA-lipid complex (accounting for 10% of the total volume) was then mixed with complete media containing the respective number of cells and the corresponding mixture was added to each well.

The amounts and volumes of reagents below are provided for a single well of a 6-well plate. The total volume used for each well was 2.5 mL, and the transfection mixture added to each well equated to 10% of the total volume (250 µL). If a different plate was used, amounts were scaled down according to the well's total surface area.

HEK293T – For the lipofectamine mixture, 3.75 µL Lipofectamine 3000 was added to Opti-MEM media (#31985070) to bring the total volume to 125 µL for each well. For the DNA + P3000 mixture, 1.25 µg DNA + 2.5 µL P3000 Reagent were combined and the total volume was brought to 125 µL per well using Opti-MEM media. These two solutions were combined 1:1 and following a 20 min incubation at room temperature, 250 µL of this solution was added to each well with 9.0×10^5 cells in 2.25 mL complete media.

HCM – The lipofectamine mixture containing 1.5 µL Lipofectamine 3000 combined with Opti-MEM media was brought up to a total volume of 125 µL for each well. For the DNA + P3000 mixture, 2.5 µg DNA + 2 µL P3000 Reagent were combined and the total volume was adjusted to 125 µL per well with Opti-MEM media. Following the 1:1 mixture with these two solutions, 250 µL was added with 3.5×10^5 cells in 2.25 mL complete media to each well.

4.2.5 SNAP-APJ protein expression

Protein normalization, SDS-PAGE gels, and western blots were performed following the protocol described in **Chapter 3, Section 3.2.5** with the following modifications. For SNAP gels, samples were treated with SNAP substrate 782 (#S9142) for 30 min before being loaded onto an SDS-PAGE gel to identify SNAP-tagged proteins. SNAP gels were imaged at 700nm/800nm to measure SNAP-APJ protein expression and Coomassie stained (#LC6060) to quantify and

normalize each data point to the total amount of protein per lane. Following reduction with 50 mM dithiothreitol, the lysates of APJ and empty vector transfected cells were either boiled for 7 minutes or left to incubate at room temperature for 15 minutes. This brought to our attention that GPCR samples must be left at room temperature, because boiling a GPCR product led to excessive aggregation that prevented protein separation on the gel. Primary antibodies underwent the following dilutions: 1:1000 dilution of rabbit anti-APJ antibody (Proteintech, #20341-1-AP), 1:5000 dilution of rabbit anti-GAPDH antibody (Cell Signaling, #14C10), 1:333 dilution of rabbit anti-phospho-p44/42 MAPK (ERK1/2) (Thr202/Tyr204) antibody (Cell Signaling, #9101).

4.2.6 GPCR stability, functionality, and cell viability assays

GPCR stability was tested using a cycloheximide chase assay (10). Following the 24h transient transfection in HEK293T cells, the cells were treated with 50 µg/mL cycloheximide (#14126) for 0-6h and 24h. Cells were then collected, lysed, and incubated with the fluorescently tagged SNAP substrate 782, following the manufacturer's protocol, to identify any intact APJ protein. Data points were expressed as percent band intensity per total protein as measured by Coomassie staining utilizing biological triplicates. APJ half-life was determined using a nonlinear regression one-phase exponential decay curve.

The cAMP kit was purchased from Promega (#V1501). The HEK293T transfection was scaled down to utilize a 96-well white walled, clear bottom plate (#165306). For this experiment, cells underwent a 5-minute agonist/antagonist treatment with apelin and protamine sulfate before being subjected to a 15-minute forskolin treatment, after which the manufacturer's cAMP assay protocol was followed.

HCM viability was measured following the procedure described in **Chapter 2, Section 2.2.6**.

4.2.7 Induction of hypertrophy

Twenty-four hours after the SNAP-APJ or empty SNAP vector transfection, serum free media supplemented with apelin or controls replaced the existing media and a 2h pretreatment was initiated to prime APJ receptor recycling to the cell surface (11). After this, a 4 μM PMA treatment or a comparable vehicle control (0.025% DMSO) in serum free media was initiated, some supplemented with apelin treatment, and others left with just the PMA or vehicle treatment to serve as the no apelin control. The cells were then retreated 24h later with 2 μM PMA and their respective apelin or control supplementation, leading to a total 48h hypertrophy treatment with or without the apelins. The cells at this point were either utilized or harvested for further downstream analysis.

4.2.8 Total RNA isolation, RT-qPCR, and mRNA-sequencing

The total RNA isolation and RT-qPCR protocols were followed exactly as described in **Chapter 2, Section 2.2.5**. mRNA-sequencing was completed as described in **Chapter 2, Section 2.2.7**.

4.2.9 Bioinformatics and pathway analyses

4.2.9.A Gene expression analysis and gene set enrichment analysis

Gene expression analysis and GSEA protocols were run as described in **Chapter 2, Sections 2.2.8.A** and **2.2.8.B**, respectively. For this chapter, in addition of the use of the hallmark and canonical pathway molecular signature database categories, we also investigated the Gene Ontology collection of gene sets.

4.2.9.B WebGestalt

The WebGestalt analysis was completed as explained in **Chapter 3, Section 3.2.7.D** with one modification. These enrichment results were displayed using the weighted set cover, which finds the minimum subset of gene sets that can cover all the enriched gene sets and assign a corresponding P-value (12).

4.3 Results

4.3.1 Validation of stable and functional APJ overexpression

Initially, the commercially available Origene® Myc-DDK-tagged APJ plasmid (#RC207576) was used to overexpress APJ, but further analysis determined that introducing this plasmid into HEK293T cells resulted in inactive and nonfunctional APJ. Following this discovery, we instead created an APJ plasmid by inserting the APJ ORF into a pSNAPf vector, which resulted in a SNAP-tagged APJ (SNAP-APJ). After transient transfection in HEK293T cells, lysates confirmed SNAP-APJ overexpression with a SNAP substrate gel (**Figure 4.2A**) as well as western blot analysis with an anti-APJ antibody (**Figure 4.2B**) confirming expression of both SNAP and APJ, respectively.

To explore the stability of overexpressed APJ, we performed a cycloheximide chase degradation assay in transfected HEK293T cells to quantify the degradation half-life of APJ (**Figure 4.3**). The cycloheximide chase assay is widely recognized as a method to inhibit protein synthesis and determine protein half-life by visualizing intracellular protein degradation (10). This experiment confirms that APJ is stable and has a degradation half-life of 2.2h.

The functionality of APJ in HEK293T cells was confirmed through the changes in activation of two different downstream signaling cascades following incubation with different

agonists. The schematic for APJ signaling can be found in **Figure 1.7**. APJ signaling is predominantly governed by a $G\alpha_i$ subunit, meaning activation of APJ leads to a decrease in cAMP. As observed in **Figure 4.4A**, the baseline of intracellular cAMP content in APJ-HEK cells is higher than Empty-HEK cells, due to the overabundance of GPCRs resulting from APJ overexpression. When normalizing the cAMP content to untreated APJ-HEK cells though, we see the expected decline in cAMP levels with the addition of agonist AP-13 (**Figure 4.4B**). Another common avenue of downstream signaling activation is the phosphorylation of MAPK through APJ's subunit $G\alpha_q$, which is increased following a 15-minute incubation with pyr-AP-13 (**Figure 4.4C**). The validation of APJ overexpression, stability, and functionality following transfection confirmed that this SNAP-APJ plasmid will be suitable for further experimentation.

4.3.2 Overexpression of APJ in HCMs

Although transfection conditions were optimized to achieve maximal APJ overexpression in HEK293T cells, these conditions proved too harsh in human ventricular cardiomyocytes so transfection conditions had to be reoptimized in HCMs. Following the new optimized protocol found in **Section 4.2.4**, with reduced lipofectamine concentrations and increased plasmid content, we observed increases in APJ protein expression (**Figure 4.5A**) and mRNA (**Figure 4.5B**) in HCMs. Additionally, we analyzed how APJ overexpression in HCMs altered mRNA expression of apelin (**Figure 4.5C**).

Furthermore, viability assays demonstrated that there was no change in cell survival following APJ overexpression (**Figure 4.6**). All viability assays were centered around the notion that we would eventually be conducting a 48h hypertrophy treatment with PMA, as validated in **Chapter 3, Section 3.3.2**. Based on preliminary data, we believed the most promising changes would be observed with a 2h apelin pretreatment to promote APJ receptor priming (11). We

decided to continue this apelin treatment along with the hypertrophy treatment and termed it a "rolling" apelin treatment. A schematic of this treatment regimen can be found in **Figure 4.7** to assist in clarity. Before proceeding to the hypertrophy treatment, it was necessary to determine if the rolling apelin treatment alone alters viability. Notably, there was a significant increase in viability in both Empty- and APJ-HCMs treated with 500 nM pyr-AP-13 (**Figure 4.6**).

4.3.3 PMA treatment in control cells and those expressing APJ

In control Empty-HCMs, PMA treatment resulted in a 60% decrease in viability, while APJ-HCMs demonstrated about a 70% reduction in cell viability, although this difference between experimental groups was not statistically significant (**Figure 4.8A**). In both Empty- and APJ-HCMs, 500 nM pyr-AP-13 treatment did not rescue viability, although in APJ-HCMs pyr-AP-13 treatment just missed the significance cut off with a Pval = 0.06 when compared to the PMA treatment alone (**Figure 4.8B**).

Our next step was to investigate how rolling apelin treatments with pyr-AP-13 and AP-17 altered *NPPB* expression in HCMs treated with PMA. We used the expression of *NPPB*, the cardiac hypertrophy biomarker, to explore the severity of cardiac hypertrophy following the addition of the components of the AS, where a higher *NPPB* expression signified increased hypertrophy. We optimized apelin concentrations to maximize observed *NPPB* changes while better mimicking endogenous apelin concentrations. It is interesting to note that PMA treated cells that overexpressed APJ had lower *NPPB* values compared with control cells (**Figure 4.9**) even without apelin treatment. Additionally, in the absence of APJ, apelin treatment resulted in increased *NPPB* in the cells, but *NPPB* expression decreased when APJ and apelin were both present in the cells (**Figure 4.9**).

4.3.4 Cardiomyocyte transcriptome changes due to the addition of the AS components

To begin, we wanted to determine how the different components of the AS (i.e. overexpressing APJ, or externally adding pyr-AP-13 or AP-17) alter the cardiomyocyte's ability to maintain homeostasis at the transcriptome level. RNA was isolated from twelve different experimental groups (n=3 each) and sent to Novogene for mRNA-sequencing to tease out pathway perturbations due to changes in the AS components. In this section we will be focusing on 6 of these groups (Empty-HCMs and APJ-HCMs either untreated, treated with pyr-AP-13, or treated with AP-17) in order to assess the global effects of introducing components of the AS on the healthy cardiomyocyte transcriptome. We will introduce the samples treated with PMA in the next section. A DESeq2 analysis was applied to generate a preranked list of differentially expressed genes based on significance within the different datasets, and a PCA was performed to analyze variation between the Empty-HCM and APJ-HCM samples. The PCA analysis demonstrated clear separation between the experimental groups transfected with either empty SNAP vector or SNAP-APJ plasmid, but there was no clear separation observed between samples that were untreated vs those treated with either pyr-AP-13 or AP-17 (**Figure 4.10**). This finding suggests that there were minimal transcriptome variations due to the exogenous addition of both apelin isoforms compared to the no apelin controls.

4.3.4.A APJ overexpression alters the healthy cardiomyocyte transcriptome

Pathway analysis suggests that APJ overexpressing cells are undergoing resource overload due to excessive protein production. It is well known that there are many cellular consequences caused by overexpressing certain proteins, so we found it vital to analyze the changes observed due to APJ overexpression in control cells prior to analyzing AS linked

changes under hypertrophic conditions. The preranked DESeq2 analysis completed for the APJ-HCMs compared to the Empty-HCMs was utilized in a GSEA, where genome wide perturbations based on APJ overexpression were mapped onto biologically relevant pathways. GSEA uncovered many changes suggestive of the HCMs transfected with APJ undergoing both resource overload and stoichiometric imbalance, observed through increases in energy metabolism and translation, and decreases in ECM organization (**Figure 4.11**). Due to this discovery, we ensured all further transcriptomic analyses controlled for APJ overexpression changes first before considering secondary changes due to hypertrophy induction or externally added apelin.

4.3.4.B Apelin treatment modulation of the healthy myocyte transcriptome

Cardiomyocyte treatment with pyr-AP-13 or AP-17 leads to activation of different pathways. Similarly to the analysis completed with APJ overexpressing HCMs, a GSEA was completed with the preranked DESeq2 analyses comparing untreated Empty-HCMs to Empty-HCMs treated with either 250 nM pyr-AP-13 or 250 nM AP-17. Treatment with pyr-AP-13 resulted in increases in pathways crucial for translation and decreases in pathways imperative to cholesterol biosynthesis and metabolism (**Figure 4.12**). Myocytes treated with AP-17 led to increases in pathways linked to cellular energy metabolism, mitochondrial translation, and the ribosome, and decreases in helicase activity and eicosanoid secretion (**Figure 4.13**). These findings are intriguing and suggest that pyr-AP-13 and AP-17 may play different roles in cardiomyocyte homeostasis even though they bind to the same receptor.

4.3.5 AS components alter the cell's response to hypertrophy

Using the hypertrophy model validated in **Chapter 3, Section 3.3.2**, we investigated changes in the hypertrophy response following a 48h PMA treatment to induce cardiac

hypertrophy along with modulation of APJ expression in HCMs with exogenous addition of pyr-AP-13 or AP-17. Here we introduce the final 6 experimental groups subjected to RNA-sequencing: Empty-HCMs and APJ-HCMs either treated with PMA, AP-17 + PMA, or pyr-AP-13 + PMA. A PCA plot with all of the samples, both vehicle treated (previously described), and PMA treated samples, demonstrated a distinct separation between vehicle and PMA treated samples, with less severe variation observed between Empty- and APJ-HCMs (**Figure 4.14**). As observed with the healthy cardiomyocytes, neither Empty-HCMs nor APJ-HCMs had large and distinct transcriptome changes due to treatment with the different apelin analogs.

With PMA treatment alone, there were many observed changes in crucial pathways for cardiomyocyte homeostasis. Increases in pathways imperative to lipid metabolism, ferroptosis, glycosylation, and hypoxia were detected, as well as decreases in pathways important for calcium regulation, cellular energy metabolism, and the cell cycle (**Figure 4.15**). All of these pathway changes indicate that the cardiomyocytes are undergoing intracellular changes concurrent to those that occur during the onset of cardiac hypertrophy. A similar analysis was conducted in **Chapter 3, Section 3.3.4** and described in **Chapter 3, Section 3.4.2**, but slightly different pathways were chosen to be highlighted in this chapter.

To investigate the hypertrophy response changes due to addition of the different components of the AS, an interaction analysis known as a likelihood ratio test was necessary. An LRT analysis can tease out changes by controlling for two different exposures (one being a component of the AS, and the other being PMA treatment). In the following sections we will explore how the cellular response to hypertrophy changes due to increased APJ expression (**4.3.5.A**), the addition of exogenous pyr-AP-13 or AP-17 (**4.3.5.B**), or a combination of APJ overexpression and apelin treatment (**4.3.5.C**).

4.3.5.A Hypertrophic response changes due to APJ overexpression

To analyze the changes in the cardiomyocyte hypertrophic response due to APJ overexpression, we controlled for both APJ overexpression changes and PMA treatment changes with our LRT analysis. This comparison identified 32 genes (FDR < 0.05) that changed significantly in the PMA response due to APJ overexpression. This gene list was analyzed through a WebGestalt over-representation analysis to transition from a gene list into biologically relevant functional pathways (12). These 32 genes mapped onto pathways that play roles in the metabolism and biosynthesis of lipids, translation, and the immune response (**Figure 4.16**), suggesting that APJ expression alters the PMA response potentially through these pathways.

4.3.5.B Hypertrophic response changes due to the external addition of pyr-AP-13 or AP-17

Apelin treatment caused minimal changes in the hypertrophic response in the absence of APJ overexpression. Two LRT analyses were completed to analyze apelin treatment changes in the hypertrophic response. In these LRT analyses, we controlled for the Empty-HCM PMA response both in the presence and absence of treatment with either pyr-AP-13 or AP-17. Intriguingly, without APJ overexpression, there was little changed in the cardiac hypertrophy response following PMA treatment. There were no identified gene changes following pyr-AP-13 + PMA treatment, and only 3 identified gene changes (FDR < 0.05) following AP-17 + PMA treatment compared to PMA treatment alone. The three genes changed due to the AP-17 PMA response are *PLIN2* (perilipin 2), *STC2* (stanniocalcin 2), and *PTGS2* (prostaglandin-endoperoxide synthase 2).

4.3.5.C Hypertrophic response changes due to both APJ overexpression and apelin treatment.

Responses to AP-17 treatment in the presence of APJ exhibited alterations in the hypertrophic response when compared to the AP-17 hypertrophic response without APJ expression. In the presence of APJ overexpression, there were no differences in the hypertrophic response with pyr-AP-13 + PMA treatment, but there were 160 genes identified as being different following the AP-17 + PMA treatment. These LRT analyses indirectly controlled for APJ overexpression changes by analyzing gene changes in the PMA response compared to the vehicle treatment in APJ-HCMs. Additionally, these LRT analyses controlled for the apelin + PMA response compared to the apelin + vehicle response in the APJ-HCMs. Notably, the genes identified as being altered due to AP-17 + PMA treatment in the APJ-HCMs were consistent with changes in pathways responsible for the cell cycle, immune response, ECM organization, insulin regulation, and other cellular changes (**Figure 4.17**). The fact that changes with PMA and AP-17 treatment were significant only in the presence of APJ overexpression, suggests that AP-17 plays a larger role in the cardiac hypertrophy response when there is an abundance of APJ present in the cells, as opposed to cells with very low or nonexistent APJ expression.

When considering the addition of two AS components: APJ expression and apelin treatment, there are changes in the hypertrophic response due to AP-17 treatment, but not pyr-AP-13 treatment. LRT analyses were completed, controlling for APJ overexpression, and PMA + apelin treatment. These analyses identified genes changed due to apelin treatment and APJ expression. Interestingly, there were no observed changes due to pyr-AP-13 treatment in addition to APJ expression, but there were 32 genes identified as being altered due to AP-17 treatment

and APJ expression. These genes mapped onto just two significant pathway changes: the metabolism of amino acids and serine glycine biosynthesis (**Figure 4.18**).

4.4 Discussion

4.4.1 Summary of results

In this study, we investigated the consequences of increasing expression levels of APJ or availability of different apelin isoforms and further explored how these changes altered the hypertrophic response. The key finding in this study is that the components of the AS play different roles in the heart and contribute to changes in different downstream pathways following the induction of hypertrophy. In this discussion section, we will start by presenting the development and validation of a SNAP-APJ plasmid. We will then discuss the remainder of the results based on the cardiomyocyte's altered response to hypertrophy due to an increase in APJ expression, exogenous apelin treatment, or both.

4.4.2 SNAP-APJ plasmid leads to overexpression of stable and active APJ

Initially, we began by creating a plasmid that resulted in stable and functional APJ overexpression in HEK293T cells. As the C-terminal tail of a GPCR is crucial for downstream signaling (13), we ligated a SNAP-tag to the N-terminal domain of APJ. Transfection with the SNAP-APJ led to increases in both SNAP and APJ protein expression in HEK293T cells (**Figure 4.2)**. A cycloheximide chase assay demonstrated APJ's membrane stability (**Figure 4.3**), and suggested APJ had a relatively long degradation half-life compared to other GPCRs, although not much is known about GPCR degradation (10).

Additionally, we used two methods in HEK293T cells, a cAMP assay and quantification of MAPK phosphorylation to test if the overexpressed APJ was functional. Signaling through

APJ triggers different downstream effects, mediated by the attached Gα subunits (14). The predominant Gα subunit is $G\alpha_i$, indicating that APJ activation leads to an inhibitory effect on cAMP production. As APJ signaling is complex and convoluted, we examined both multiple time points and multiple agonist concentrations to attempt to pinpoint the most optimal conditions to observe functional changes initiated by APJ activation. Another intricate response of APJ that needs to be taken into consideration when conducting these experiments is that APJ is prone to agonist-induced internalization, which can lead to recycling of the receptor back to the cell surface or receptor degradation by lysosomes (11). As expected, we did observe a decrease in forskolin induced cAMP production following a 5-minute incubation with agonist AP-13 (**Figure 4.4B**). Intriguingly though, the dose-dependent inhibition was opposite of what was expected, where the lowest concentration of AP-13 led to the highest degree of inhibition of cAMP production. This may be due to many contributing factors, but our current hypothesis is that with the higher concentrations of AP-13, we are eliciting increased receptor internalization, which desensitizes the system to further activation (15).

APJ is also coupled with a $G\alpha_q$ subunit, where activation by an agonist leads to MAPK phosphorylation (14), which was observed following a 15-minute stimulation with pyr-AP-13 (**Figure 4.4C**). Taken together, this data suggests that the SNAP-APJ plasmid leads to an active and functional receptor that can be utilized for further experimentation. Since we characterized the SNAP-APJ plasmid in HEK293T cells due to their ease of use and successful history of GPCR characterization (9), conditions had to be reoptimized to maximize the response from the AS with agonist treatment in HCMs as well, but these optimizations will be discussed further in their respective AS section.

4.4.3 Cardiomyocyte changes in the transcriptome due to APJ overexpression

Transfection in HCMs led to an observed increase in APJ protein and mRNA expression, as well as a significant decrease in apelin mRNA expression (the gene that encodes the 77 amino acid preproapelin isoform) (**Figure 4.5**). It is worth noting that although the apelin mRNA expression is decreased, we are unsure how this affects the different apelin isoform concentrations. Due to the complexities of APJ regulation and signaling we are hesitant to speculate on why this could be the case. With APJ overexpression alone no changes in cell viability were observed following vehicle treatment (**Figure 4.6**). Interestingly, with PMA treatment alone, APJ-HCM viability decreased slightly compared to Empty-HCMs, but this did not reach the threshold for significance (**Figure 4.8**). With PMA treatment however, there is less observed *NPPB* in APJ-HCMs (**Figure 4.9**). Taken together, this data suggests that APJ alone may be protective against the development of hypertrophy, but more work is needed to fully understand these cellular responses.

Transcriptome changes due to APJ overexpression is indicative of excessive protein production. Overexpressing proteins can lead to cellular changes and toxicity due to resource overload, stoichiometric imbalance, promiscuous interactions, and pathway modulation (16). This is a limitation in our study, but since the HCMs do not endogenously express APJ at very high levels, we are not able to silence the expression of APJ to investigate changes in the cell response. With the overexpression of APJ alone, some of the pathway changes are suggestive of resource overload within the HCMs (**Figure 4.11**). Observed increases in pathways critical to translation, energy metabolism, translocation machineries, and post translational modifications, as well as decreases in the ECM organization are all characteristic changes instigated by the overproduction of proteins (16,17). Additionally, we observed overall dysregulations in cell

growth and a decline in $G\alpha_s$ signaling. Since APJ is a GPCR this could indicate stoichiometric imbalance due to reallocation of $G\alpha$ protein subunits within the cells due to the overexpression of APJ. Interestingly though, we did note a decrease in pathways that play a role in cardiomyopathy and cholesterol metabolism, which cannot be explained through the overexpression of proteins as a whole and may be a result of the overexpression of APJ. To minimize overexpression bias while investigating the mechanistic consequences of APJ overexpression, we chose to control for APJ overexpression in all further transcriptomic analyses.

An LRT test identified 32 genes altered in the hypertrophic response due to APJ overexpression alone. This analysis controlled for both APJ overexpression and the PMA response, teasing out changes in lipid metabolism and biosynthesis, translation, cholecystokinin (CCK) signaling, and interleukin-10 signaling (**Figure 4.16**). Experimental evidence has shown that both CCK and interleukin-10 levels may be correlated with heart failure and could serve as potential biomarkers (18–20). Additionally, it is common for cardiomyocytes to undergo metabolic switching during the development of cardiac hypertrophy, where hypertrophied hearts rely more on glucose for energy production than fatty acids (21), and translation is a common dysregulation when it comes to cardiac hypertrophy (22). Taken together, these changes suggest that APJ plays a crucial role in critical pathways that are thought to be altered in hypertrophy. The directionality of these changes cannot be determined through this analysis, but these results highlight some important pathways that have biomarker potential in distinguishing healthy hearts from diseased hearts, thus warranting further investigation to elucidate the specific role the apelin receptor plays without increasing the ligand.

4.4.4 Changes in cardiomyocyte responses due to apelin treatment

Preceding hypertrophy treatment, many apelin pretreatments were attempted to elicit the largest change in response through AS activation. Pope et al., demonstrated that 2h following pyr-AP-13 pretreatment, the proportion of APJ on the cell surface was significantly higher than in control cells, suggesting specific compartmentalization of APJ on the cell surface (11). Based on this theory and our preliminary results, we decided to use a "rolling" treatment for further testing. Here we dosed the HCMs with either pyr-AP-13, AP-17, or controls for 2h in order to prime APJ back to the cell surface following receptor activation and internalization with the apelin isoforms. Then the HCMs were re-dosed with their respective apelin treatments in addition to PMA, or vehicle controls, and analyzed for changes.

Viability was significantly increased following vehicle + pyr-AP-13 treatment in both Empty-HCMs and APJ-HCMs (**Figure 4.6**), while pyr-AP-13 + PMA treatment did not alter the cardiomyocyte's viability in either Empty-HCMs or APJ-HCMs (**Figure 4.8**). *NPPB* expression levels suggested that with the rolling treatment of either pyr-AP-13 and AP-17, Empty-HCMs had an increased amount of hypertrophy, although only pyr-AP-13 was statistically significant (**Figure 4.9**). These results suggest that for apelin to elicit protective effects against cardiac disease, APJ expression levels are crucial and treatment with apelin alone has no protective effect in the absence of the receptor. This confirms that the signaling properties of apelin mostly occur through APJ and not by binding to another receptor.

Pyr-AP-13 and AP-17 treatment influence activation of different pathways within control cardiomyocytes. Following the vehicle + apelin treatments in Empty-HCMs, we observed differing cellular responses with pyr-AP-13 and AP-17. Pyr-AP-13 treatment led to alterations in two large biological modules encompassing pathways imperative to increased translation and

decreased cholesterol biosynthesis and metabolism (**Figure 4.12**). There is considerable literature evidence to suggest that apelin and cholesterol-LDL levels are inversely related (23,24), so these findings are supportive of increased apelin content leading to a decline in pathways responsible for cholesterol biosynthesis. On the other hand, there were distinct changes observed following AP-17 treatment. Four biological modules were identified with AP-17 treatment in Empty-HCMs: increased cellular energy metabolism and mitochondrial translation, and decreased helicase activity and eicosanoid signaling (**Figure 4.13**). The effects of AP-17 signaling are not as well understood, but it is interesting to note that the cellular responses from both apelin isoforms are distinct from each other. These results suggest that both apelin isoforms lead to increased translation within the cells, but each apelin isoform may play different roles through their impact on different lipid species. How these changes in cellular response apply to other cell types such as liver or kidney requires investigation.

There were minimal changes in the hypertrophic response due to apelin treatment in the absence of APJ overexpression. An LRT analysis exploring the hypertrophic response changes due to pyr-AP-13 treatment in Empty-HCMs, returned zero genes, while an LRT analysis exploring the AP-17 hypertrophic response identified three unique genes: *PLIN2*, *STC2*, and *PTGS2*. These genes encode for the proteins perilipin 2, stanniocalcin 2, and prostaglandin-endoperoxide synthase 2. These proteins help increase lipid storage by promoting the formation of lipid droplets (25), regulate calcium and phosphate transport and homeostasis (26), and mediate the biosynthesis of prostaglandins (27), respectively.

4.4.5 Cardiomyocyte changes due to both APJ overexpression and exogenous apelin treatment

Viability changes due to apelin treatments are different in the presence of APJ overexpression, only when the cardiomyocytes are undergoing hypertrophy. There is a significant increase in viability in APJ-HCMs treated with pyr-AP-13 compared to controls, but there is no change in viability between Empty-HCMs and APJ-HCMs treated with pyr-AP-13 (**Figure 4.6**). There are, however, small changes in viability in pyr-AP-13 + PMA treated APJ-HCMs compared to PMA treatment alone in APJ-HCMs, although this finding just misses the significance cut off with a Pval of 0.06 (**Figure 4.8**). Additionally, with PMA treatment, there is an observed decrease in *NPPB* expression with APJ expression and either pyr-AP-13 + or AP-17 treatment (**Figure 4.9**). Taken together, these results suggest that perhaps both APJ and apelin must be present in order to protect against PMA induced hypertrophy, and the corresponding heart failure disease progression.

LRT analyses were also completed to address how apelin treatment alters the hypertrophic response in the presence of APJ. These analyses controlled for APJ expression indirectly, by comparing the PMA and vehicle response in APJ-HCMs. Similarly to the lack of response with pyr-AP-13 + PMA treatment, there were no genes identified as being altered in the hypertrophic response in APJ-HCMs, but there were 160 unique gene responses with the AP-17 + PMA treatment in APJ-HCMs (**Figure 4.17**). These genes mapped onto many different pathway changes including the cell cycle, immune response, and ECM organization, all of which are characteristic changes observed during the onset of cardiovascular disease (28–30). AP-17-APJ also mediated changes in the hypertrophic response due to insulin regulation and again, prostaglandin synthesis. Changes were also observed in the transcription factors CREB and

NRF-2. CREB1 (cAMP response element binding protein 1) is a transcription factor that is activated by PKA phosphorylation and is thought to play an important role in cardiovascular remodeling (31). Additionally, the KEAP1-NFE2L2 pathway is widely recognized as being cardioprotective due to its entanglement with NRF2-target genes leading to the promotion of antioxidant responses as well as the suppression of pro-inflammatory proteins (32). All these changes suggest that AP-17-APJ may play a role in crucial cardiomyocyte responses that influence hypertrophy progression. Unfortunately, directionality is not distinguishable through this analysis, but these results support that AP-17 and APJ play critical roles in cardiac hypertrophy progression, and these interactions should be further explored. The fact that the PMA response with AP-17 treatment is drastically different in the presence or absence of APJ expression suggests that there are crucial AP-17-APJ cellular responses that occur in the development of cardiac hypertrophy, but how these responses could be exploited in future therapies is a topic that requires further experimentation.

Finally, while running an LRT analysis to directly compare the two components of the AS: APJ expression and apelin addition, we identified changes in the hypertrophic response due to AP-17 + PMA treatment, but no changes were observed with pyr-AP-13 + PMA treatment. 32 genes were identified as being altered due to the role of both AP-17 and APJ in the hypertrophic response. These changes mapped onto only two pathways: amino acid metabolism and serine glycine biosynthesis (**Figure 4.18**). Interestingly, activating the serine biosynthesis pathway may serve as a treatment strategy for cardiomyopathy (33), suggesting again that the AP-17-APJ axis may serve as a regulator for CVD development. The consistent lack of change with pyr-AP-13 treatment leads us to believe that there are better ways to elicit an APJ response with pyr-AP-13

treatment instead of utilizing a rolling pyr-AP-13 + PMA treatment. Future work should focus on optimizing this response.

4.5 Conclusions

The AS plays an important role by mediating physiological responses within the cardiovascular system. Overexpression of APJ in cardiomyocytes altered the stress response of the cells, suggesting that increased APJ expression may protect against the progression of cardiac hypertrophy. Additionally, apelin treatment in control cells elicited different pathway changes depending on the apelin isoform. Pyr-AP-13 treatment decreased cholesterol biosynthesis, while treatment with AP-17 decreased eicosanoid signaling, suggesting that although both apelins work through APJ signaling, the isoforms may play different roles in lipid homeostasis and overall cell homeostasis. Analysis with both APJ and apelin treatment suggested that both elements of the AS must be present for apelin to elicit a change in the hypertrophic response. With both APJ expression and AP-17 treatment, there were changes in many crucial pathways for cardiomyocyte health, suggesting the AP-17-APJ axis may serve as a future target for CVD therapies.

To facilitate the development of apelin analogs that can bind to different regions on the receptor and elicit distinct signaling cascades, it is necessary to develop a reliable method to test for APJ binding. **Chapter 5** will discuss a potential solution to easily screen for APJ receptor binding to facilitate future development of APJ agonists that can have a positive impact on cardiovascular disease especially when conventional therapies are unsuccessful.

Figures

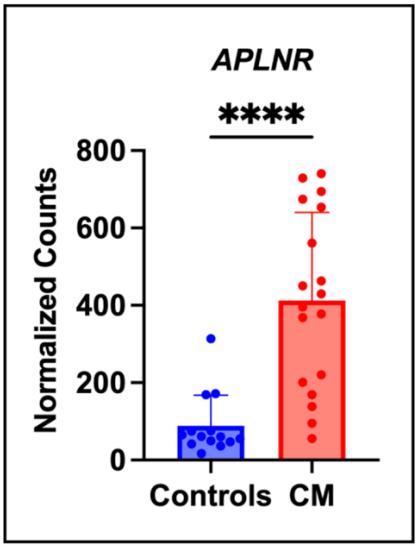

Figure 4.1. RNA sequencing shows increased APJ expression in diseased hearts.

APLNR (gene name for APJ) expression in human heart tissue in control subjects (n=14) or patients diagnosed with cardiomyopathy (CM) (n=18). **** $P < 0.0001$

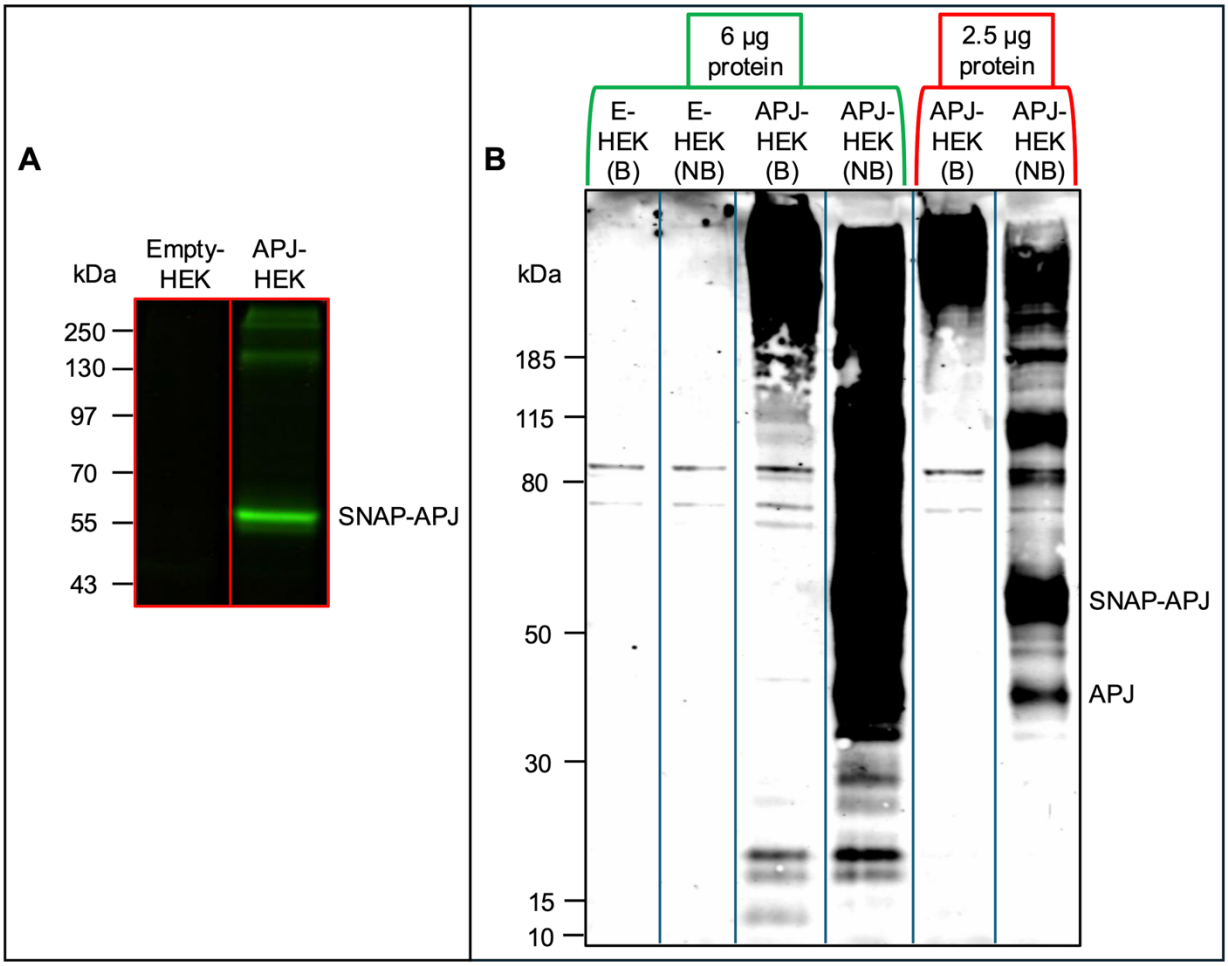

Figure 4.2. SNAP-APJ overexpression in HEK293T cells.

(**A**) SDS-PAGE gel with a SNAP substrate demonstrating that samples have the SNAP tag and (**B**) western blot with an anti-APJ antibody confirming cells are expressing APJ. SNAP-APJ can be found at ~62 kDa, while untagged APJ has a molecular weight of ~43 kDa. (Empty/E) – empty SNAP vector (B) – Boiled, (NB) – Not boiled

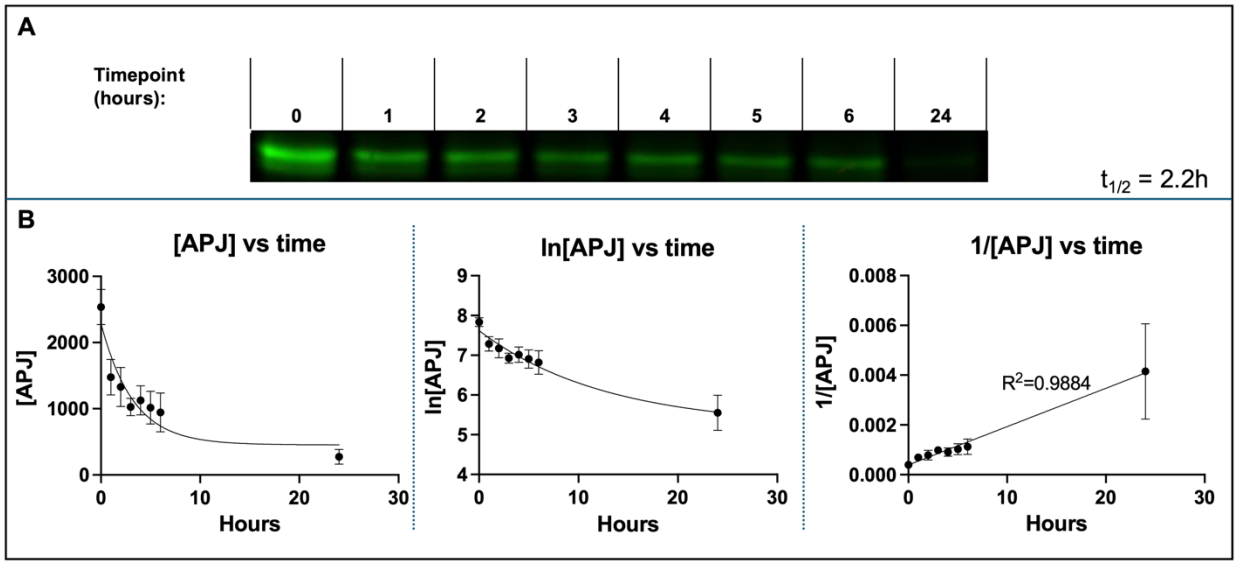

Figure 4.3. Cycloheximide chase assay of SNAP-APJ in HEK293T cells.

(**A**) Representative image of gel displaying SNAP-APJ protein levels in lysates at varying time points of cycloheximide treatment in HEK293T cells overexpressing APJ. (**B**) Degradation kinetics of APJ demonstrate that APJ degrades following second-order kinetics and has a degradation $t_{1/2}$ of 2.2h, n=3.

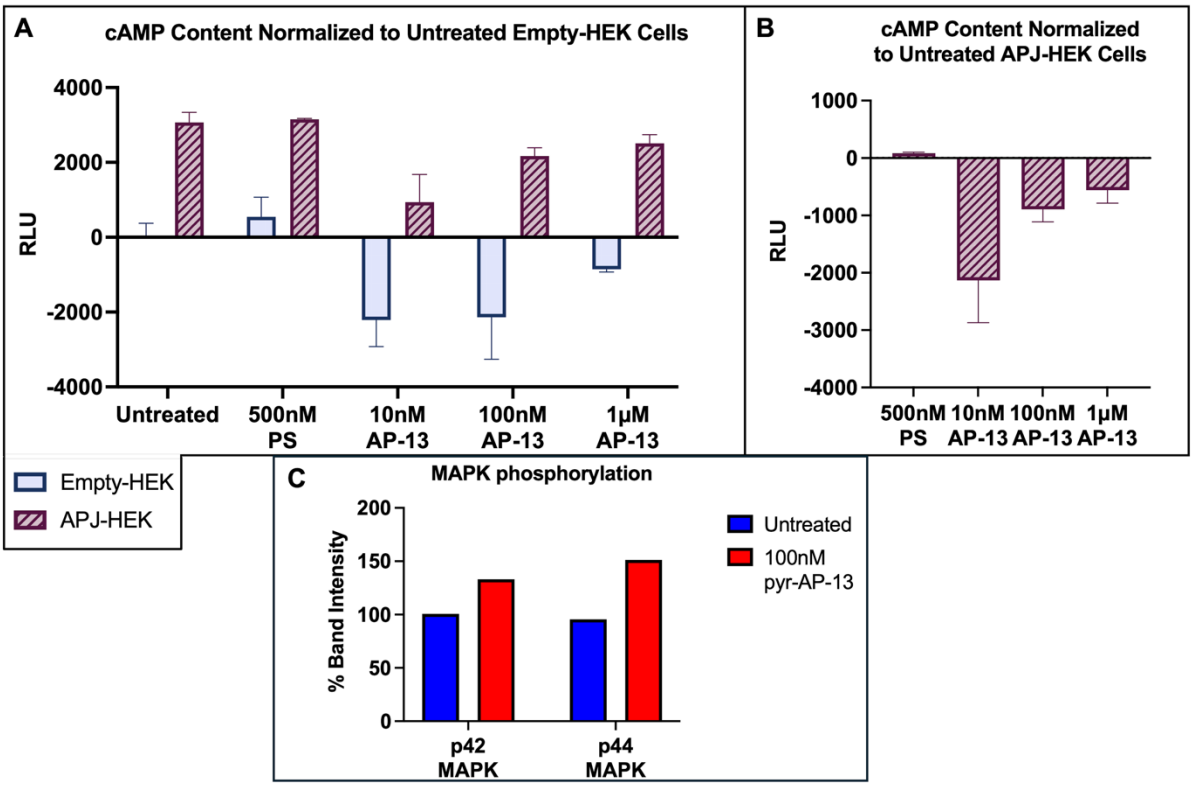

Figure 4.4. APJ functional assays.

(**A**) cAMP assay measured in relative light units (RLU). Following a 5 min incubation with antagonist protamine sulfate (PS) or agonist apelin-13 (AP-13), cAMP production was induced with 10 µM forskolin. Positive RLU values indicate more intracellular cAMP content than control cells. Data is normalized to the untreated Empty-HEK cells, n=3. (**B**) Data is normalized to the untreated APJ-HEK cells, n=3. (**C**) MAPK phosphorylation increases following 15 min stimulation with pyr-AP-13, technical replicates n=3.

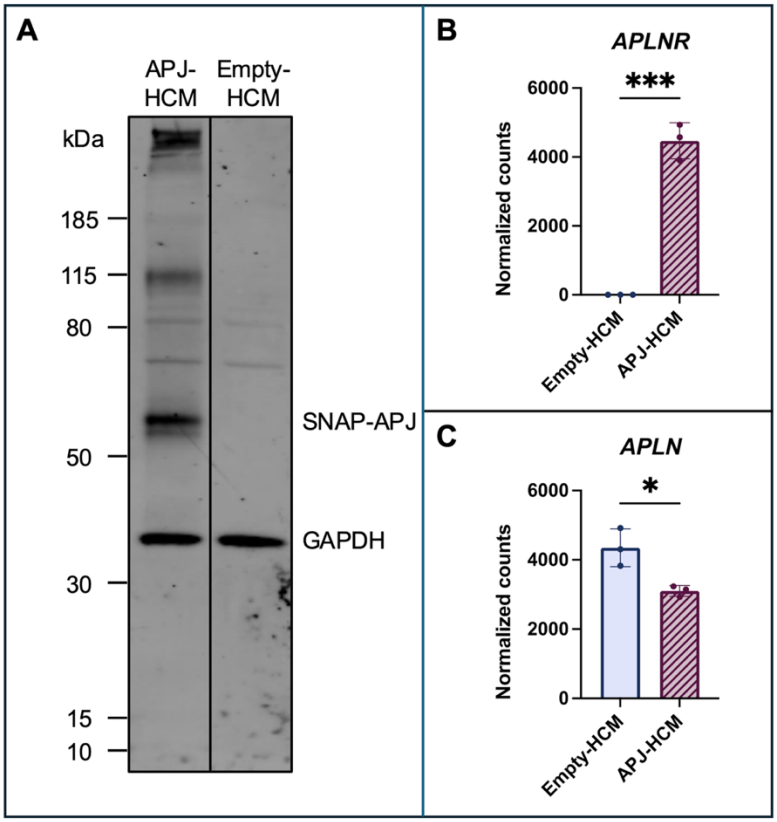

Figure 4.5. SNAP-APJ overexpression in immortalized human cardiomyocytes.

(**A**) Western blot analysis with an anti-APJ and an anti-GAPDH antibody. SNAP-APJ is at ~62 kDa, while the GAPDH band serves as a loading control and migrates at ~37 kDa. (**B**) *APLNR* (gene name for APJ) and (**C**) *APLN* (gene name for apelin) normalized gene expression from RNA-sequencing data in transfected HCMs. *** $P < 0.001$, * $P < 0.05$

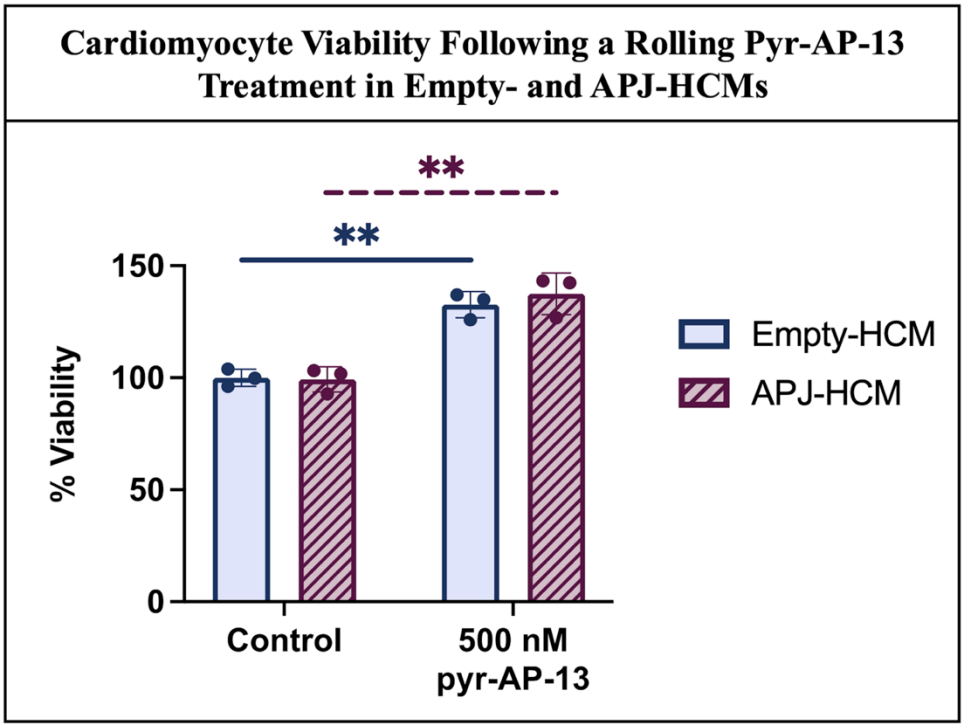

Figure 4.6. Viability assay following addition of the AS components.

Empty- and APJ-HCMs were treated with 500 nM pyr-AP-13 for 50h to assess viability changes. Data was normalized to the untreated Empty-HCM samples. ** $P < 0.01$

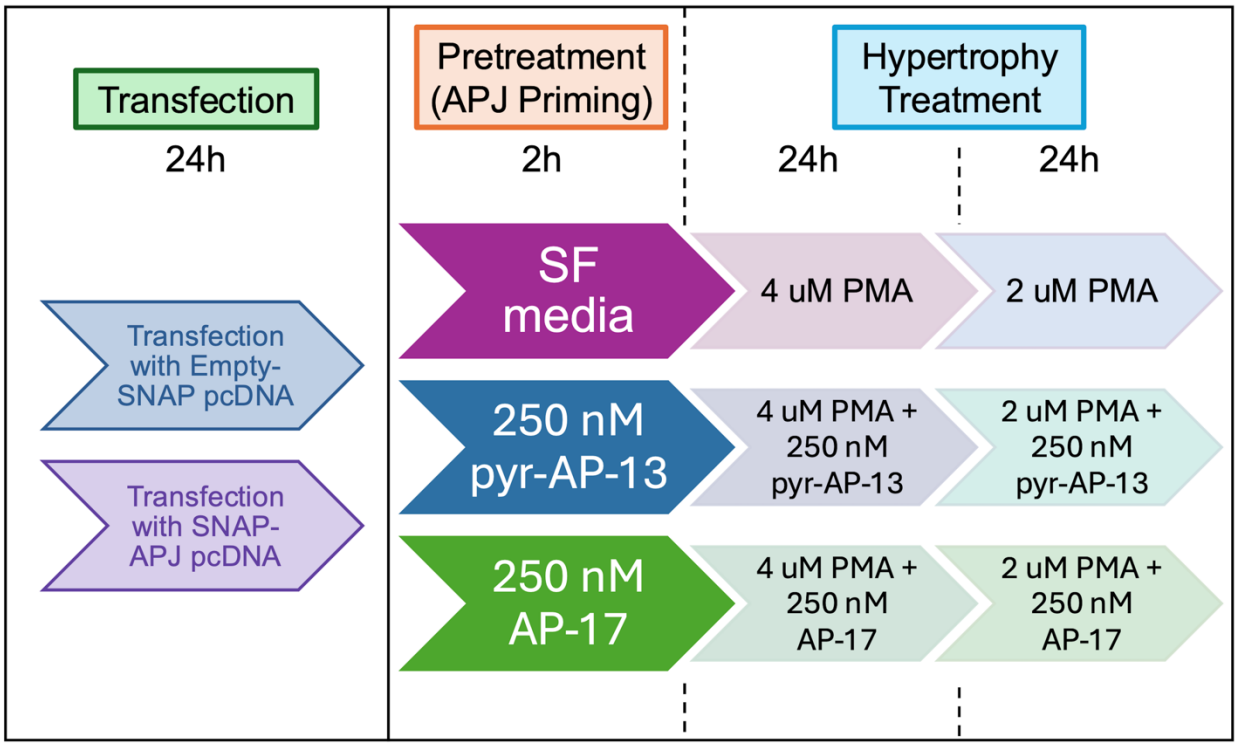

Figure 4.7. Apelinergic system hypertrophy treatment regimen.

HCMs were transfected with either Empty-SNAP or SNAP-APJ plasmids and left for 24h. Cells then underwent a 2h pretreatment with pyr-AP-13, AP-17, or a SF (serum free) media control to prime APJ back to the cell surface following agonist-induced internalization. At this point the hypertrophy treatment was initiated with a 4 µM PMA treatment in the presence of the respective apelin treatment or controls; this is termed a "rolling" apelin treatment. Twenty-four hours into this treatment, the HCMs were re-dosed with 2 µM PMA and the respective apelin or vehicle.

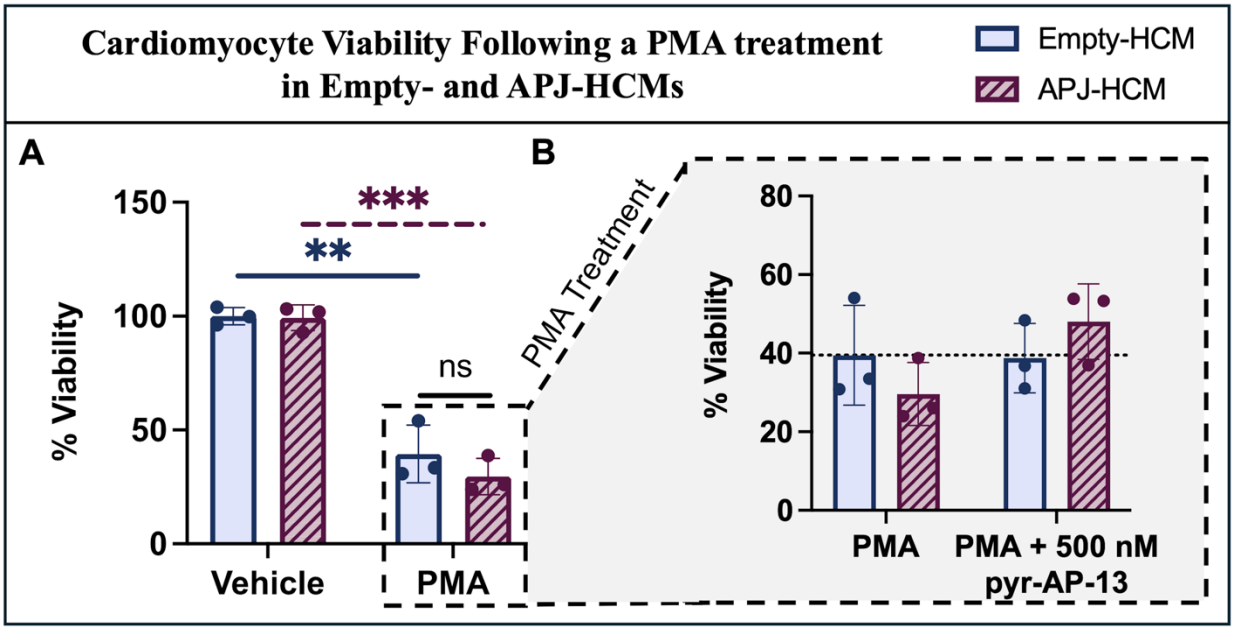

Figure 4.8. HCM viability following a 48h treatment with PMA.

HCM viability following PMA treatment in the (**A**) absence and (**B**) presence of a rolling pyr-AP-13 treatment. Data normalized to vehicle Empty-HCM samples. *** $P < 0.001$, ** $P < 0.01$

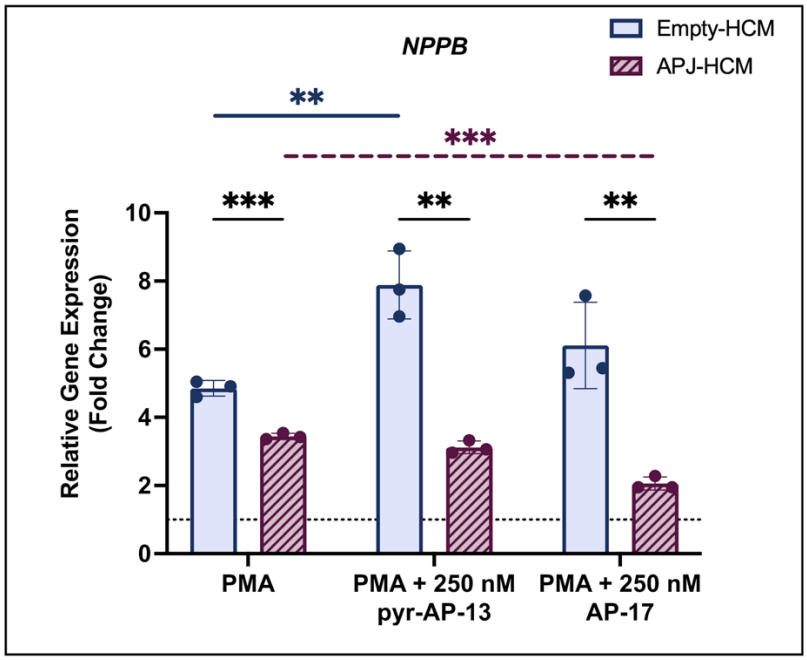

Figure 4.9. RT-qPCR analysis of *NPPB* following PMA treatment in the absence and presence of apelin in both Empty- and APJ-HCMs.

All counts were normalized to the housekeeping gene, *GUSB*, and fold change was determined through comparison of each respective vehicle control treatment. *** $P < 0.001$, ** $P < 0.01$

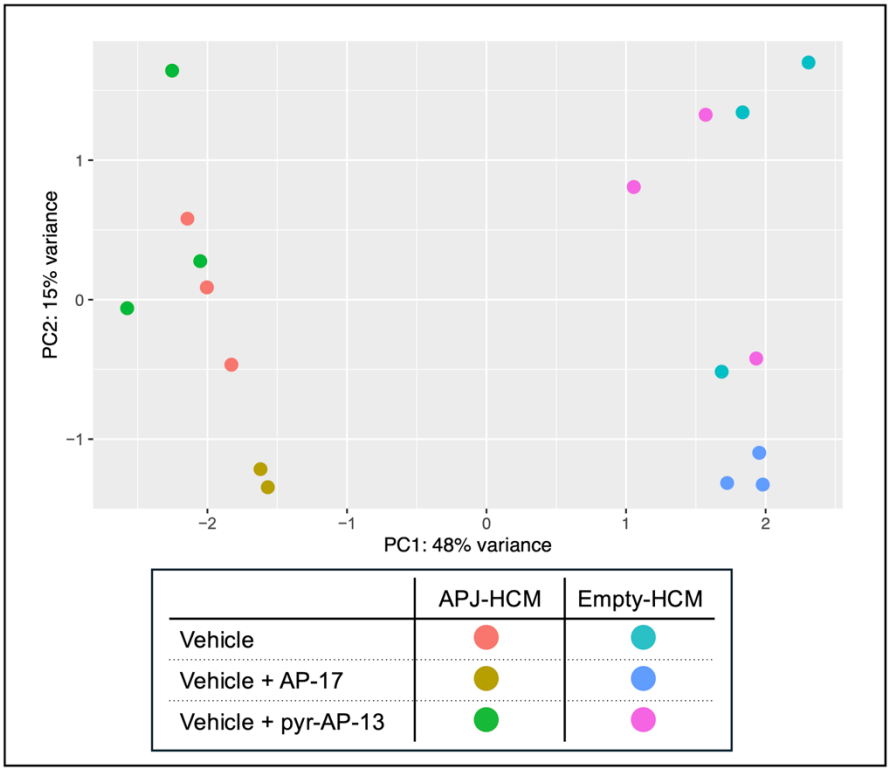

Figure 4.10. PCA plot displaying separation between Empty- and APJ-HCMs.

There were no distinct groupings observed following treatment with AP-17 or pyr-AP-13 in Empty- or APJ-HCMs.

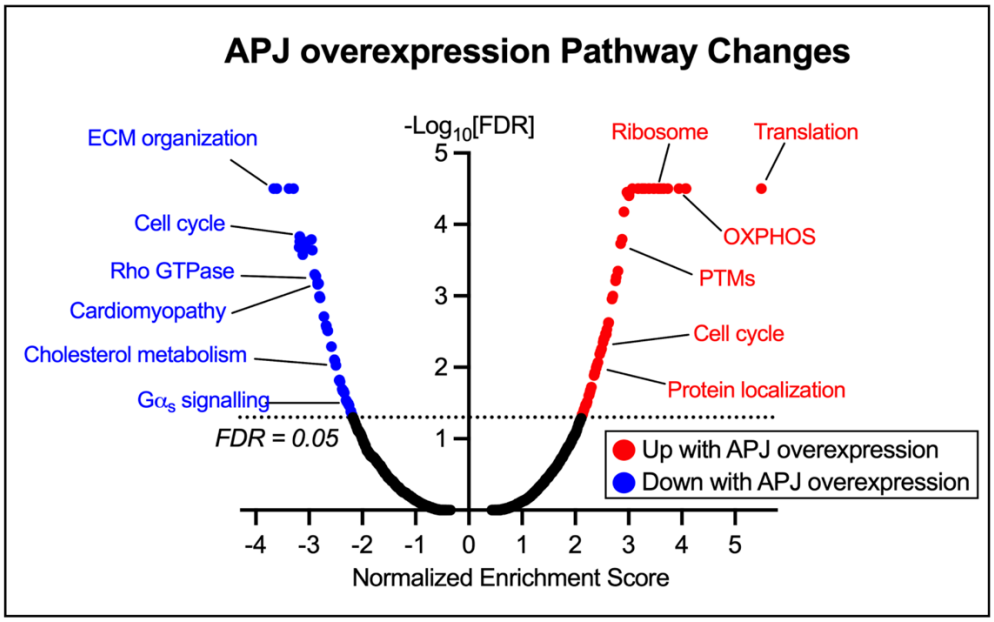

Figure 4.11. Volcano plot representing the major pathway changes due to APJ overexpression.

ECM – extracellular matrix, OXPHOS – oxidative phosphorylation, PTMs – post translational modifications

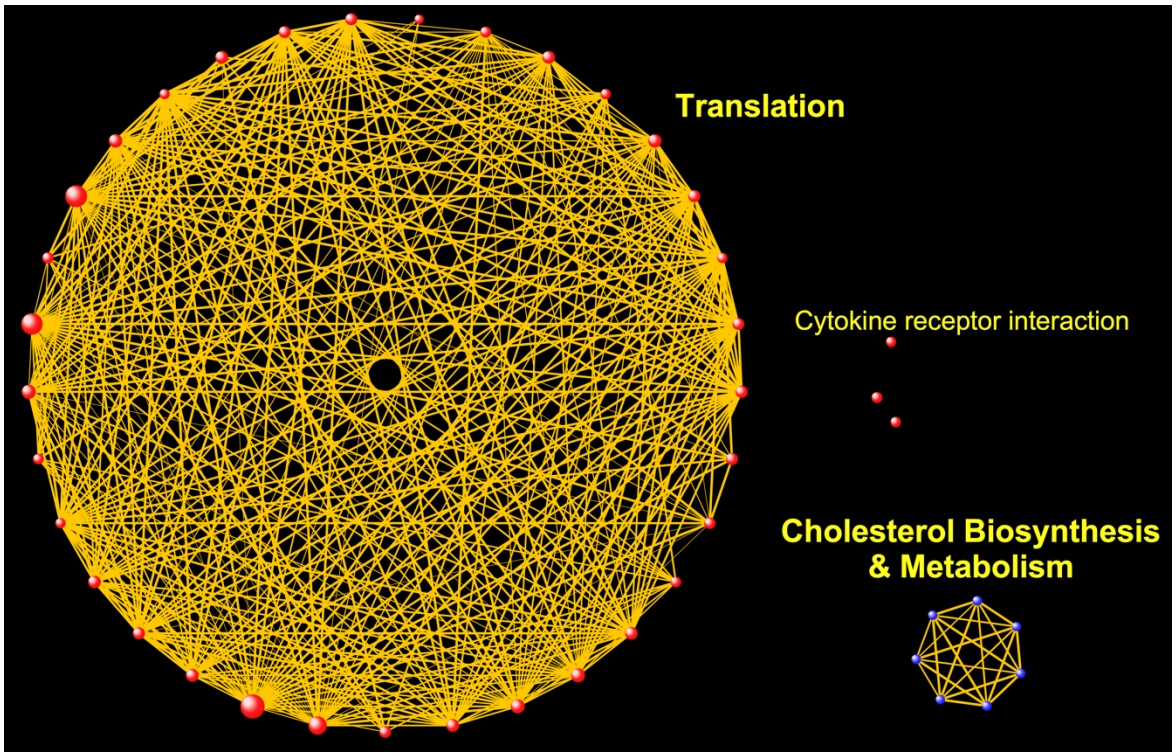

Figure 4.12. Network based summary of GSEA results due to 250 nM pyr-AP-13 treatment in Empty-HCMs.

Identified pathway changes (FDR < 0.05) were bundled into biological modules following a 50h treatment with 250 nM pyr-AP-13. Red spheres correspond to an upregulated gene set, while blue spheres represent downregulated gene sets. The spheres are connected if the gene sets contain over 50% overlap among their member genes.

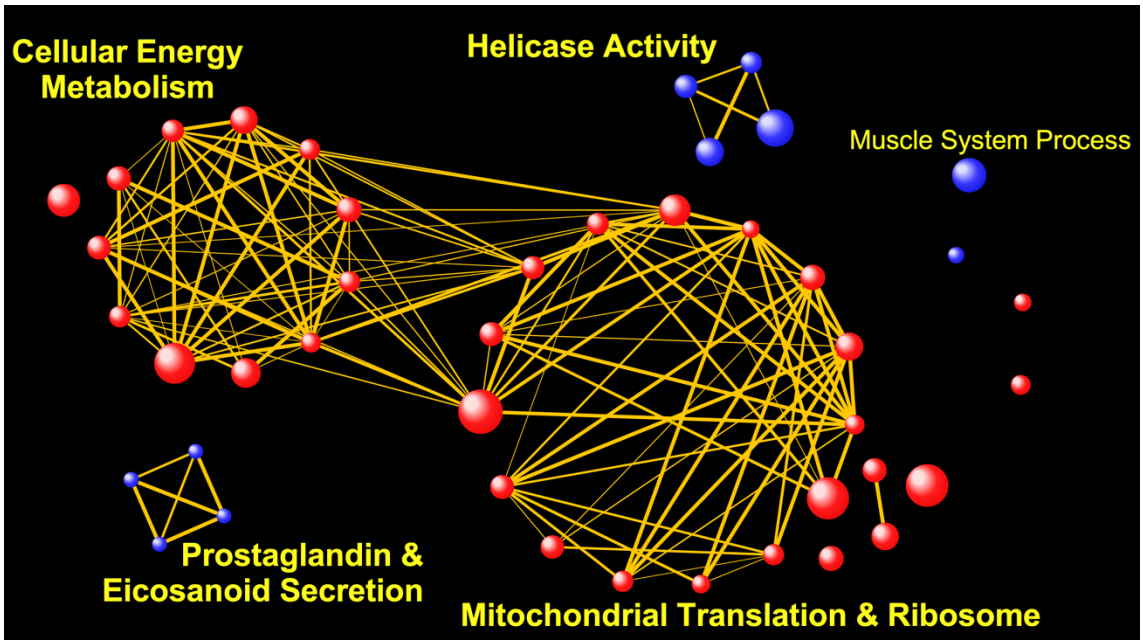

Figure 4.13. Network based summary of GSEA results due to 250 nM AP-17 treatment in Empty-HCMs.

Biological modules were constructed out of identified pathways changes (FDR < 0.05) following a 50h treatment with 250 nM AP-17. Red and blue spheres correspond to upregulated and downregulated gene sets, respectively. Connectivity between the spheres is observed if the gene sets contain over 50% overlap among their member genes.

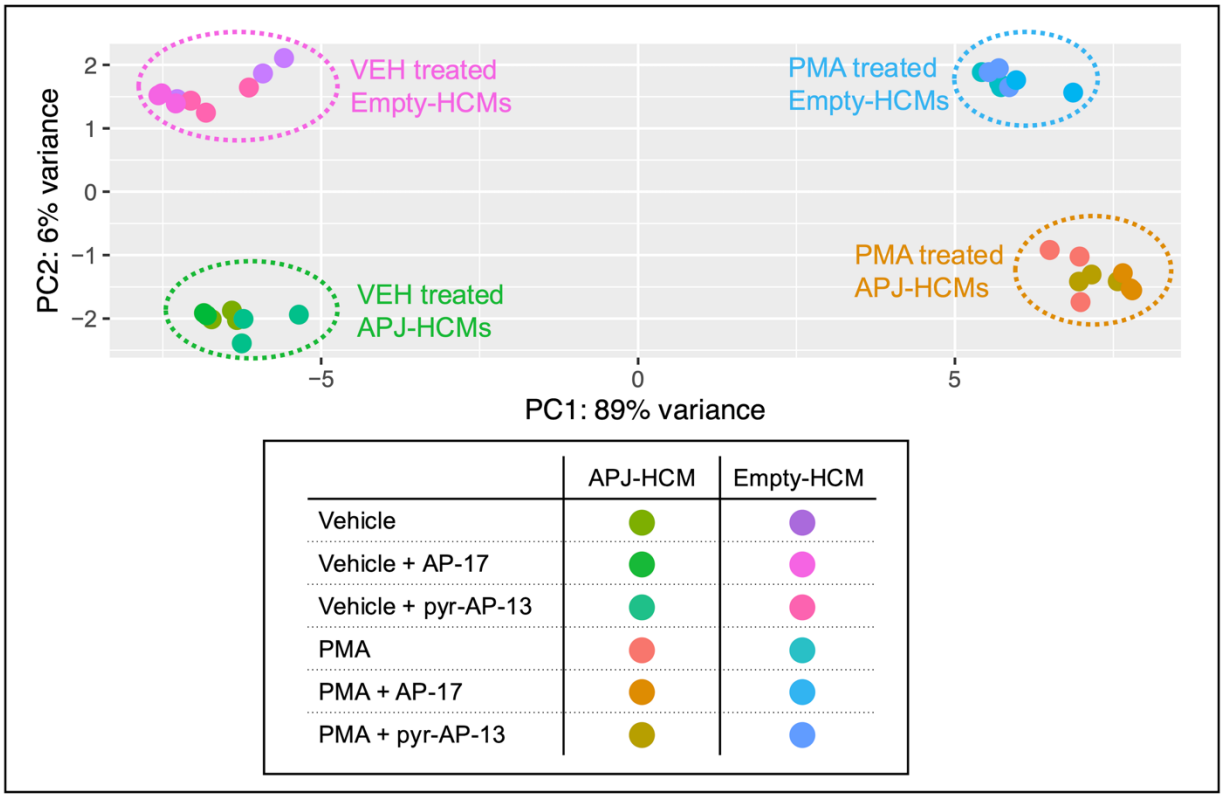

Figure 4.14. PCA plot with all RNA sequencing samples.

There is clear separation between vehicle and PMA treated samples, with less observed variation between the experimental groups transfected with Empty vector vs APJ. VEH – vehicle

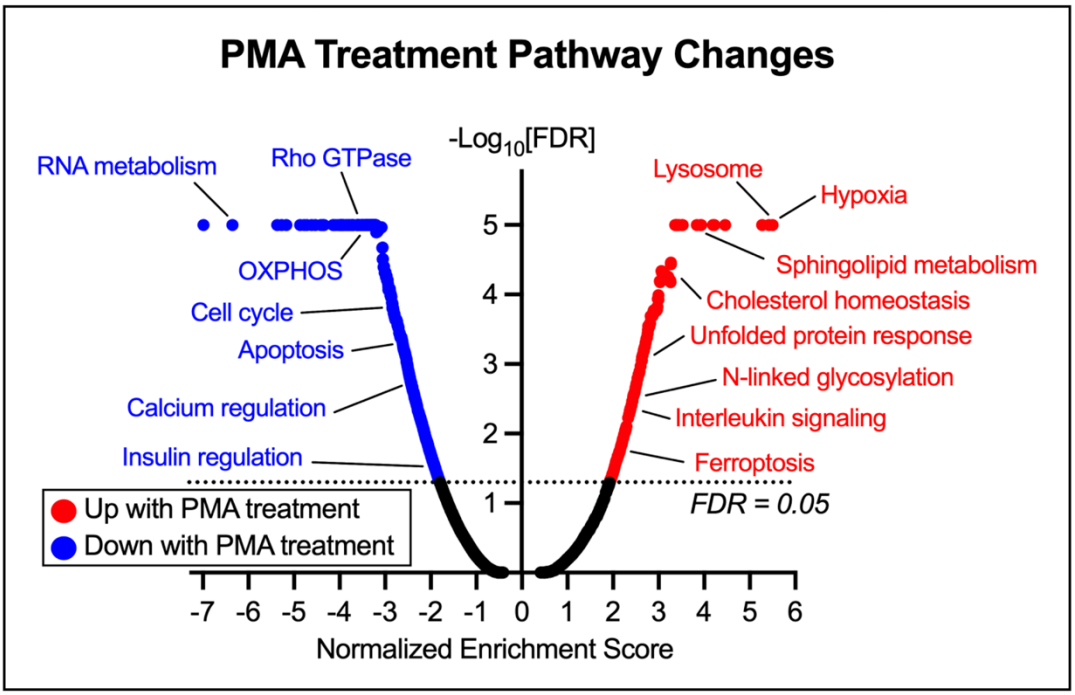

Figure 4.15. Volcano plot demonstrating respective pathway changes following PMA treatment compared to controls.

OXPHOS – oxidative phosphorylation

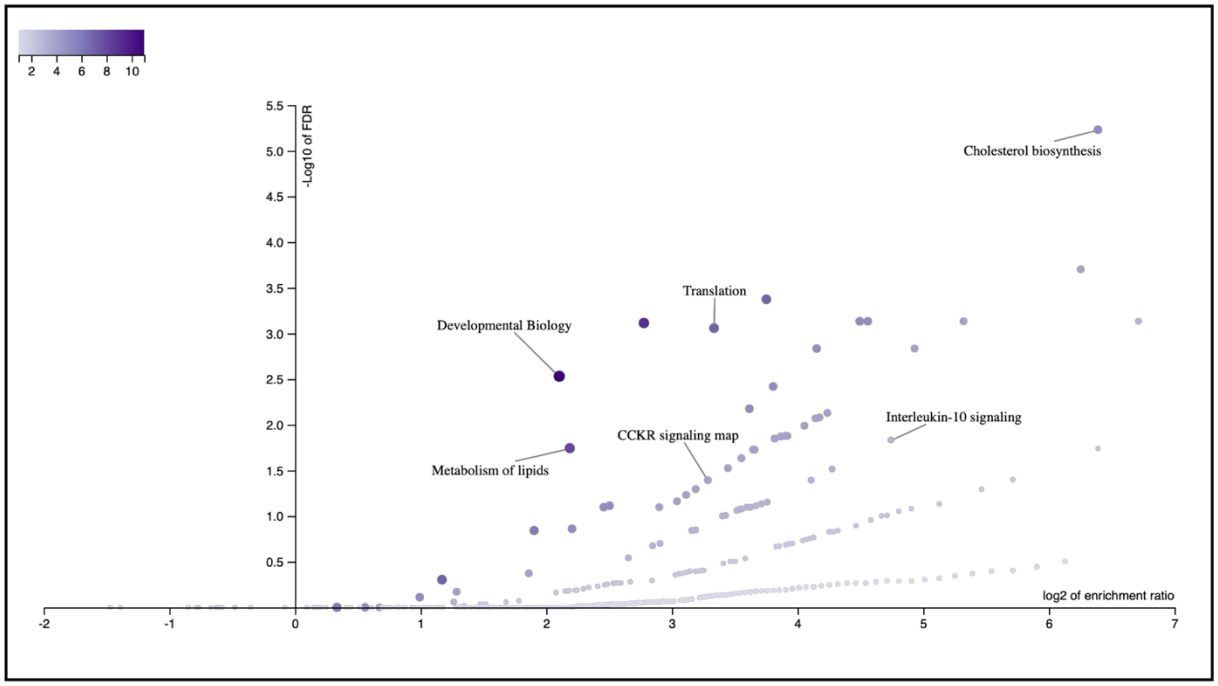

Figure 4.16. Pathways changes in the hypertrophic response due to APJ overexpression.

WebGestalt analysis that turns the observed DEGs identified with the LRT analysis controlling for PMA treatment and APJ overexpression into biologically relevant pathways. CCKR – cholecystokinin receptor

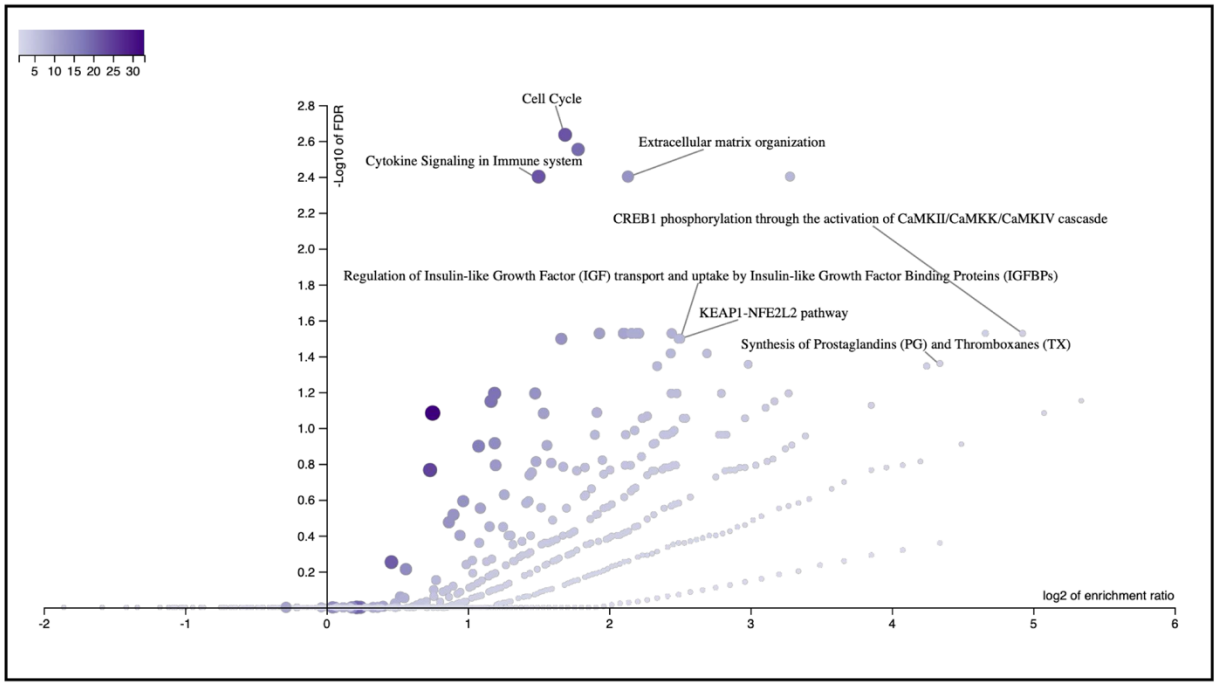

Figure 4.17. WebGestalt analysis identifying pathway changes due to AP-17 + PMA treatment in APJ expressing HCMs compared to the APJ-HCM PMA response alone.

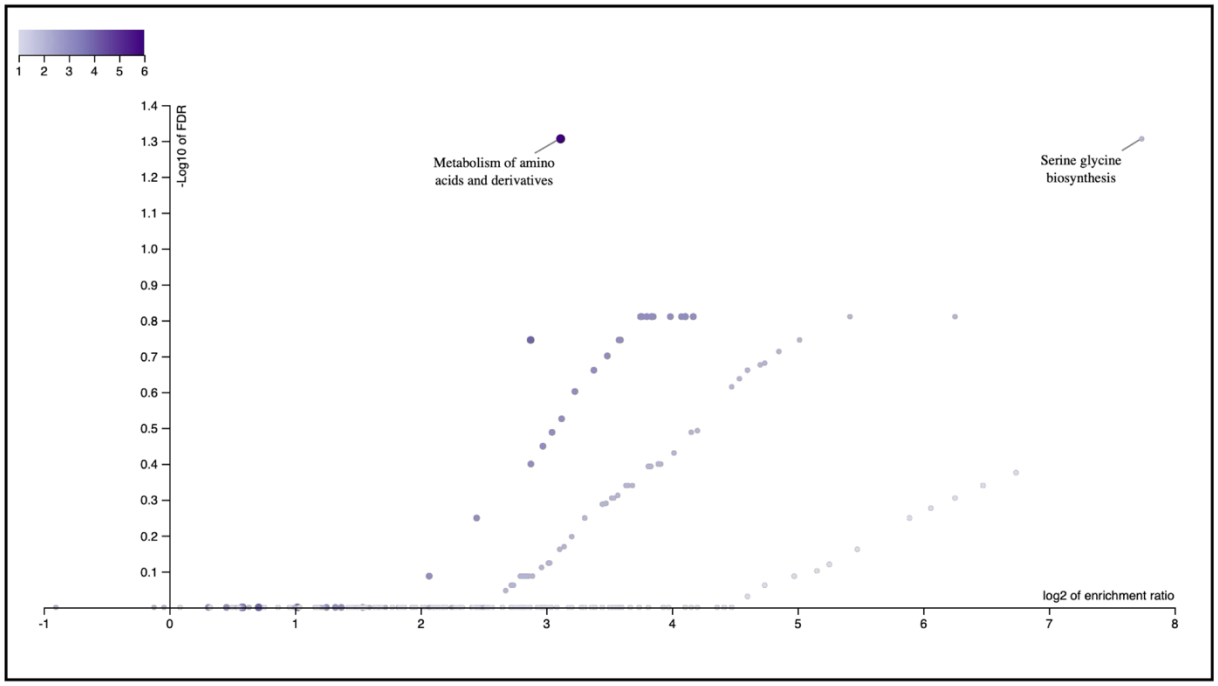

Figure 4.18. WebGestalt analysis identifying hypertrophy pathway changes due to both APJ overexpression and AP-17 treatment.

References

1. Shin K, Kenward C, Rainey JK. Apelinergic system structure and function. Compr Physiol. 2018 Jan 1;8(1):407–50.

2. Shin K, Landsman M, Pelletier S, Alamri BN, Anini Y, Rainey JK. Proapelin is processed extracellularly in a cell line-dependent manner with clear modulation by proprotein convertases. Amino Acids. 2019;51(3):395–405.

3. Chen J, Chen X, Li S, Jiang Y, Mao H, Zhang R, et al. Individual phosphorylation sites at the C-terminus of the apelin receptor play different roles in signal transduction. Redox Biol. 2020 Sep 1;36:101629.

4. Jiang Y, Yan M, Wang C, Wang Q, Chen X, Zhang R, et al. The Effects of Apelin and Elabela Ligands on Apelin Receptor Distinct Signaling Profiles. Front Pharmacol. 2021;12.

5. Iturrioz X, Gerbier R, Leroux V, Alvear-Perez R, Maigret B, Llorens-Cortes C. By Interacting with the C-terminal Phe of Apelin, Phe255 and Trp259 in Helix VI of the Apelin Receptor Are Critical for Internalization. J Biol Chem. 2010 Oct;285(42):32627–37.

6. Ma Y, Yue Y, Ma Y, Zhang Q, Zhou Q, Song Y, et al. Structural Basis for Apelin Control of the Human Apelin Receptor. Structure. 2017 Jun 6;25(6):858-866.e4.

7. Zhen EY, Higgs RE, Gutierrez JA. Pyroglutamyl apelin-13 identified as the major apelin isoform in human plasma. Anal Biochem. 2013 Nov;442(1):1–9.

8. Zhong JC, Zhang ZZ, Wang W, McKinnie SMK, Vederas JC, Oudit GY. Targeting the apelin pathway as a novel therapeutic approach for cardiovascular diseases. Biochim Biophys Acta BBA - Mol Basis Dis. 2017 Aug;1863(8):1942–50.

9. Atwood BK, Lopez J, Wager-Miller J, Mackie K, Straiker A. Expression of G protein-coupled receptors and related proteins in HEK293, AtT20, BV2, and N18 cell lines as revealed by microarray analysis. BMC Genomics. 2011 Jan 7;12.

10. Lee KS, Navaluna E, Marsh NM, Janezic EM, Hague C. Development of a Novel SNAP-Epitope Tag/Near-Infrared Imaging Assay to Quantify G Protein-Coupled Receptor Degradation in Human Cells. SLAS Discov Adv Sci Drug Discov. 2021;26(4):570–8.

11. Pope GR, Tilve S, McArdle CA, Lolait SJ, O'Carroll AM. Agonist-induced internalization and desensitization of the apelin receptor. Mol Cell Endocrinol. 2016;437:108–19.

12. Liao Y, Wang J, Jaehnig EJ, Shi Z, Zhang B. WebGestalt 2019: gene set analysis toolkit with revamped UIs and APIs. Nucleic Acids Res. 2019 Jul 2;47(W1):W199–205.

13. Thibeault PE, Ramachandran R. Role of the Helix-8 and C-Terminal Tail in Regulating Proteinase Activated Receptor 2 Signaling. ACS Pharmacol Transl Sci. 2020 Oct 9;3(5):868–82.

14. Tian Y, Chen R, Jiang Y, Bai B, Yang T, Liu H. The Protective Effects and Mechanisms of Apelin/APJ System on Ischemic Stroke: A Promising Therapeutic Target. Front Neurol. 2020 Mar 3;11:75.

15. Kee TR, Khan SA, Neidhart MB, Masters BM, Zhao VK, Kim YK, et al. The multifaceted functions of β-arrestins and their therapeutic potential in neurodegenerative diseases. Exp Mol Med. 2024 Jan 11;56(1):129–41.

16. Moriya H. Quantitative nature of overexpression experiments. Cohen-Fix O, editor. Mol Biol Cell. 2015 Nov 5;26(22):3932–9.

17. Bolognesi B, Lehner B. Reaching the limit. eLife. 2018 Aug 10;7:e39804.

18. Dong X, Wang C, Zhang J, Wang S, Li H, Kang Y, et al. Cholecystokinin Expression in the Development of Postinfarction Heart Failure. Cell Physiol Biochem. 2017;43(6):2479–88.

19. Welsh P, Murray HM, Ford I, Trompet S, De Craen AJM, Jukema JW, et al. Circulating Interleukin-10 and Risk of Cardiovascular Events: A Prospective Study in the Elderly at Risk. Arterioscler Thromb Vasc Biol. 2011 Oct;31(10):2338–44.

20. Xu S, Zhang J, Liu J, Ye J, Xu Y, Wang Z, et al. The role of interleukin-10 family members in cardiovascular diseases. Int Immunopharmacol. 2021 May;94:107475.

21. Ritterhoff J, Young S, Villet O, Shao D, Neto FC, Bettcher LF, et al. Metabolic Remodeling Promotes Cardiac Hypertrophy by Directing Glucose to Aspartate Biosynthesis. Circ Res. 2020 Jan 17;126(2):182–96.

22. He X, Yang T, Lu YW, Wu G, Dai G, Ma Q, et al. The long noncoding RNA CARDINAL attenuates cardiac hypertrophy by modulating protein translation. J Clin Invest. 2024 Jul 1;134(13):e169112.

23. Li C, Cheng H, Adhikari BK, Wang S, Yang N, Liu W, et al. The Role of Apelin–APJ System in Diabetes and Obesity. Front Endocrinol. 2022 Mar 9;13:820002.

24. Castan-Laurell I, Masri B, Valet P. The apelin/APJ system as a therapeutic target in metabolic diseases. Expert Opin Ther Targets. 2019 Mar 4;23(3):215–25.

25. Tsai TH, Chen E, Li L, Saha P, Lee HJ, Huang LS, et al. The constitutive lipid droplet protein PLIN2 regulates autophagy in liver. Autophagy. 2017 Jul 3;13(7):1130–44.

26. Zeiger W, Ito D, Swetlik C, Oh-hora M, Villereal ML, Thinakaran G. Stanniocalcin 2 Is a Negative Modulator of Store-Operated Calcium Entry. Mol Cell Biol. 2011 Sep 1;31(18):3710–22.

27. Kamal MV, Damerla RR, Dikhit PS, Kumar NA. Prostaglandin-endoperoxide synthase 2 (PTGS2) gene expression and its association with genes regulating the VEGF signaling pathway in head and neck squamous cell carcinoma. J Oral Biol Craniofacial Res. 2023 Sep;13(5):567–74.

28. Kehat I, Molkentin JD. Molecular Pathways Underlying Cardiac Remodeling During Pathophysiological Stimulation. Circulation. 2010 Dec 21;122(25):2727–35.

29. Xiao Z, Kong B, Yang H, Dai C, Fang J, Qin T, et al. Key Player in Cardiac Hypertrophy, Emphasizing the Role of Toll-Like Receptor 4. Front Cardiovasc Med. 2020 Nov 26;7:579036.

30. Ahuja P, Sdek P, MacLellan WR. Cardiac Myocyte Cell Cycle Control in Development, Disease, and Regeneration. Physiol Rev. 2007 Apr;87(2):521–44.

31. Ichiki T. Role of cAMP Response Element Binding Protein in Cardiovascular Remodeling: Good, Bad, or Both? Arterioscler Thromb Vasc Biol. 2006 Mar;26(3):449–55.

32. Cuadrado A, Rojo AI, Wells G, Hayes JD, Cousin SP, Rumsey WL, et al. Therapeutic targeting of the NRF2 and KEAP1 partnership in chronic diseases. Nat Rev Drug Discov. 2019 Apr;18(4):295–317.

33. Perea-Gil I, Seeger T, Bruyneel AAN, Termglinchan V, Monte E, Lim EW, et al. Serine biosynthesis as a novel therapeutic target for dilated cardiomyopathy. Eur Heart J. 2022 Sep 21;43(36):3477–89.

Chapter 5: Developing a Method to Screen Compounds Against GPCR Targets

5.1 Introduction

5.1.1 The challenges of targeting GPCRs in drug discovery

G protein-coupled receptors are a privileged protein class with an extensive history of successful therapeutics approved modulating their activity despite their inherent challenges as a druggable target. In fact, approximately 30 – 40% of all approved small molecule drugs target just 165 of the 800 potential GPCRs encoded in the human genome (1,2). Of these 800 GPCRs, half are non-therapeutic olfactory receptors (3,4). Subtracting the 165 GPCRs with existing therapeutics leaves ~ 200 potentially druggable GPCRs without an existing drug treatment option, highlighting the immense potential that drugging novel GPCRs still holds. With the depletion of rational-design and natural-product inspired therapeutics, GPCR drug discovery is left with an unexplored and difficult path towards novel therapeutic compounds (5–7). As membrane-bound receptors, GPCRs present challenges in drug discovery due to issues with the measurement of activity, expression, and proper folding. As the field of drug discovery evolves and the need to explore novel GPCR therapeutics increases, capabilities in drug discovery need to be expanded to meet this rising need.

Common approaches to GPCR drug discovery navigate around issues with activity measurement and proper protein expression and folding. Each of these approaches are met with hurdles and researchers frequently make experimental sacrifices to achieve results by running low-throughput screens or introducing non-physiological receptor mutations to increase GPCR stability outside of its native environment. The most traditional approach to identify compounds targeting GPCRs are cellular activity assays, which directly measure downstream signaling

markers and inform on compound agonism and antagonism. This type of testing is the most informative but is labor intensive and cannot be performed at exceptionally high-throughput levels. Additionally, when examining GPCR activity, results can be convoluted as there is no "one-size fits all" assay that reports on all GPCRs' activation. GPCRs are heterotrimeric G proteins composed of three distinct subunits (α, β, and γ) that are functionally classified depending on their associated Gα subunit; of which there are four families, each family leading to the activation of a distinct signaling pathway (8). To make matters more complex, many GPCRs are associated with multiple Gα subunit families, meaning that activation with two different agonists on the same GPCR may lead to two very different physiological responses, and two very different results via activity measurement. It is also important to note that following agonist activation of a GPCR, GDP bound to Gα on the intracellular side is exchanged with GTP, leading to dissociation of the Gα subunit from the membrane-bound Gβγ dimer, thus generating two functional units that can signal to various cellular pathways (8,9). Taken together, while assessing the functional impact of compound-GPCR engagement is important and informative, the labor required for this type of experimentation introduces variation that makes screening large numbers of compounds and ranking them difficult.

More modern drug discovery approaches focus on identifying compound-GPCR interactions, but these methods rely on soluble and properly folded protein. Protein-ligand interaction assays like radioligand studies, use recombinant protein to identify compounds that target GPCRs. This type of experimentation removes the complex signaling component of GPCR activation yet introduces the separate challenge of expressing and purifying the GPCR target protein. There is no universal strategy for recombinant expression of functional GPCRs, so optimization is unique to each protein. Different expression systems, such as bacteria, insect

cells, yeast, and mammalian cells have been utilized over the past few decades, with growing interest in the use of mammalian cell lines due to less post-translational modifications and a higher percentage of functional, membrane-inserted GPCRs (10–13). Purifying functional recombinant GPCRs away from their native bilayer can be divided into two processes – extraction of the GPCR from the membrane and purification. Experimental conditions must be optimized to maintain the active state of the GPCR. In most cases, different detergents are used, with mild non-ionic surfactants supplemented with stabilizing agents traditionally being the most successful (11,12). Unfortunately, many GPCRs are still not stable when in a detergent solution due to their structural flexibility and multiple differing conformational states (11). The need to keep the GPCR in its correctly folded state limits how aggressive purification can be; hence a simple column protein purification likely will not yield desirable protein, as the GPCR will most likely unfold. While protein-ligand interaction assays facilitate more direct measurement of ligand interaction and even high-throughput screening (HTS), expression and purification of properly folded GPCRs remains an incredibly high barrier of entry for these assays and has prevented active study of many of the under investigated GPCRs.

The inherent variability and difficulty in assays used for studying GPCR activity, juxtaposed with the need for properly folded purified recombinant protein in ligand interaction studies, underscores why GPCRs are notoriously difficult targets for conventional drug discovery approaches. These challenges necessitate innovative assay designs and screening strategies that can accommodate the unique structural and functional demands of GPCRs.

5.1.2 The theory behind the utilization of virus-like particles as a GPCR screening model

Virus-like particles (VLPs) have recently gained attention for their use as a vaccination modality to deliver antigens efficiently, but the application of VLPs has expanded over the years with extensive efforts focused on using VLPs for different functions in medicine such as gene therapy and diagnostics (14). VLPs are virus-derived structures made up of multiple subunits with the ability to self-assemble (15,16). VLPs maintain the correct form and size of a virus, while lacking the genetic material required to replicate and infect a host cell (16). HIV-1 virus assembly and release is driven by the viral Gag protein (17). The Gag protein oligomerizes into a spherical protein shell that ultimately results in budding and release from the cell surface, using the plasma membrane as a lipid envelope (17,18). Since the Gag protein utilizes the plasma membrane as a vesicular wrapper, we hypothesized that co-overexpression of a GPCR on the plasma membrane in addition to the Gag polyprotein would result in correctly folded GPCR that could be used for drug screening purposes (**Figure 5.1**) and bypass all the issues associated with separating the GPCR from its native bilayer.

VLPs are not completely novel in the GPCR space. In 2016, Ho et al. utilized VLPs to screen hundreds of GPCR protein variants to select the ideal construct for increased protein yield and stability (19). Additionally, the use of VLPs in isolating target GPCR-specific antibodies has increased due to the fact VLPs are more stable to handle than intact GPCR-expressing cells (20). Based on the previous work accomplished with VLPs, we believe a reliable method can be developed to utilize VLP formation to capture GPCRs in their native state without the traditional requirements for protein modifications or extreme buffer conditions. Though the VLPs do not contain the necessary cellular machinery to execute functional analyses, VLPs present an easy

and low-barrier access point to produce properly folded GPCRs while satisfying the standard buffer requirements for many protein-ligand assays.

Affinity selection mass spectrometry has become an indispensable technique in the high-throughput drug discovery process and has evolved to accommodate a broad range of modalities and protein targets. The ASMS workflow is characterized by several key steps designed to precisely identify compounds that exhibit specific interactions with the protein target of interest. The assay workflow begins with the incubation of a target protein with a library of compounds, optimized to promote specific interactions between the protein of interest and potential ligands. This is followed by a wash step to remove compounds that do not interact with the target protein, leaving only ligands that have formed specific binding interactions with the protein of interest. The remaining compounds are then collected, and mass spectrometry analysis is used to assign their identities (**Figure 5.2**).

While ASMS has seen a recent expansion of applications and methodologies, ASMS in terms of GPCR screening remains largely unexplored due to proper protein folding difficulties. Additionally, the need for buffer conditions to mimic the GPCR native environment is incompatible with mass spectrometry detection methods (21–24). Utilizing VLPs eliminates both problems, providing properly folded protein in a simple buffer condition.

We selected the GPCR, APJ, for our initial studies because of our interest in the signaling and cardioprotective properties of the AS (described in detail in **Chapter 1, Section 1.4.1** and further explored in **Chapter 4**). APJ is a difficult target that is currently being explored in terms of drug design due to its therapeutic potential. APJ represents all the promise but also all the problems associated with GPCRs. APJ and its endogenous ligands represent an incredibly important physiological signaling system imperative to cardiovascular homeostasis, yet it has no

approved drug to date. APJ is difficult to study in terms of functional screening and without mutations, it cannot be reliably extracted from the cell membrane without altering protein folding (25,26). This makes APJ a great test GPCR to study for our uses. Additionally, we included the adenosine A2a receptor (ADORA2A) as it is a well-studied GPCR that can be utilized as a control and benchmark for other techniques. In terms of GPCRs, ADORA2A represents a validated drug target that is better understood and more tractable. The two GPCRs, APJ and ADORA2A, provide divergent yet easily accessible test cases for experimental evaluation.

The structural and functional complexity of GPCRs present significant challenges which necessitate innovative approaches like ASMS to increase the speed of developing drugs that target GPCRs. In this work, we hypothesized that VLPs represent a portable and tunable system for maintaining GPCR structural stability and folding and can be utilized in conjunction with ASMS-based HTS for determining target engagement with GPCRs. The generation of GPCR-VLPs avoids the complexities that come with having to purify GPCRs from their native bilayer and expands the current capabilities of ASMS with correctly folded GPCRs in simple buffer systems.

5.1.3 Research strategy

In this chapter, we discuss the development of a reliable and reproducible method for generating and purifying GPCR-VLPs in HEK293T cells. We chose these cells because they are easy to use and typically lead to large yields of recombinant proteins. We demonstrate ligand specificity and selectivity with two different GPCR systems, APJ and ADORA2A, utilized as test and reference GPCR systems, respectively. Before using a GPCR-VLP platform we attempted to purify and maintain correctly folded APJ through removal from the native bilayer. **Appendix I** expands on the various techniques attempted to extract APJ in its native folded state.

Additionally, this appendix goes into detail about some of the important lessons learned from VLP purification attempts as well as important experiments that helped shape the ASMS binding assay protocol. We will begin this chapter by discussing the generation and purification of GPCR containing VLPs as well as confirm that purified samples contain vesicles of the correct size and morphology as native VLPs. We will then show evidence of VLP formation with electron microscopy micrographs. This chapter is concluded by discussing experiments performed to demonstrate positive control binding enrichment utilizing both simple and complex experimental conditions. We believe GPCR-VLP generation is a first step to developing a universal system to screen peptides or small molecules against GPCRs. In terms of APJ screening, we believe this method will allow for the screening of compounds with desirable drug-like properties, including a longer half-life and stability, compared to APJ's endogenous ligands, apelin and elabela.

5.2 Materials and Methods

5.2.1 Materials

HEK293T cells and DMEM media were purchased through ATCC (Manassas, VA). The APJ plasmid was obtained from Origene (Rockville, MD), while the ORF of ADORA2A was purchased from Twist Bioscience (South San Francisco, CA). The pSNAPf vector, SNAP substrate, and SNAP-Capture Magnetic Beads were obtained from New England Biolabs (Ipswich, MA). The HIV-1 Gag-mCherry plasmid was purchased from Addgene (Watertown, MA). Stellar competent cells and the In-Fusion HD Cloning Kit were obtained from Takara Bio (San Jose, CA), while the HiSpeed Plasmid Maxi Kit was purchased from QIAGEN (Germantown, MD). Eurofins Genomics (Seattle, WA) validated all plasmid sequences. FBS, Opti-MEM media, lipofectamine 3000, PBS, formaldehyde, dithiothreitol, XCell SureLock Mini-Cell Electrophoresis system, PageRuler Plus Prestained Protein Ladder, NuPAGE 4-12%

Bis-Tris gels, MOPS SDS Running Buffer, SimplyBlue SafeStain, iBlot Transfer System, nitrocellulose transfer stacks, Tween 20, and salt guanidine hydrochloride were all purchased from Thermo Fisher Scientific (Waltham, MA). Heparin was obtained from TRC (Manchester, NH). An APJ antibody was purchased through Proteintech (Rosemont, IL), while the secondary antibody was bought from LI-COR (Lincoln, NE). The small volume protein assay was purchased from Bio-Rad Laboratories (Hercules, CA). Pyroglutamyl-apelin-13 and adenosine were purchased from Cayman Chemical (Ann Arbor, MI). Columns were obtained from Waters (Columbus, MS). Bovine serum albumin (BSA) and peptide synthesis solvents were purchased from Sigma Aldrich (Burlington, MA). Chromatography solvents were obtained from Fisher Scientific (Hampton, NH). Quantfoil R 2/2 300-mesh copper grids, carbon support film 200-mesh copper grids, Whatman filter paper, and Dumont Tweezers were purchased from Electron Microscopy Sciences (Hatfield, PA). Nano-W dye was purchased from Nanoprobes (Yaphank, NY).

5.2.2 Development and purification of SNAP-GPCR plasmids

The development of the SNAP-APJ was described in detail in **Chapter 4, Section 4.2.3**. The ORF of ADORA2A was ordered and subcloned into the pSNAPf vector using the same method. The HIV-1 Gag-mCherry plasmid was purchased through Addgene (Plasmid # 85390) (27). All plasmids were transformed into Stellar competent cells (#636766) and purified using QIAGEN's HiSpeed Plasmid Maxi Kit (#12662) following the manufacturer's protocol. All plasmid sequences were validated though Eurofins Genomics (Seattle, WA).

5.2.3 VLP generation

VLPs were generated by following three distinct steps (**Figure 5.3**) that are described in detail below: transfection (**5.2.3.A**), collection (**5.2.3.B**), and purification (**5.2.3.C**).

5.2.3.A Transfection

HEK293T cells (ATCC, #CRL-3216) were maintained in DMEM supplemented with 4% v/v FBS for at least one week before beginning the process of VLP generation, with passaging as necessary, to ensure cells were acclimated to culture conditions. Cells were kept in a humidified incubator at 37ºC with 5% CO_2. A reverse transfection protocol was applied, using the Lipofectamine 3000 Transfection Reagent (#L3000001). Two separate solutions were created: one containing lipofectamine 3000, and the other a mixture of DNA and P3000 reagent (**Figure 5.4A**). DNA concentrations were added in a 1:3 GPCR:Gag ratio due to observed optimal increases in both GPCR and Gag protein expression to get a total of 25 µg DNA per T175 flask. The two solutions were then mixed well and combined in a 1:1 ratio to get a DNA-lipid complex. This DNA-lipid complex was incubated at room temperature for at least 20 min, while HEK293T cells were passaged and counted (**Figure 5.4B**). The DNA-lipid complex was then combined with complete media containing 12 million cells to a T175 flask (**Figure 5.4C**). The DNA-lipid complex constituted 10% of the total volume.

5.2.3.B Collection

The collection schematic can be viewed in **Figure 5.3B**. After 18h of initiating the transfection, the media containing the transfection mixture was aspirated and replaced with fresh complete media supplemented with 10 µg/mL heparin (TRC, #H245800). The first step for VLP binding to host cells occurs when VLPs interact with heparan sulfate, thus the addition of heparin inhibits this process and results in increased VLP concentrations in the supernatant (28). Media was then collected and replenished at 48h, 72h, and 96h post-transfection after which the cells were discarded. After each collection, the media was centrifuged at 300 x g for 5 min to remove cell debris and the supernatant was stored at 4°C until all media collections were complete.

5.2.3.C Purification

The purification schematic can be viewed in **Figure 5.3C**. Following the 96h collection and 300 x g centrifugation step, samples were pooled and centrifuged at 2,000 x g for 20 min to eliminate extra protein contaminants. The supernatants were then transferred into ultracentrifuge tubes without disrupting the pellets. The samples were ultracentrifuged using a Beckman Type 45 Ti Fixed-Angle Rotor at 16,000 RPM for 2h at 4°C. The supernatant was carefully decanted and the pellets containing the VLPs were gently resuspended in PBS and centrifuged in the microcentrifuge at 16,000 RPM for 45 min. The supernatant was again discarded and the pellet containing the VLPs was gently resuspended in PBS to get the desired final concentration.

5.2.4 Validation of protein expression by imaging and western blotting

For imaging purposes, the HEK293T cells underwent a scaled down transfection in a 12-well plate. Cells were fixed using 4% methanol-free formaldehyde as described in **Chapter 3, Section 3.2.4**, but instead of using the described stains, GPCR expression was validated with the cell impermeable SNAP-Surface Alexa Fluor 488 (#S9129S), while Gag was visualized through the mCherry tag. Images were captured on an EVOS M7000 Microscope at 10X. Images then underwent background subtraction and channel merging using ImageJ 1.8.0. Western blotting was accomplished utilizing the protocol described in **Chapter 3, Section 3.2.5** and the primary rabbit anti-APJ antibody (Proteintech, #20341-1-AP) at a 1:1000 dilution. Coomassie staining was accomplished with the SimplyBlue SafeStain (#LC6060).

5.2.5 Negative-Stain Electron Microscopy sample preparation and data collection

VLP samples prepared for electron microscopy (EM) underwent the same generation and purification procedure with the slight modification of excluding the supplemented heparin from

the HEK293T media. 200-mesh Carbon Copper grids (#CF200-Cu-50) for negative-stain electron microscopy (ns-EM) were glow discharged for 30s before a 3.5 µL sample aliquot was applied to the grid and allowed to absorb at room temperature for 1 min. Grids were then blotted with Whatman filter paper and immediately dipped into Nano-W dye (#2018-5mL). Grids were stained for 30s at room temperature, then blotted to dryness and stored for downstream data acquisition.

Grids were imaged using a 120 kV FEI Technai G2 Spirit TEM with a Gatan Ultrascan 4000 CCD. Micrographs were collected using Leginon at a magnification of 67000X corresponding to a pixel size of 1.60 Å per pixel. The final micrographs were low pass-filtered and contrast-enhanced in ImageJ 1.8.0 for visualization.

5.2.6 Cryo-EM sample preparation and data collection

To make grids for cryogenic electron microscopy (cryo-EM), Quantifoil R 2/2, 300-mesh carbon grids (#Q3100CR2) were glow discharged for 30s. A 3.5 µL aliquot of VLP sample was applied to the grid and allowed to adsorb on the grid for 10s inside a humidity-controlled chamber to avoid evaporation. The grids were then immediately frozen in liquid ethane using a Vitrobot Mark IV at 4 °C and 100% humidity with 3.5s blotting.

Frozen grids were imaged using a 200 kV Glacios Cryo-TEM with a Gatan K3 direct electron detector. Micrographs were collected in article counting mode at a magnification of 22000X, corresponding to a pixel size of 1.38 Å per pixel. Image frames were corrected for electron beam-induced motion using Motioncor2. The final micrographs were binned, low pass-filtered, and contrast-enhanced in ImageJ 1.8.0 for visualization.

5.2.7 Peptide pulldown assay

5.2.7.A Protein loading

Following purification, each VLP sample batch was protein normalized using a small volume protein assay (Bio-Rad Laboratories, #500012). Protein normalized VLP samples were loaded onto 40 µL equilibrated SNAP-Capture Magnetic Beads (New England Biolabs, #S9145S) in a low protein binding microcentrifuge tube and allowed to equilibrate on a rotating tube mixer for at least 1h at 4°C. The amount of protein loaded per experiment was adjusted depending on batch yield and necessary agonist signal on the mass spectrometer but fell in the range of 2.75 – 5.5 µg total protein, with a higher protein content leading to a better MS (mass spectrometry) signal. Following magnetic bead-VLP incubation, the samples were captured via magnet and washed three times with 500 µL blocking buffer containing 0.1% w/v BSA and 0.05% v/v Tween 20 in PBS.

5.2.7.B Binder incubation

Blocked magnetic bead-VLP samples were then incubated with each respective test condition. All test solutions were made in blocking buffer, and each 100 µL incubation consisted of 1 µM known binding partner with equivalent concentrations of the test compounds. These incubations were set up to undergo light agitation on the rotating tube mixer for 1h at 4°C. Once the 1h incubation was complete, samples were immediately washed three times as quickly as possible with 200 µL of ice-cold PBS. Then samples were eluted twice with 25 µL of 3 M guanidine hydrochloride while undergoing constant agitation with finger flicking.

5.2.8 High-performance liquid chromatography - mass spectrometry

Eluted samples were either immediately chilled to 8°C in a Waters UPLC M-class autosampler or stored for up to 24h at 4°C before analysis. A 60°C heated Waters BEH C18 Column, 130Å, 2.5 µm, 2.1 mm X 50 mm (Waters, #186006029) was utilized for apelin separation, while adenosine separation was achieved using an InfinityLab Poroshell 120 HILIC, 2.1 x 150 mm, 4 µm. Optima water with 0.1% formic acid and acetonitrile with 0.1% formic acid made up Buffers A and B, respectively. Apelin separation was achieved with a standard gradient of 0-100% B buffer over 15 min, while an isocratic gradient of 100% B buffer was used to separate adenosine. MS data was collected and peak integration was performed using either a Waters Xevo TQ-S-2 with MassLynx 4.1 or a Thermo Fisher Orbitrap Ascend Tribrid with Xcalibur V4.1.

Compound retention was quantified using mass spectra. Multiple reaction monitoring (MRM) methods were built on the Waters Xevo for both adenosine and pyr-AP-13 that standardized fragments and transitions. These MRM methods were ideal for these initial experiments since they offered increased sensitivity and dynamic range. Injecting dilution gradients of each compound yielded linear response curves to investigate MS signal response. Data was collected on the ThermoFisher Tribrid Obritrap Ascend for the mock library experiment utilizing the data independent acquisition (DIA) mode for broad mass tracking at the MS^1 level.

To reduce the variability inherent in sample injections, we included an in-house peptide, 8d11, in our quench buffer to serve as an injection control and assist in sample normalization. Cyclic peptide 8d11 has the sequence [dVal][dLeu]A[dAla][dVal]P[dPro]I. It has a mass of 802.5 Da and is known to be well structured and well characterized. It was selected as an internal

standard from a pool of synthetic cyclic peptides for its ability to be retained in both standard C18 chromatography as well as HILIC. 8d11 did not show interaction with either the target protein or our compounds of interest. Assay development and ASMS experimental details can be found here (29).

5.2.9 Synthesis of mock library

More information on the peptide library synthesis can be found in Jonathan Palmer's thesis Chapter 3 (29). Of note, the peptides comprising the mock library were estimated to have a final concentration of 250 nM, so pyr-AP-13 was added accordingly at 250 nM.

5.2.10 Analysis of library incubation with computational calculation of enrichment ratio

Varying from traditional ASMS approaches that require MS^2 data collection, this mock library was designed to have a low mass degeneracy, opening the avenue of uninterrupted primary mass monitoring (29). Peptides that did not have a PAR (peak area ratio) > 0.001 were excluded from analysis due to lack of column retention. Compound enrichment was determined by dividing the PAR for each peptide in the different GPCR-VLP samples by the negative control; then the enrichment factor was calculated by dividing the compound enrichment observed in the APJ-VLPs by the compound enrichment observed in the A2A-VLPs. Further details describing this process can be found in Jonathan Palmer's thesis (29).

5.3 Results

5.3.1 VLP purification

To generate VLPs, we purchased an optimized Gag plasmid with an mCherry tag to visualize the production of VLPs and created SNAP-tagged GPCR plasmids for two different

GPCRs, APJ and ADORA2A. Transfection conditions were optimized to observe increases in both GPCR and Gag protein expression in HEK293T cells (**Figure 5.5A**). Following this validation, we developed a robust purification regimen for VLP collection. During method development, we discovered that media collection from the GPCR-VLP expressing cells followed by a three-centrifugation step procedure yielded the maximum APJ signal as assessed by western blot analysis (**Figure 5.5B**). Additionally, visualization of all proteins in the sample via Coomassie staining yielded molecular weight bands that are similar to the full-length Gag-mCherry. Other Gag cleavage products are expected in both APJ- and ADORA2A-VLPs (**Figure 5.5C**).

5.3.2 Visualization of VLPs

Purified VLP samples appear to contain particles with the correct size and morphology. Following purification, VLP samples underwent ns-EM and cryo-EM. VLPs were likely co-purified with extracellular vesicles, as indicated by ns-EM micrographs containing particles ranging in size from 50-250 nm in diameter (**Figure 5.6A**). Cryo-EM micrographs indicate VLPs form consistent morphologies containing well-ordered Gag and are 50-250 nm in diameter, with an average of 115 nm (**Figure 5.6B**).

5.3.3 Peptide pulldown assays

5.3.3.A Validation of binding-competent protein with GPCR-VLP-ASMS

GPCR plasmids were cloned with an N-terminal SNAP-tag, allowing GPCR proteins to be covalently captured on magnetic beads to provide an insoluble solid support for the GPCR-VLPs. This bead-GPCR-VLP conjugate was subjected to ASMS protocols and compound incubation was optimized for GPCR binding. The presence of binding-competent protein was demonstrated with specific retention of the endogenous positive control pyr-AP-13. Pyr-AP-13

was retained in samples containing APJ-VLPs at a greater level than control VLPs lacking the SNAP-GPCR expression (**Figure 5.7A**). Additionally, APJ-VLPs retained pyr-AP-13 without retaining angiotensin II (AngII), a nonspecific interaction control compound (**Figure 5.7B**). This demonstrates that retention of pyr-AP-13 by APJ-VLPs is specific to the binding interaction between the ligand and APJ and suggests that APJ is present in the VLP folded in a state that favors binding.

5.3.3.B Testing GPCR-VLP-ASMS binding retention with a complex peptide mixture

To validate the APJ-VLP model, we sought to demonstrate specific and significant binding ligand enrichment using a second GPCR as a control. Rather than evaluate enrichment against empty-VLP samples, we selected the GPCR, ADORA2A (A2A) as a nonspecific interaction control for APJ samples. This format provided the added benefit of using the reverse of the system and applying APJ as the control for adenosine-A2A binding (**Figure 5.8A**). Using these experimental conditions and a coincubation with equimolar amounts of adenosine and pyr-AP-13, we were able to demonstrate adenosine-A2A enrichment (**Figure 5.8B**) and pyr-AP-13-APJ enrichment (**Figure 5.8C**) above the threshold of nonspecific interactions.

Encouraged by the retention of co-incubated pyr-AP-13, we further modified the co-incubation conditions to feature pyr-AP-13 and a mock screening library. This mock library was utilized to mimic high throughput screening conditions with random compounds designed to act as noise, allowing further investigation of the nonspecific retention of compounds. Pyr-AP-13 was spiked into a library of 2,688 peptides composed of 13 amino acids at equimolar concentration, giving a final library of 2,689 peptides with one positive control for APJ. Incubation with this library in APJ- and A2A-VLPs rendered significant pyr-AP-13 binding enrichment in APJ-VLPs (**Figure 5.9B**).

5.4 Discussion

5.4.1 Summary of results

In this study we present a novel promising GPCR high throughput screening platform. With this work, we were able to provide the first confirmation that VLPs can be used as a GPCR screening method, thus eliminating the need for a specific buffer or assay condition optimization to support native GPCR folding. The key finding in this study is that with the use of GPCR-VLPs, we can detect enriched binding with positive controls in both simple and complex mixtures of thousands of peptides. This study serves to streamline GPCR drug discovery, as our methodology can be adapted for any GPCR or membrane protein that can be overexpressed *in vitro*.

5.4.2 Robust generation and purification of VLPs

Initially, we began by co-overexpressing a GPCR protein with an HIV-1 Gag protein in order to initiate VLP budding. We utilized HEK293T cells as our model cells for protein production due to their ease of use and large yield of recombinant proteins. Analyses demonstrated that in a co-transfection with SNAP-GPCR and Gag plasmids, both GPCR and Gag were expressed in HEK293T cells (**Figure 5.5A**). Furthermore, following VLP purification, western blot analysis validated APJ expression (**Figure 5.5B**), and Coomassie staining led to observed protein bands at the correct molecular weight of full-length Gag-mCherry (**Figure 5.5C**, band A). Additionally, we noted the predominant protein found in both VLP samples was at the correct molecular weight of a known Gag cleavage product. Gag polyprotein is composed of six different components: matrix protein (MA), capsid protein (CA), spacer peptides 1 (SP1) and 2 (SP2), nucleocapsid protein (NC), and p6 (30). Notably, Gag undergoes cleavage during maturation and while budding off from the cell Gag can leave an outer shell of MA subunits

below the plasma membrane (30,31), which we believe is the predominant protein expressed in our samples (**Figure 5.5C**, band B). Rough calculations with western blot quantification utilizing Image Studio Version 4.0 software estimated that about 25% of total protein in the sample was SNAP-GPCR. Additionally, both ns-EM and cryo-EM corroborate that our purification method resulted in the collection of vesicles that fall within the expected size and morphological range of VLPs (**Figure 5.6**).

5.4.3 GPCR-VLP-ASMS demonstrates binding enrichment with known positive controls in simple peptide solutions

Initial attempts to screen against APJ using ASMS without a VLP platform were met with mixed results. Aggressive inclusion of detergents and other stabilizing agents proved inadequate for keeping APJ in its properly folded state, as evidenced by poor results following ASMS screening. Furthermore, the stabilizing agents used were incompatible with mass spectrometry conditions and mandated difficult sample clean up and loss of analyte. These failures, as outlined in **Appendix I**, led us to adopt the use of VLPs to assist in keeping the GPCRs folded and provide an additional platform for ASMS experimentation.

The use of the SNAP tag on the N-terminus of the GPCRs is crucial for this ASMS experimental workflow in order to capture the targeted VLPs on solid support microbeads allowing for several wash steps. The New England Biolabs SNAP-tag is designed to specifically and rapidly react with benzylguanine derivates, leading to irreversible covalent labeling of the SNAP-tag to any SNAP substrate (32). The utilization of this tag allows an exclusive focus on the targeted SNAP-GPCR-VLPs, thereby providing a cleaner background signal due to minimized non-SNAP-GPCR containing VLP capture.

The initial focus on specific and selective binding enrichment for GPCR-VLP-ASMS was developed around pyr-AP-13 binding to APJ-VLPs. This was selected as our primary test condition for the GPCR-VLP system as APJ represents a complex GPCR that is challenging to maintain in its native folding state when removed from the cell (25,26). HPLC-MS quantification methods were built using a Waters triple quad method specific to APJ's endogenous ligand pyr-AP-13. Quantification was attained with calibration curves and normalized with internal standard peak areas.

Use of the GPCR-VLP-ASMS approach led to significant positive enrichment with pyr-AP-13 in APJ-VLP samples. Initial binding studies demonstrated a 4-fold increase in pyr-AP-13 binding with APJ-VLPs compared to empty-VLPs. Maximal binding was achieved with an ASMS approach using a 60 min incubation time and 1 μM ligand concentration. Additionally, in order to test APJ's binding selectivity, a co-incubation was performed with equal concentrations of pyr-AP-13 and angiotensin II. AngII was selected as a test compound because it's binding partner, the angiotensin AT_1 receptor, is highly homologous with APJ, yet AngII and APJ have no known interaction or binding to their respective receptors (33,34). Observed enrichment of pyr-AP-13 without enrichment of AngII binding to APJ-VLPs (**Figure 5.7B**) evidenced a specific and selective binding interaction between APJ and pyr-AP-13. These findings further support our hypothesis that APJ in VLPs is present in its properly folded state, implied through selective and specific pyr-AP-13 binding enrichment.

5.4.4 GPCR-VLP-ASMS demonstrates binding enrichment with known positive controls in more complex ligand mixtures

Furthermore, we established increased positive control ligand retention utilizing two different GPCR systems, ADORA2A and APJ. ADORA2A- and APJ-VLP samples were protein

normalized and co-incubated with equimolar amounts of adenosine and pyr-AP-13. With this experiment, we demonstrated enriched retention of A2A's native binding partner, adenosine, with A2A-VLP samples (**Figure 5.8B**), and enriched retention of pyr-AP-13 with APJ-VLP samples (**Figure 5.8C**). Both adenosine and pyr-AP-13 were retained in the GPCR-VLP serving as the negative control, suggesting that there is a base level of nonspecific interaction with the surface proteins present within the VLP membrane. Since VLPs introduce a large and hydrophobic surface for ligands to interact with, a baseline level of nonspecific interaction is expected, and unfortunately this increases the difficulty of identifying significant differences in ligand binding enrichment. This is evidenced by the retention of pyr-AP-13 with APJ-VLPs falling below the level of statistical significance. That said, it is worth noting that the typically better understood and better behaved GPCR, A2A, did retain its native binding partner with a greater significance than APJ. It is also possible that the interaction between pyr-AP-13 and APJ is not as robust as the interaction between adenosine and ADORA2A, demonstrated by the worsened ligand-GPCR retention with pyr-AP-13 and APJ-VLPs.

In collaboration with Dr. Jonathan Palmer (29), a mock library was created with 2,688 peptides containing 13 amino acid residues. Mutations within this mock library ensured a variety of properties, like different hydrophobicities, polar surface areas, and masses, substantiating a range of peptides that encompassed the attributes of pyr-AP-13. Before beginning the incubation of the mock library + pyr-AP-13 a similar ionization efficiency was observed for all compounds, verifying that the library members and pyr-AP-13 were present in equimolar concentrations.

Pyr-AP-13 binding enrichment was observed with APJ-VLPs compared to controls when the samples were co-incubated with a mock library consisting of 2,688 other peptides with the same number of amino acids. A2A-VLPs were used as a control for nonspecific interactions of

the mock library + pyr-AP-13 co-incubation, and an enrichment ratio was calculated for each retained test peptide by dividing the enrichment of the peptide in the APJ sample by the enrichment of the peptide in the A2A sample. This analysis facilitated interpretation for specific retention by APJ-VLP samples. In total, we identified 406 masses with some level of retention in APJ-VLP, A2A-VLP, and negative control samples. Enrichment factors spanned from 0.5 to 1.4, with a notable exception at 2.19 for pyr-AP-13 (**Figure 5.9B**), suggesting that pyr-AP-13 was more significantly retained in APJ-VLP samples compared to both A2A-VLP and negative control samples. Interestingly, although the samples were protein normalized, it appears the peptides were typically being retained by APJ-VLP samples at a greater degree than A2A-VLP samples. This could be contributed to the variability of GPCR concentrations within each VLP or the possible instability of APJ compared to A2A, leading to potential increased APJ-VLP lysis during peptide library incubations and several wash steps. Regardless, this bias is likely suppressing the pyr-AP-13 enrichment factor, providing additional confidence in the separation achieved in this experiment. An enrichment ratio cutoff of 2 is typically used to denote a specific versus nonspecific retention (35), exemplifying pyr-AP-13's binding enrichment of 2.19 to APJ-VLPs, compared to the next highest peptide enrichment falling below 1.5. This experiment provided further confidence that our incorporated wash steps were effective in limiting the nonspecific carryover of the other library members into the final eluted MS sample (**Figure 5.9A**). This work demonstrates the feasibility of a library-based high-throughput screen using our GPCR-VLP-ASMS approach.

5.4.5 Limitations of this model system

Despite our best efforts to reduce variability, we acknowledge that this method introduces a high degree of variation. As we cannot separate VLPs that do not contain SNAP-GPCR during

purification, we note that there are likely many VLPs that contain other membrane proteins that are purified in addition to our VLPs of interest. To counter this intrinsic variation in sample collection and purification, we added an additional sample GPCR-VLP that acts as a control for other nonspecific binding to membrane proteins present in the VLP samples. Furthermore, we implemented long incubation times to minimize nonspecific interactions and increase both magnetic bead-VLP association and GPCR-ligand interactions. Future experiments should focus on larger batch VLP generation and purification, as this would increase the VLP yield and potentially further decrease the variability observed in ASMS analysis. As the field of ASMS develops, it is worth tracking broadly applicable advances, like using biolayer interferometry to reduce human sample handling and track protein loading and apply those advances to this technique to reduce error and variability.

Though we set out to demonstrate statistically significant enrichment of GPCR binding partners, it is worth noting that this goal can be at odds with the general application of ASMS. ASMS as a screening tool often consists of single shot experiments, requiring fewer replicates and controls than the experiments detailed here. In general, putative compounds with target engagement identified from ASMS screens will require further testing and validation, and GPCR-VLP-ASMS is no exception. Therefore, we view this GPCR-VLP-ASMS approach as a qualitative step to narrow down a vast chemical space and identify a hit rather than as a quantitative way to provide a definitive answer for GPCR binding and activation. With our pyr-AP-13-mock library screen, we have suggested that our approach is capable of enriching compounds with binding interactions above an identifiable threshold. Though that threshold may not be as strict as traditional ASMS approaches, we believe that we have made great strides in combating some of the challenges posed by using GPCRs in ASMS. Future iterations of this

work should focus on screening random or directed libraries against GPCRs to discover new compounds with target interactions.

5.5 Conclusions

In conclusion, we have developed a novel platform for the HTS of compounds for testing target engagement with GPCRs by enriching GPCR production in VLPs. We demonstrated that we are able to capture GPCR expressing VLPs to solid support beads and observe enriched binding with positive controls in both simple and complex solutions. By presenting the potential of GPCR-VLPs as a screening tool for identifying novel hits, we hope to accelerate and unlock compound screening against GPCRs at a level previously unreachable. The integration of GPCR-VLPs in ASMS will make targeting specific GPCRs quicker and easier and will greatly improve the capability of drug screening today, as well as advance the development of GPCR-targeted therapeutics.

Figures

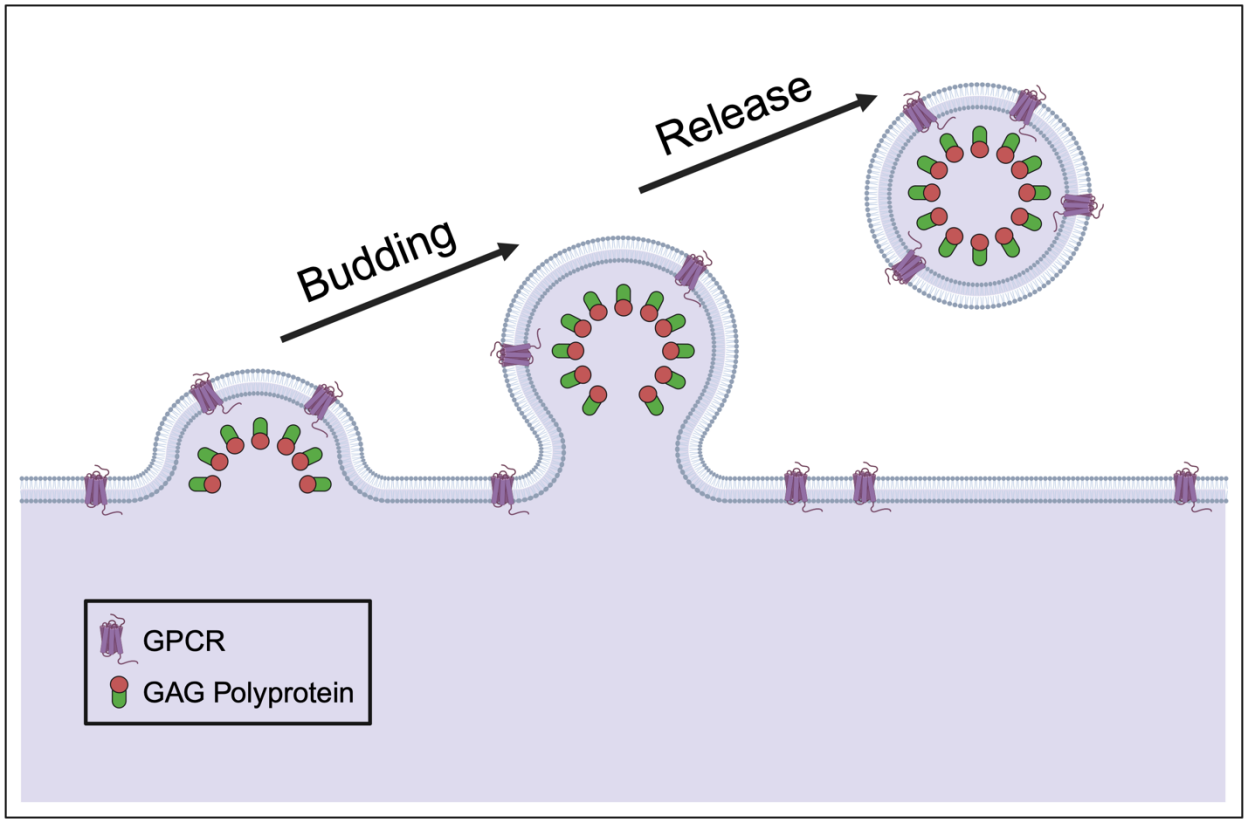

Figure 5.1. Schematic representation of the formation of VLPs.

Recombinant overexpression of a GPCR leads to increased protein on the cell surface, that is then utilized as the VLP lipid envelope following Gag budding and release. Created with BioRender.com

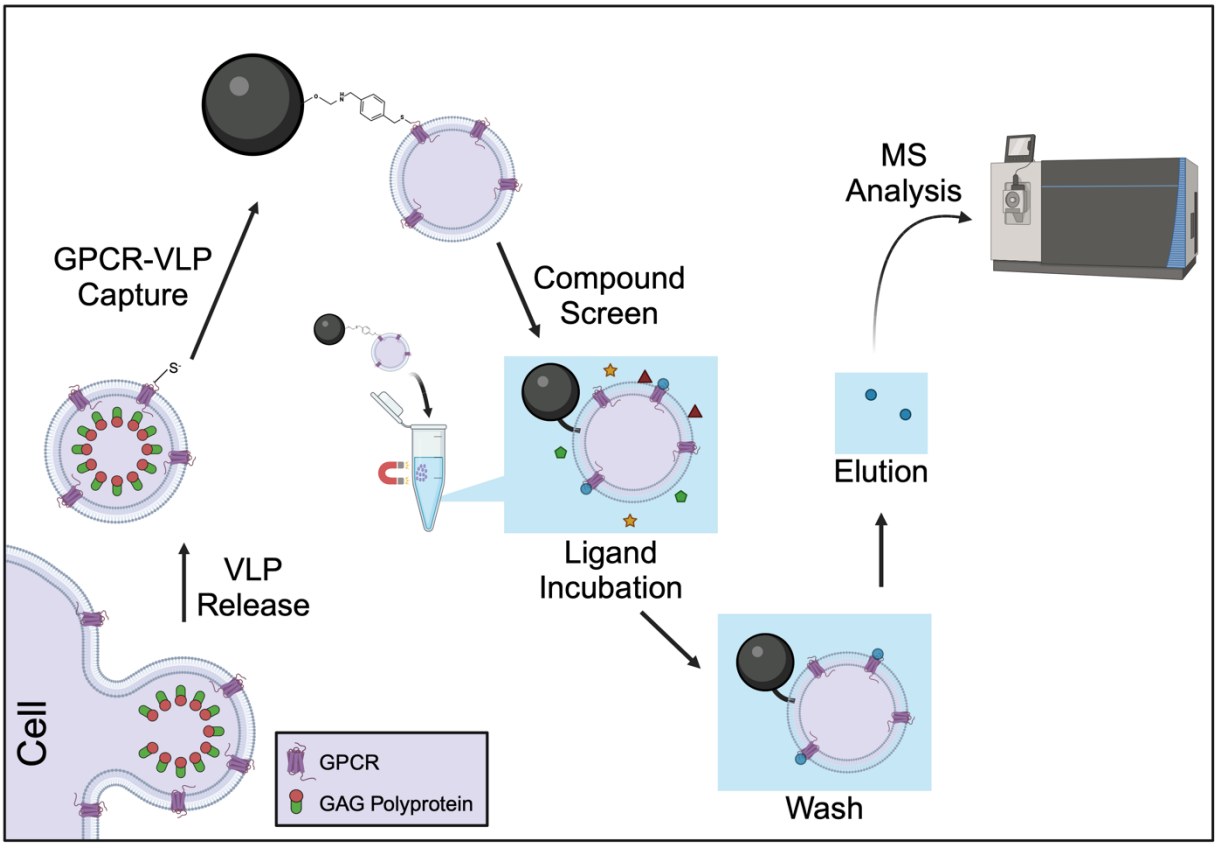

Figure 5.2. Affinity selection mass spectrometry workflow.

First, GPCR containing VLPs are generated and purified. Then the GPCR-VLPs are captured via covalent linkage with insoluble support magnetic beads, and the compound screen is initiated with the ligand incubation. Subsequent wash steps then remove compounds that do not interact with the target protein. Finally, compounds that form a tight binding interaction with the target protein are eluted and undergo mass spectrometry analysis. Created with BioRender.com

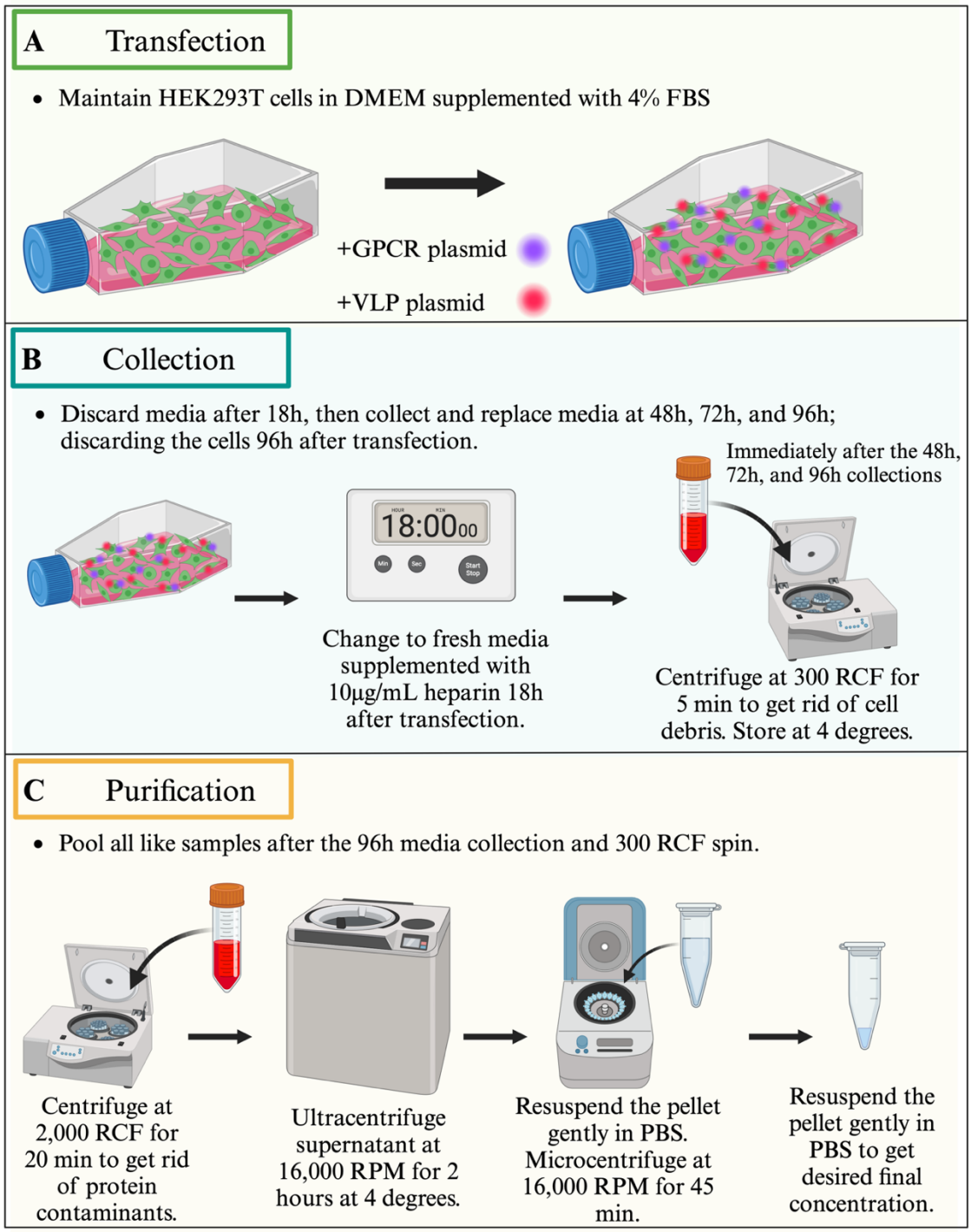

Figure 5.3. Schematic of the different steps for VLP generation.

(**A**) transfection (**B**) collection, and (**C**) purification. Created with BioRender.com

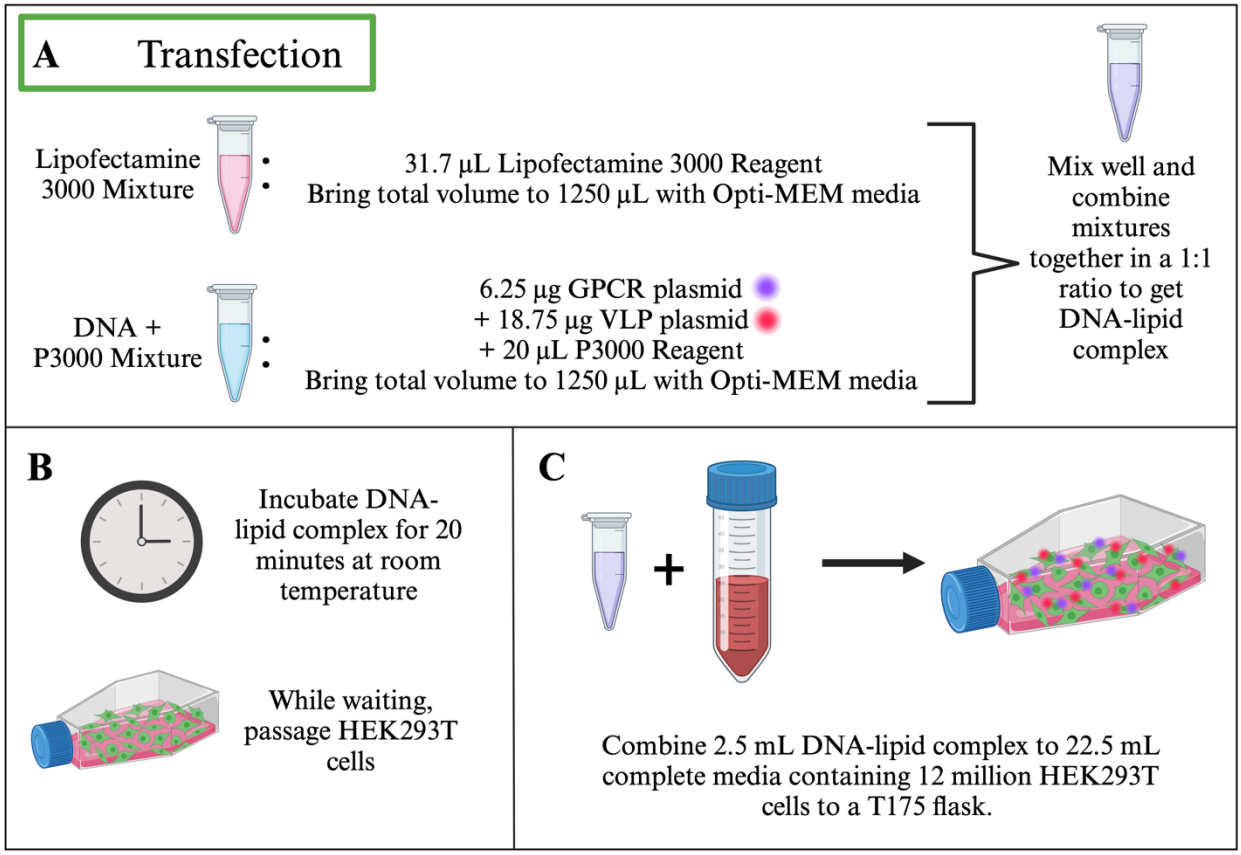

Figure 5.4. Step by step breakdown of the transfection protocol.

(**A**) The transfection reagents are made and combined in a 1:1 v:v ratio. (**B**) While the DNA-lipid complex incubates, begin passaging HEK293T cells. (**C**) Combine 10% volume of the DNA-lipid complex with HEK293T cells and plate in a T175 flask. Created with BioRender.com

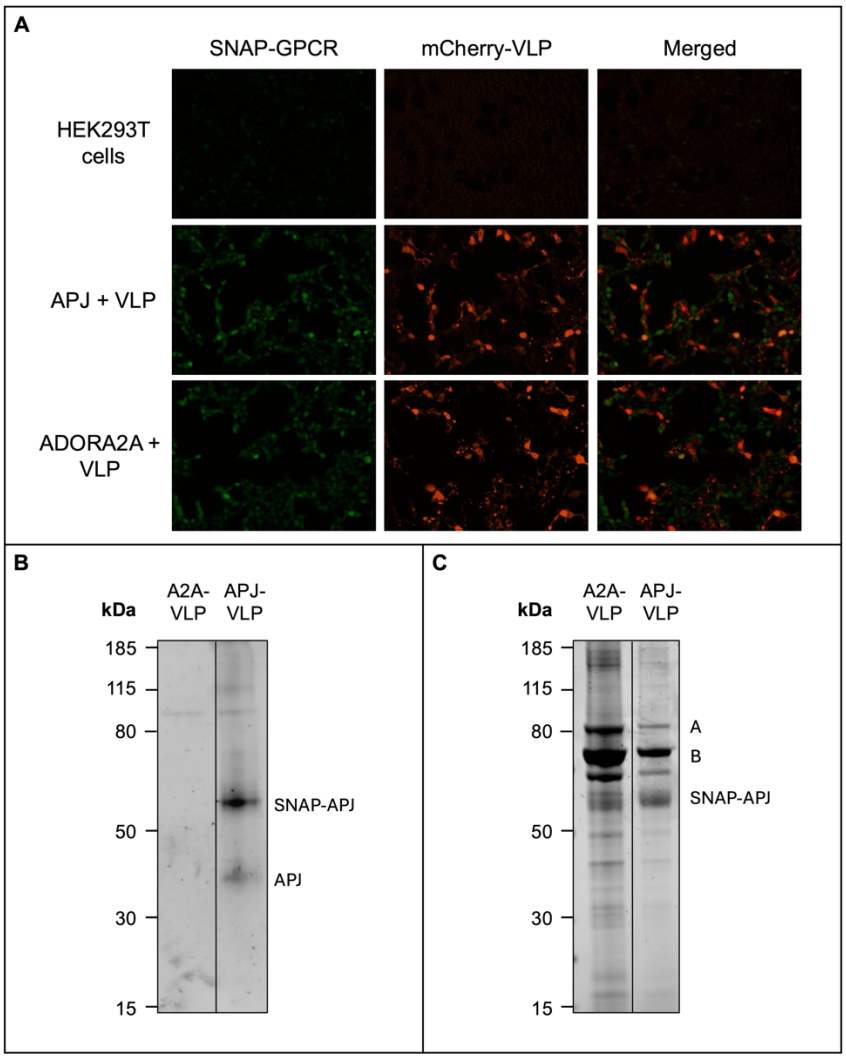

Figure 5.5. Validation of increased GPCR and Gag protein expression.

(**A**) Fluorescent images with SNAP-tag Alexa 488 substrate validating GPCR expression and mCherry validating Gag expression in HEK293T cells. (**B**) Western blot with purified VLP samples and an anti-APJ antibody verifying APJ expression. (**C**) Coomassie staining showing all proteins present following VLP purification. Band A has the same molecular weight as full-length Gag-mCherry (~83kDa), while band B could be a cleavage product of Gag without the matrix (MA) component. SNAP-APJ / SNAP-GPCR migrates at ~62 kDa, while APJ without the SNAP tag is observed at ~43 kDa.

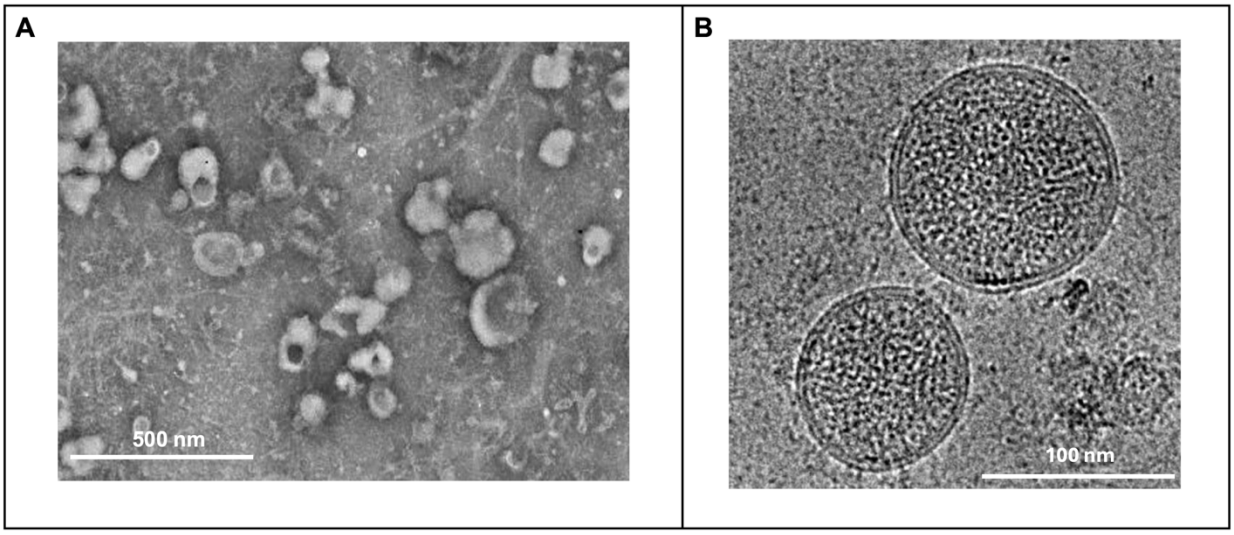

Figure 5.6. Visual confirmation of VLP purity and morphology.

Visualization by (**A**) ns-EM and (**B**) cryo-EM.

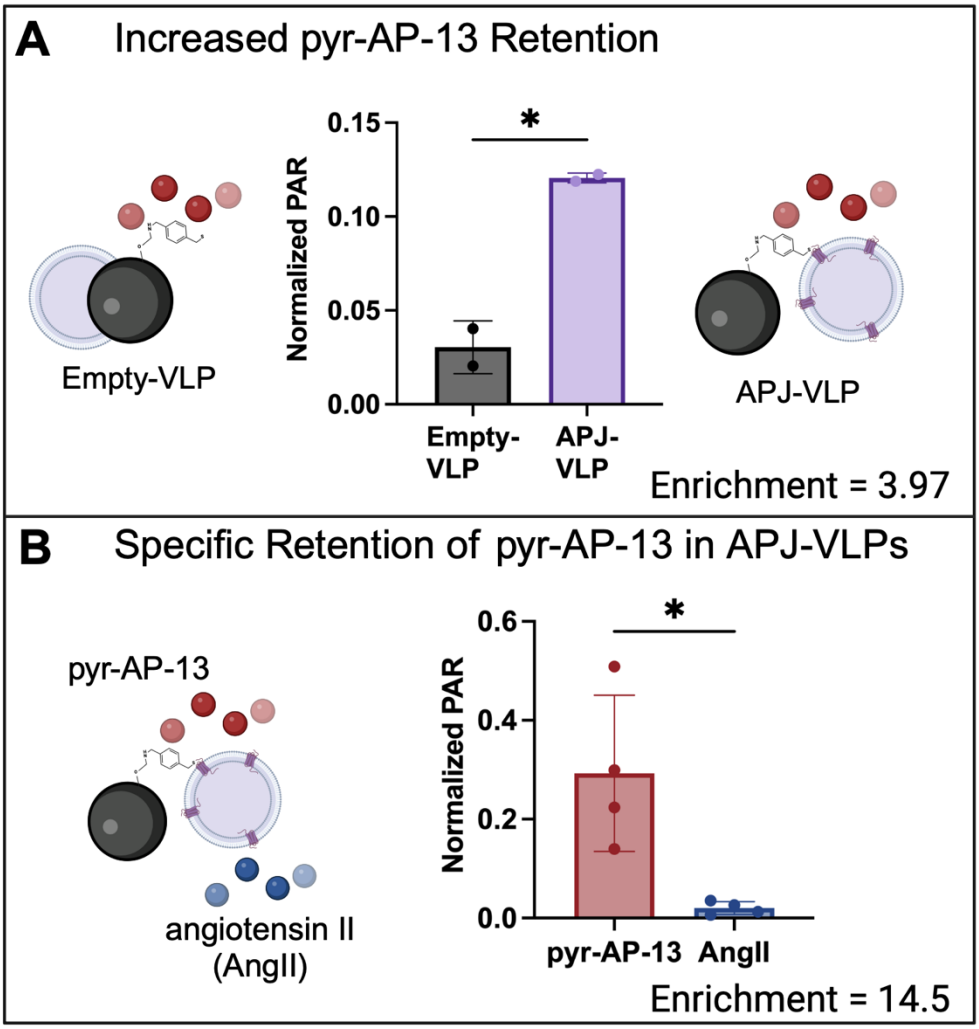

Figure 5.7. GPCR-VLP-ASMS validation of pyr-AP-13 binding.

(**A**) Results from the ligand retention benchmarking test demonstrated an approximate 4-fold enrichment in pyr-AP-13 retention with APJ-VLP samples compared to VLP-negative controls. (**B**) APJ-VLPs specifically bind pyr-AP-13 and not AngII. PAR was normalized to pyr-AP-13 and AngII internal standards, n=4. * $P < 0.05$. Created with BioRender.com

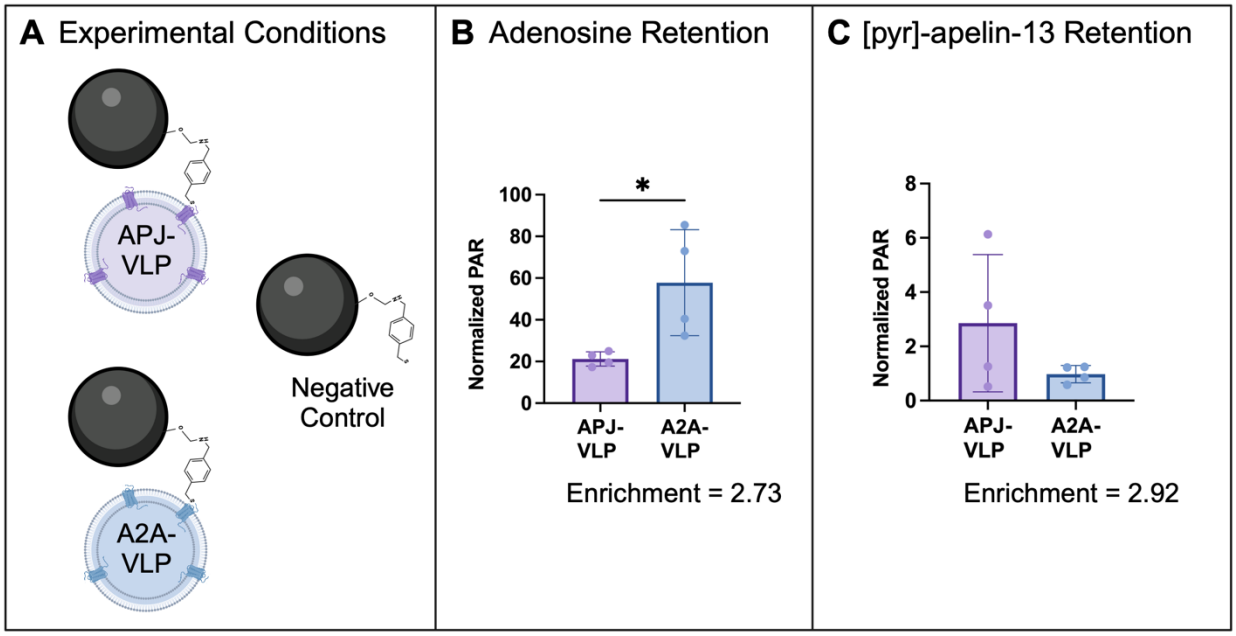

Figure 5.8. Enriched retention of positive control ligands in a two-compound mixture.

(**A**) Schematic of the different experimental conditions utilized. (**B**) Adenosine binding enrichment is observed in A2A-VLPs and (**C**) pyr-AP-13 binding enrichment is observed in APJ-VLPs when ligands are co-incubated. PAR was normalized to adenosine and pyr-AP-13 retention in negative control samples, n=4. * $P < 0.05$ Created with BioRender.com

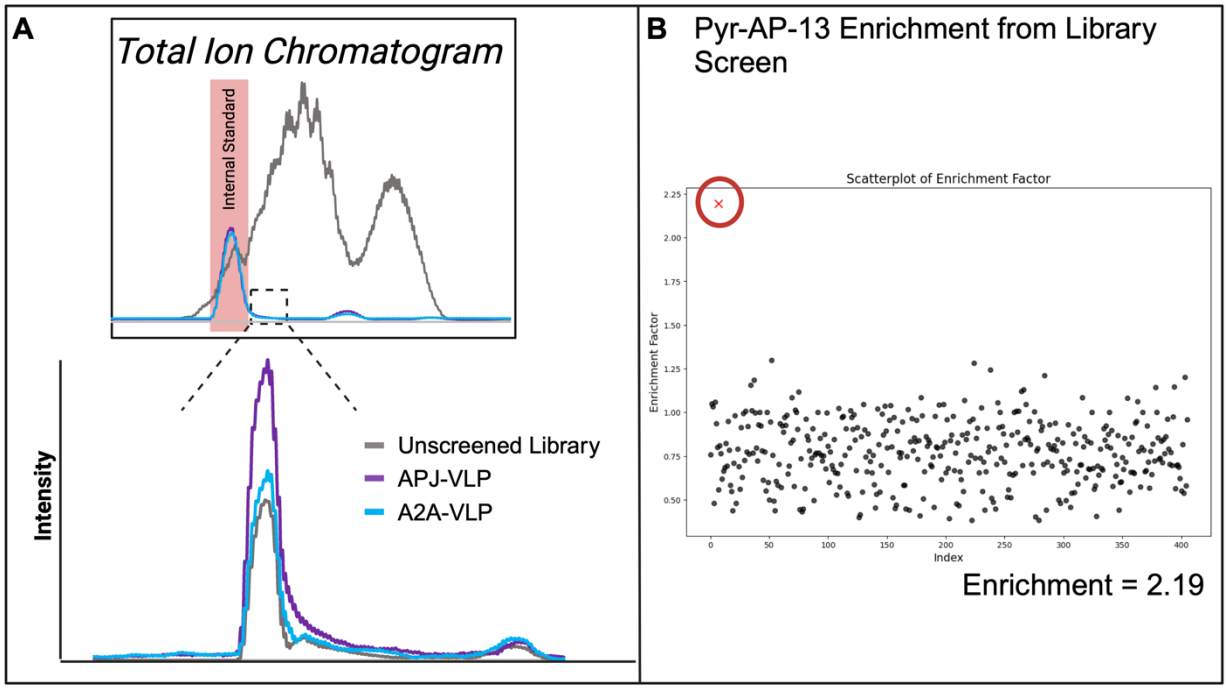

Figure 5.9. Enriched retention of pyr-AP-13 with APJ-VLPs when co-incubated with a complex mixture with over 2,500 peptides.

(**A**) Total ion chromatogram demonstrating wash steps sufficiently eliminate the background from the unscreened library. Comparison of the library chromatograms from the different samples compare the retention capability of either all peptides (total ions) or pyr-AP-13 (extracted ion). (**B**) Enrichment of pyr-AP-13 from a mock library of similarly sized peptides. Results of the library screening show pyr-AP-13 enrichment versus the mock library.

References

1. Santos R, Ursu O, Gaulton A, Bento AP, Donadi RS, Bologa CG, et al. A comprehensive map of molecular drug targets. Nat Rev Drug Discov. 2017 Jan;16(1):19–34.

2. Sriram K, Insel PA. G Protein-Coupled Receptors as Targets for Approved Drugs: How Many Targets and How Many Drugs? Mol Pharmacol. 2018 Apr;93(4):251–8.

3. Yang D, Zhou Q, Labroska V, Qin S, Darbalaei S, Wu Y, et al. G protein-coupled receptors: structure- and function-based drug discovery. Signal Transduct Target Ther. 2021 Jan 8;6(1):1–27.

4. Congreve M, De Graaf C, Swain NA, Tate CG. Impact of GPCR Structures on Drug Discovery. Cell. 2020 Apr;181(1):81–91.

5. Hauser AS, Attwood MM, Rask-Andersen M, Schiöth HB, Gloriam DE. Trends in GPCR drug discovery: new agents, targets and indications. Nat Rev Drug Discov. 2017 Dec 1;16(12):829–42.

6. Insel PA, Sriram K, Gorr MW, Wiley SZ, Michkov A, Salmerón C, et al. GPCRomics: An Approach to Discover GPCR Drug Targets. Trends Pharmacol Sci. 2019 Jun;40(6):378–87.

7. Wootten D, Christopoulos A, Sexton PM. Emerging paradigms in GPCR allostery: implications for drug discovery. Nat Rev Drug Discov. 2013 Aug;12(8):630–44.

8. Syrovatkina V, Alegre KO, Dey R, Huang XY. Regulation, Signaling, and Physiological Functions of G-Proteins. J Mol Biol. 2016 Sep;428(19):3850–68.

9. Bourne HR, Sanders DA, McCormick F. The GTPase superfamily: conserved structure and molecular mechanism. Nature. 1991 Jan 10;349(6305):117–27.

10. Grisshammer R. Understanding recombinant expression of membrane proteins. Curr Opin Biotechnol. 2006 Aug;17(4):337–40.

11. Grisshammer R. Chapter 36 Purification of Recombinant G-Protein-Coupled Receptors. In: Methods in Enzymology [Internet]. Elsevier; 2009 [cited 2024 Feb 28]. p. 631–45. Available from: https://linkinghub.elsevier.com/retrieve/pii/S0076687909630366

12. Wiseman DN, Otchere A, Patel JH, Uddin R, Pollock NL, Routledge SJ, et al. Expression and purification of recombinant G protein-coupled receptors: A review. Protein Expr Purif. 2020 Mar;167:105524.

13. Sarramegna V, Talmont F, Demange P, Milon A. Heterologous expression of G-protein-coupled receptors: comparison of expression systems from the standpointof large-scale production and purification. Cell Mol Life Sci CMLS. 2003 Aug;60(8):1529–46.

14. Shirbaghaee Z, Bolhassani A. Different applications of virus-like particles in biology and medicine: Vaccination and delivery systems. Biopolymers. 2016 Mar;105(3):113–32.

15. Zeltins A. Construction and Characterization of Virus-Like Particles: A Review. Mol Biotechnol. 2013 Jan;53(1):92–107.

16. Nooraei S, Bahrulolum H, Hoseini ZS, Katalani C, Hajizade A, Easton AJ, et al. Virus-like particles: preparation, immunogenicity and their roles as nanovaccines and drug nanocarriers. J Nanobiotechnology. 2021 Feb 25;19(1):59.

17. Weiss ER, Göttlinger H. The Role of Cellular Factors in Promoting HIV Budding. J Mol Biol. 2011 Jul;410(4):525–33.

18. Gao F, Li Y, Decker JM, Peyerl FW, Bibollet-Ruche F, Rodenburg CM, et al. Codon Usage Optimization of HIV Type 1 Subtype C *gag* , *pol* , *env* , and *nef* Genes: *In Vitro* Expression and Immune Responses in DNA-Vaccinated Mice. AIDS Res Hum Retroviruses. 2003 Sep;19(9):817–23.

19. Ho TT, Nguyen JT, Liu J, Stanczak P, Thompson AA, Yan YG, et al. Method for rapid optimization of recombinant GPCR protein expression and stability using virus-like particles. Protein Expr Purif. 2017 May;133:41–9.

20. Jo M, Jung ST. Engineering therapeutic antibodies targeting G-protein–coupled receptors. Exp Mol Med. 2016 Feb 5;48(2):e207–e207.

21. Laeremans T, Sands ZA, Claes P, De Blieck A, De Cesco S, Triest S, et al. Accelerating GPCR Drug Discovery With Conformation-Stabilizing VHHs. Front Mol Biosci. 2022 May 23;9:863099.

22. Guo S, Zhao T, Yun Y, Xie X. Recent progress in assays for GPCR drug discovery. Am J Physiol Cell Physiol. 2022 Aug 1;323(2):C583–94.

23. Park MA, Kim HJ, Kim HJ. Optimum conditions for production and purification of human papillomavirus type 16 L1 protein from Saccharomyces cerevisiae. Protein Expr Purif. 2008 May;59(1):175–81.

24. Bondarev AD, Attwood MM, Jonsson J, Chubarev VN, Tarasov VV, Schiöth HB. Opportunities and challenges for drug discovery in modulating Adhesion G protein-coupled receptor (GPCR) functions. Expert Opin Drug Discov. 2020 Nov;15(11):1291–307.

25. Ma Y, Yue Y, Ma Y, Zhang Q, Zhou Q, Song Y, et al. Structural Basis for Apelin Control of the Human Apelin Receptor. Structure. 2017 Jun 6;25(6):858-866.e4.

26. Yue Y, Liu L, Wu LJ, Wu Y, Wang L, Li F, et al. Structural insight into apelin receptor-G protein stoichiometry. Nat Struct Mol Biol. 2022 Jul;29(7):688–97.

27. Miyauchi K, Marin M, Melikyan GB. Visualization of retrovirus uptake and delivery into acidic endosomes. Biochem J. 2011 Mar 15;434(3):559–69.

28. Joyce JG, Tung JS, Przysiecki CT, Cook JC, Lehman ED, Sands JA, et al. The L1 Major Capsid Protein of Human Papillomavirus Type 11 Recombinant Virus-like Particles Interacts

with Heparin and Cell-surface Glycosaminoglycans on Human Keratinocytes. J Biol Chem. 1999 Feb;274(9):5810–22.

29. Palmer J. Advancing the Development of Macrocyclic Peptide Therapeutics Using High Throughput Mass Spectrometry Approaches [Doctoral Dissertation]. [UW Campus Repository]: University of Washington; 2024.

30. Lavado-García J, Jorge I, Boix-Besora A, Vázquez J, Gòdia F, Cervera L. Characterization of HIV-1 virus-like particles and determination of Gag stoichiometry for different production platforms. Biotechnol Bioeng. 2021 Jul;118(7):2660–75.

31. Mattei S, Tan A, Glass B, Müller B, Kräusslich HG, Briggs JAG. High-resolution structures of HIV-1 Gag cleavage mutants determine structural switch for virus maturation. Proc Natl Acad Sci [Internet]. 2018 Oct 2 [cited 2024 Jan 26];115(40). Available from: https://pnas.org/doi/full/10.1073/pnas.1811237115

32. Keppler A, Gendreizig S, Gronemeyer T, Pick H, Vogel H, Johnsson K. A general method for the covalent labeling of fusion proteins with small molecules in vivo. Nat Biotechnol. 2003 Jan;21(1):86–9.

33. Shin K, Kenward C, Rainey JK. Apelinergic system structure and function. Compr Physiol. 2018 Jan 1;8(1):407–50.

34. O'Dowd BF, Heiber M, Chan A, Heng HHQ, Tsui LC, Kennedy JL, et al. A human gene that shows identity with the gene encoding the angiotensin receptor is located on chromosome 11. Gene. 1993 Dec;136(1–2):355–60.

35. Qin S, Meng M, Yang D, Bai W, Lu Y, Peng Y, et al. High-throughput identification of G protein-coupled receptor modulators through affinity mass spectrometry screening. Chem Sci. 2018;9(12):3192–9.

Chapter 6: Conclusions and Future Directions

6.1 Conclusions

The main objectives of this dissertation project were two-fold; (i) to extensively characterize the impact of two different inotropic agents, the ceramides and the apelins, on the development of cardiac hypertrophy, and (ii) to develop a universal method to screen hits against G-protein coupled receptor targets using APJ as an example. This work expands the existing knowledgebase of novel CVD biomarkers and sheds new light on the mechanisms of the ceramides and apelins in the development of cardiac hypertrophy. Furthermore, this work may improve drug screening against GPCR targets and make it more accessible and less labor intensive than previous assays.

To investigate the impact of ceramides on cardiac hypertrophy, we silenced the ceramide synthase genes responsible for the production of 16:0 ceramide (*CERS5/6*) and 22:0 plus 24:0 ceramide (*CERS2*) in immortalized human ventricular cardiomyocytes. We hypothesized that long-chain ceramide 16:0 would be detrimental to health and lead to the progression of CVD, while very long-chain 22:0 and 24:0 ceramides would be protective based on previous work (1) and provided evidence to support this hypothesis. We demonstrated that knocking down *CERS2* and *CERS5/6* resulted in the reduction of the expected VLC and LC ceramides, as well as the downstream sphingolipid metabolites quantified by mass spectrometry. While examining the transcriptomics response with *CERS2* KD alone, we observed many cellular dysregulations suggestive of a decline in cardiomyocyte health, while *CERS5/6* KD resulted in transcriptional changes that hinted at improved HCM health. With hypertrophy induction using PMA, we further observed exacerbated hypertrophy progression in HCMs with silenced *CERS2*, while *CERS5/6* KD appeared to alleviate some of the observed hypertrophic response. These findings

suggest that expression of *CERS2* and its gene product metabolites, 22:0 and 24:0 ceramides, may be protective against CVD progression, while expression of *CERS5* and *CERS6*, and their metabolite, 16:0 ceramide, may contribute to the progression of CVD.

The next section of this dissertation investigated the impact of the apelinergic system on cardiac hypertrophy. We examined the role of multiple apelin isoforms and APJ, the GPCR through which each apelin exerts its function. We provided evidence that pyroglutamyl-apelin-13 and apelin-17 treatment elicited different pathway changes in cardiomyocytes, indicating that although both apelin isoforms signal through APJ binding, they can assume different roles in cardiomyocyte health.

We created a SNAP-APJ plasmid that resulted in the overexpression of stable and active APJ and overexpressed this receptor in immortalized human ventricular cardiomyocytes. We demonstrated that with the induction of hypertrophy, APJ overexpression reduced the mRNA expression of the hypertrophy biomarker BNP, and transcriptionally, altered many pathways that play crucial roles in the development of CVD. Furthermore, following hypertrophy induction we observed that in the absence of APJ, pyr-AP-13 and AP-17 increased BNP mRNA, but with APJ overexpression, BNP levels declined following both treatments. These findings suggest that both APJ and apelin are necessary to elicit a protective response from the AS. Through this work we identified many pathway changes, but a conclusive role for the AS in these pathways needs to be further defined by knocking down genes in these specific pathways in cardiomyocytes and determining how they affect cell health.

Finally, we concluded this dissertation by presenting a potential universal method for high-throughput GPCR drug screening. As current methodologies require extensive experimental labor and troubleshooting, we hypothesized that we could develop a method which works for

identifying GPCR binders but requires minimal optimization across different receptors. Here we employed the use of virus-like particles to serve as a screening vessel for our GPCR targets. We discussed and validated the development of a purification technique to generate GPCR-VLPs. We further explained how we used these GPCR-VLPs in an ASMS screening assay where we were able to identify positive control binders with two different GPCR systems, APJ and ADORA2A. We concluded this work by testing the limits of this screening method, where we added pyr-AP-13 to a complex mixture of over 2500 peptides and were able to show enriched binding with apelin compared to the peptide library with APJ-VLPs. Taken together, the development of the GPCR-VLP-ASMS technique has the potential to greatly impact drug development, by eliminating the labor-intensive optimization procedures for each GPCR target.

6.2 Future Directions

The discovery nature of this dissertation project laid the groundwork for future research directions aimed towards defining the role that the ceramides and apelins play in CVD progression. Additionally, the work completed in this project is a first step towards addressing issues with current GPCR screening technologies and provides an alternative approach, that could serve as a universal high-throughput screening method to make GPCR binding studies more accessible and less demanding.

Some next steps with respect to the ceramide component of this thesis involve an untargeted lipidomics study. As many of the findings that were discovered with *CERS2* and *CERS5/6* KD were centered around cholesterol biosynthesis and metabolism, it would be interesting to investigate how changes in the 16:0, 22:0, and 24:0 ceramide species altered the cell's global lipidome. Additionally, since we noted that insulin regulation declined in the hypertrophic response due to either *CERS2* or *CERS5/6* KD, it would be worthwhile to explore

the role specific sphingolipids play in insulin resistance. Finally, due to the increase in cell death observed with both *CERS2* and *CERS5/6* KDs, the role of ceramides in the cardiac cell cycle needs to be further investigated. The clear findings and importance of this work suggest that more effort is needed to characterize the role that VLC and LC ceramide species play *in vivo* in both the development and progression of cardiovascular disease.

In order to fully elucidate the role the AS plays in cardiomyocyte homeostasis and cardiac hypertrophy development, additional work needs to be allocated to study how APJ overexpression and treatment with various apelins alter specific forms of cell death, such as ferroptosis and apoptosis. To understand the role pyr-AP-13 plays in the hypertrophy response, additional experimentation should be completed utilizing pyr-AP-13 treatments aside from the rolling treatment used in this project. If APJ activation could be increased through different apelin treatment strategies and more gene changes could be elicited, this would open the door to performing a cluster analysis to determine pathway change directionality. Also, since it appears that pyr-AP-13 treatment alters cholesterol metabolism, while AP-17 treatment alters pathways related to eicosanoids, it would be very interesting to study the global lipidome changes due to apelin treatment. Since the apelin species collectively are known to influence obesity and play roles in lipolysis and fatty acid oxidation (2,3), it would be intriguing to explore how treatment with the different apelin isoforms leads to changes in lipid species within the cell as well as lipid storage in lipid droplets. Additional work should be completed *in vivo* to further define the role of the different apelin isoforms in cardiac health. Both preventative and rescue experiments with the different apelin isoforms should be completed in mouse models. Mice should be dosed with the apelin isoforms prior to the initiation of a myocardial infarction and disease severity should be assessed over time to see if apelin treatment could be used as a preventative strategy to

counter CVD development. In conjunction with this, rodent models exhibiting different versions of CVD, with and without changes in ejection fraction, should be dosed with the different apelin isoforms to elucidate the potential protective mechanisms of the different apelins. Completion of this work would open the door to potential structure activity relationship studies between the different apelin-APJ interactions, to better mimic the desired signaling response with future CVD therapies targeting the AS.

Finally, future efforts could go into increasing the yield and efficiency of making GPCR-VLPs. Experimentation should continue generating vesicles with viral proteins beyond HIV-1 Gag that could help increase the yield of GPCR containing vesicles. The current GPCR-VLP method could undergo further testing with other GPCRs, or ion channels, to test if VLPs could be used as a vessel to identify ligand binding for other complex membrane proteins. Additionally, this method should be used in the future to characterize a large compound library screen with compounds designed to bind to APJ, or other interesting GPCR targets.

References

1. Lemaitre RN, Jensen PN, Hoofnagle A, McKnight B, Fretts AM, King IB, et al. Plasma Ceramides and Sphingomyelins in Relation to Heart Failure Risk: The Cardiovascular Health Study. Circ Heart Fail. 2019 Jul;12(7):e005708.

2. Hu H, He L, Li L, Chen L. Apelin/APJ system as a therapeutic target in diabetes and its complications. Mol Genet Metab. 2016 Sep 1;119(1–2):20–7.

3. Li C, Cheng H, Adhikari BK, Wang S, Yang N, Liu W, et al. The Role of Apelin–APJ System in Diabetes and Obesity. Front Endocrinol. 2022 Mar 9;13:820002.

Appendix I: Efforts towards developing properly folded APJ excised from mammalian cells and optimization for binding assay conditions

This appendix will detail the various approaches attempted to isolate APJ from mammalian cells in its native folded state. In order to attach APJ to solid support magnetic beads and utilize the protein in affinity selection mass spectrometry binding assays, we initially believed we needed a method to remove APJ from its native membrane bilayer. The complexities of removing GPCRs from their native environment and purifying them in a way that enables correct protein folding is discussed in great detail in **Chapter 5**. In this appendix, I will focus on important experiments for the ASMS assay validation and discuss in detail the different purification attempts made to generate correctly folded APJ. I will first discuss the validation of our SNAP-APJ plasmid covalently binding to SNAP magnetic beads and why this was a crucial first step. I will then present each APJ purification attempt in detail leading up to our decision to invest in utilizing VLPs as a host environment for natively folded APJ. At that point, I will break down experiments that were conducted and different purification protocols that were attempted, in order to minimize overlap with future troubleshooting. Overall, this appendix will outline the difficulties encountered in attempting to remove APJ from the plasma membrane as well as demonstrate how the binding assay was optimized and why it is run this way now.

I.1 Successful binding of SNAP-APJ to SNAP magnetic beads

For reasons discussed in **Chapter 5**, we chose to utilize HEK293T cells as our protein expression system. As our goal was to be able to conduct an ASMS HTS method with APJ and a library of novel designed agonists, the first step to developing this method was to ensure that the tagged-APJ covalently attached to the corresponding magnetic beads, as expected. To begin to address this, HEK293T cells were transfected with either SNAP-APJ plasmid or Empty-SNAP

vector in 10 cm petri dishes, using the optimized transfection ratios discussed previously in **Chapter 5, Section 5.2.3.A**. The cells were harvested by scraping and lysed using RIPA buffer (Thermo Fisher Scientific, #J63306.AK; Waltham, MA) supplemented with Halt Protease and Phosphatase Inhibitor Cocktail (Thermo Fisher Scientific, #78440; Waltham, MA). The narrowest part of the pipette tip was cut off to make the pipette tip bore larger, and decrease the stress placed on the cells as well as the surface proteins. The samples were then manually disrupted by being pipette up and down 50 times before being placed in the microcentrifuge at 4°C and centrifuged at 16,100 x *g* for 10 min.

While the samples were spinning, 80 µL SNAP-capture magnetic beads were added to two separate tubes and equilibrated 3x with RIPA buffer. After the completion of the centrifugation, 125 µL of both the SNAP-APJ and Empty-SNAP lysates were added to their respective equilibrated SNAP beads and placed on the rotating tube mixer at 4°C overnight. The magnetic beads were captured for all subsequent steps and the supernatants were collected in order to test for unwanted APJ wash off. Unless otherwise noted, samples were placed on the room temperature rotating tube mixer for 1 min before the supernatant was collected and the next 1 mL incubation was initiated. The post-loading lysate was collected and three subsequent wash steps with RIPA buffer were initiated, followed by three running buffer (50 mM NH_4HCO_3 + 75 mM KCl, pH 8) incubations. Next, 50 µL of a high pH elution buffer (0.5 M NH_4OH, pH 11-12) was added to the beads to try to strip APJ off. The elution buffer was continuously flicked for 2 min, before the supernatant was collected for testing. This elution procedure was repeated three times, before a fourth and final elution attempt was made with the addition of 100 µL elution buffer and a 15 min room temperature incubation period. The collected supernatants were evaporated utilizing the SpeedVac vacuum concentrator and resuspended in 30 µL DI water. A

western blot with these samples and an anti-APJ antibody (Proteintech, #20341-1-AP; San Diego, CA) confirmed that APJ did not elute from the beads with any wash or elution step and a reduced band in the post-loading lysate led us to believe we overloaded the SNAP beads with APJ (**Figure I.1**). Furthermore, this experiment confirmed that APJ is not expressed in HEK293T cells, demonstrated by a lack of APJ bands in the empty vector lysate. Overall, this experiment gave confidence to using SNAP-capture magnetic beads as our insoluble solid support for the ASMS workflow.

I.2 First binding assay method attempt: Lysing overexpressed APJ from HEK293T cells

Our first attempt at utilizing APJ removed from the native bilayer in a binding assay repurposed the lysate left over from the SNAP magnetic bead validation. To 40 µL equilibrated SNAP beads, 60 µL of the APJ and empty vector lysates were added to respective tubes in duplicate and incubated at room temperature on the rotating tube mixer for 1h. A 500 µL PBS wash step was conducted three times, before the beads were washed once with 500 µL blocking buffer (0.1% (1mg/mL) BSA in PBS) and placed on the rotating tube mixer for 1 min. The samples were then introduced to 450 µL of a 16 µM solution with APJ agonist pyr-AP-13 (Cayman Chemical, #15590; Ann Arbor, MI) in blocking buffer. This agonist incubation was placed on the rotating tube mixer at room temperature for 1h, before samples were washed three times with 500 µL ice cold PBS. To elute pyr-AP-13 off the beads, two 5 min elutions were commenced with 100 µL elution buffer (6 M guanidine hydrochloride (GnHCl), 200 mM phosphate, pH 6.8 in PBS). Eluants were collected and C18 tips (Sigma-Aldrich, #ZTC18S008; St. Louis, MO) were used according to the manufacturer's recommendations to concentrate and clean up the samples. Following LC-MS/MS analysis, there was no enriched binding detected

with pyr-AP-13 in the APJ lysate compared to the empty vector control, leading us to believe that under these conditions, APJ was not folded correctly.

I.3 Second binding assay method attempt: Creating micelles with HEK293T lysates

Historically, purifying functional GPCRs away from their native bilayers has been met with the most success when non-ionic surfactants and stabilizing agents are used to make up the buffers. For this reason, we attempted to try a few different buffers to test if we achieve enriched pyr-AP-13 binding to APJ lysates. N-dodecyl-β-D-maltoside (DDM) supplemented with a cholesterol mimicking detergent like cholesteryl-hemisuccinate (CHS), and glycerol to help increase receptor stability is a commonly used combination to get Class A GPCRs correctly folded (1,2), therefore, we decided to implement this as our Buffer #1. In Buffer #2, we replaced DDM with DMPG (1,2-dimyristoyl-*sn*-glycero-3-PG) because DMPG is thought to aid in stabilizing membrane proteins (3). Buffer #3 consisted of a 1:1 mixture of Buffer #1 and Buffer #2. All buffers were prepared fresh in 50 mM HEPES supplemented with 500 mM NaCl, 20 mM KCl, and 15% glycerol, pH 7.5. Buffers were forced through an 18-gauge needle to break up large micelles and create a more uniform mixture before being added to the samples.

Buffer #1: 10 mM DDM (Cayman Chemical, #16494; Ann Arbor, MI) and 2 mM CHS (Cayman Chemical, #25698; Ann Arbor, MI). CHS was dissolved in DMSO, bringing the total organic 0.537%. This buffer became foamy like a detergent.

Buffer #2: 2 mM DMPG (Cayman Chemical, #15085; Ann Arbor, MI) and 2 mM CHS. DMPG and CHS were dissolved in DMSO, bringing the total organic to 0.813%. This buffer did not foam up.

Buffer #3: 50:50 mix of Buffer #1 and Buffer #2.

New lysates were created from transfected HEK293T cells and samples underwent a BCA and western blot analysis to validate APJ expression. Lysates were added so protein amount exceeded the binding capability of the equilibrated SNAP beads and placed on a rotating tube mixer at 4°C overnight. For each buffer above, 500 µL was added to the loaded beads, in duplicate for both APJ and empty vector lysates. The samples were then allowed to equilibrate at 4°C in the rotating tube mixer for 2.5h. Samples were washed with buffer 2x, then 500 µL blocking buffer (respective buffer + 0.1% BSA (1mg/mL)) was added to the sample and allowed to mix for 1 min, before initiating the agonist incubation. The agonist pyr-AP-13 was added to blocking buffer to compose a 16 µM solution, and 450 µL of this was added to each sample and allowed to equilibrate on the rotating tube mixer for 1h at room temperature. The samples were then washed three times with 300 µL ice cold buffer and eluted twice with 100 µL 6 M GnHCl, warmed to 45°C. During each elution step, samples were placed on the rotating tube mixer for 5 min. These samples were very dirty due to the addition of all the different surfactants, so eluants were cleaned up with C18 tips. There was no observed enriched pyr-AP-13 binding to APJ compared to control lysates with any of the different buffer conditions.

Ultimately, we decided there were too many variables that could be altered with the generation of micelles, so decided to look for different methods to achieve correctly folded APJ. With enriched pyr-AP-13 binding being our only readout, it was a huge experimental burden to alter the variables with no clear way to determine if altering one concentration in the buffer composition was beneficial as opposed to the other. That said, we did consider increasing the DMPG concentration and including a 15 min preincubation with alkylating agent iodoacetamide. Additionally, this method could be expanded upon by utilizing the dounce homogenizer with a hypotonic buffer like HEPES and altering the micelle buffer incubation period.

I.4 Third binding assay method attempt: Dialysis with HEK293T lysates

Our next purification attempt was centered around utilizing dialysis to generate correctly folded APJ. Fresh HEK293T lysates were generated and 100 µL of these lysates were added to mini slide-a-lyzer 20K MWCO dialysis units (Thermo Fisher Scientific, #69590; Waltham, MA) in duplicate for each experimental condition and each sample type (APJ and empty vector lysates). The following folding buffer was utilized in this set of experiments: 25 mM HEPES supplemented with 500 mM NaCl in DI water and filtered, pH adjusted to 7.5, then supplemented with 5% glycerol, 0.01% DDM, 0.002% CHS, and 200 mM imidazole. For this experiment, when apelin was supplemented into the media, we are referring to a solution containing 2.5 µM FITC-apelin-13 (FITC-AP-13, an apelin with a fluorescein isothiocyanate label), unless otherwise noted. Microcentrifuge tubes were filled to the top with folding buffer supplemented with apelin and dialysis units containing the lysates were placed in a way to minimize bubbles between the membrane and buffer. Samples were set on the rocker at 4°C and allowed to equilibrate overnight. In the morning, the bottom buffer was replaced with new apelin supplemented folding buffer and placed on the rocker at room temperature for 4h. At this point, we concluded the apelin sample priming, and the folding buffer was replaced for an additional 4h treatment, with no respective apelin treatment. The folding buffer was then exchanged for a final time, sans apelin treatment, and placed back on the rocker in the 4°C box overnight.

At this point, we were hopeful that the buffer combination and early priming with apelin promoted APJ into its correctly folded state and initiated incubations with apelin to be collected for subsequent analysis. The following morning, the folding buffer in the microcentrifuge tube was replenished, and FITC-AP-13 was added to the top of the membrane with the lysates to bring the total concentration of FITC-AP-13 to 2.5 µM. These samples were left to dialyze for 4h

on the room temperature rocker, where aliquots were collected from both fractions and fluorescence was analyzed on a BioTek Synergy HTX plate reader (Aligent; Santa Clara, CA). Here we determined that the FITC-AP-13 was actuality not dialyzing, so switched dialysis devices to a Rapid Equilibrium Dialysis (RED) Plate (Thermo Fisher Scientific, #90006; Waltham, MA). The lysates and folding buffers were transferred into the RED inserts and allowed to dialyze at 37°C for 4h. The FITC-AP-13 was found in both fractions collected, suggesting that dialysis was occurring within the RED plates, but there were no observed changes in fluorescence between the APJ lysates and the empty vector controls. In the future, the slide-a-lyzer dialysis units should be avoided for this purpose since they were not sufficient in promoting dialysis, but the RED plates can potentially be further optimized and used to help with protein folding and binding assays.

In parallel to running dialysis with these HEK293T lysates, we performed a binding assay with SNAP beads. Lysates were added to equilibrated SNAP beads and then run through the same buffer regimen as the dialysis units. The binding assay was run as previously described, but with a 1.25 μM pyr-AP-13 + 1.25 μM AP-13 incubation. There were no observed changes in binding enrichment following LC-MS/MS analysis between the APJ and empty vector lysates.

I.5 Utilizing VLPs for native GPCR folding

At this point, we took a step back to try and reconsider our previous assumption that it was necessary to remove APJ from the native lipid bilayer. As we had exploited many common methods to get APJ correctly folded with no success, we sought to find a method that could be more universal with all GPCRs, not just APJ. Each experiment was very labor intensive, and we only had one readout that took place at the conclusion of a very long string of experimental procedures – observed enriched agonist binding. With the binary yes or no to enriched binding,

there was no way for us to generate experimental evidence to support that any of these specific procedures was leading us closer to having correctly folded APJ. This lack of evidence to help guide experimental changes was neither efficient nor encouraging, so we went back to the drawing board to conjure up some other ideas.

These complications led us down the path of testing out VLPs as a vessel for APJ, eliminating the need to remove the GPCR from the plasma membrane. **Chapter 5** contains information on the optimization process for utilizing both Gag-protein and APJ plasmids in HEK293T cells to achieve co-overexpression. In this portion of the appendix, I will discuss crucial experiments that guided our binding assay experimental protocol with the purpose of ensuring that any future optimization does not include backtracking.

I.5.1 Important notes learned from VLP purification attempts

Flask size does matter. Initially, all VLP generation experiments were completed in T75 flasks. Purification attempts in T75 flasks led to zero success, so for all VLP experiments, T175 flasks or larger should be used to ensure sufficient VLP production. Also, 10 μg/mL heparin should be supplemented into the media to avoid VLP reentry into the cells. We noted a significant increase in cell viability and VLP concentration following the addition of heparin to our VLP batches.

An additional centrifugation step removes protein and lipid contaminants, leading to cleaner samples. The centrifugation steps underwent significant alteration during the optimization process, and although not all steps are necessary in order to observe enriched binding of agonists compared to controls, implementation of the three steps helped increase specific protein concentration as well as decrease western blot issues with loading due to hydrophobicity in the samples.

1st spin: 300 x *g* for 5 min

2nd spin: 2,000 x *g* for 20 min

3rd spin: 16,000 RPM for 2h, 4°C, 45 Ti rotor

4th spin (optional, microcentrifuge, resuspend in smaller volume to get desired concentration): 16,000 RPM for 45 min

The 1st spin step is crucial for further experimentation. This spin is in place to remove large cell debris present after media harvest. The 2nd spin step was a late experimental addition that made a significant difference in sample composition. Before the addition of this spin, we were having issues with "sample peaking" while running gel electrophoresis, likely due to the high lipid content within the samples (**Figure I.2A**). This spin step is responsible for removal of additional protein and lipid contaminants, which significantly increased our specific protein yield (**Figure I.2B**). The 3rd spin step was extensively looked at during initial experiments. This spin was performed at many different time points ranging from 45 min to 18h. Ultimately, at 45 min it appears VLPs are still congregating in the pellet, but the pellet is very loose, and for that reason, we decided to implement a 2h spin to minimize sample loss while decanting and resuspending.

We initially attempted to purify the VLPs with an ammonium sulfate precipitation protocol (4,5). We utilized 45% saturating ammonium sulfate, but following the spin steps, observed no bands on a western blot. We repeated this purification with a new batch of VLPs and added SNAP beads to both the pellet and the entire supernatant but observed no change in pyr-AP-13 binding, suggesting efforts should be focused on investigating other purification procedures.

Next, we tried to purify the VLPs using a sucrose gradient (6). Following the ultracentrifugation step, we resuspended the pellet in 11 mL TNE buffer (Quality Biological,

#351-302-101; Gaithersburg, MD). Gently, the sucrose composition was layered as so: 2 mL 65% sucrose (3.25 g / 1.75 mL TNE), 4 mL 20% sucrose (2 g / 8 mL TNE), and the 11 mL resuspended sample. The sample was then spun down at 24K RPM for 6h at 4°C in the 50.2 Ti rotor. Following ultracentrifugation, the top 13-14 mL were carefully discarded and the buffy white layer in the center containing the VLPs was moved to a new tube (next 2-3 mL). The sucrose in this layer was diluted with 13 mL TNE buffer and ultracentrifuged at 35K RPM for 6h at 4°C. This sample was used for ns-EM, but the sucrose altered the stain quality and resulted in blurred micrographs. Should the need arise, I believe this method could be successful in other aspects, but I would recommend utilizing the small-scale purification discussed by McGinnes and Morrison (6).

I.5.2 Important experiments that shaped the binding assay protocol

Conditions were optimized for agonist concentration and incubation time. Agonist concentrations from 250 nM to 16 μM were utilized in various binding assays. We ultimately chose a 1 μM agonist concentration because we observed reliable peak shapes in day-to-day experiments. Additionally, we originally tested out a 5-, 25-, and 60-min agonist incubation period. With the first attempt, we saw larger changes with the 25 min incubation time point, but with more replicates and further experimentation, observed more consistent results following the 60 min agonist incubation time, hence used this incubation time moving forward.

We also extensively altered the binding assay, but the finalized protocol can be found in **Chapter 5, Section 5.2.7**. Notably, I would like to touch on two important steps, the first being that constant agitation is crucial during elution. We utilized finger flicking or tapping to ensure the beads were not settling to the bottom and were immersed in the elution buffer. Secondly, we began this process by cleaning up our samples with C18 tips but ended up losing too much of our

analyte and introducing significant variability. Instead of continuing down this path, we experimented with the elution buffer concentrations and volumes.

Finally, I would like to mention that following transfection with the ADORA2A plasmid and Gag, we did perform western blots and RT-qPCR to ensure overexpression of ADORA2A. ADORA2A provided a second GPCR test for our VLP method, as well as a better negative control to compare agonist binding against APJ. Further optimization and results with the ADORA2A and APJ are found in **Chapter 5**.

Figures

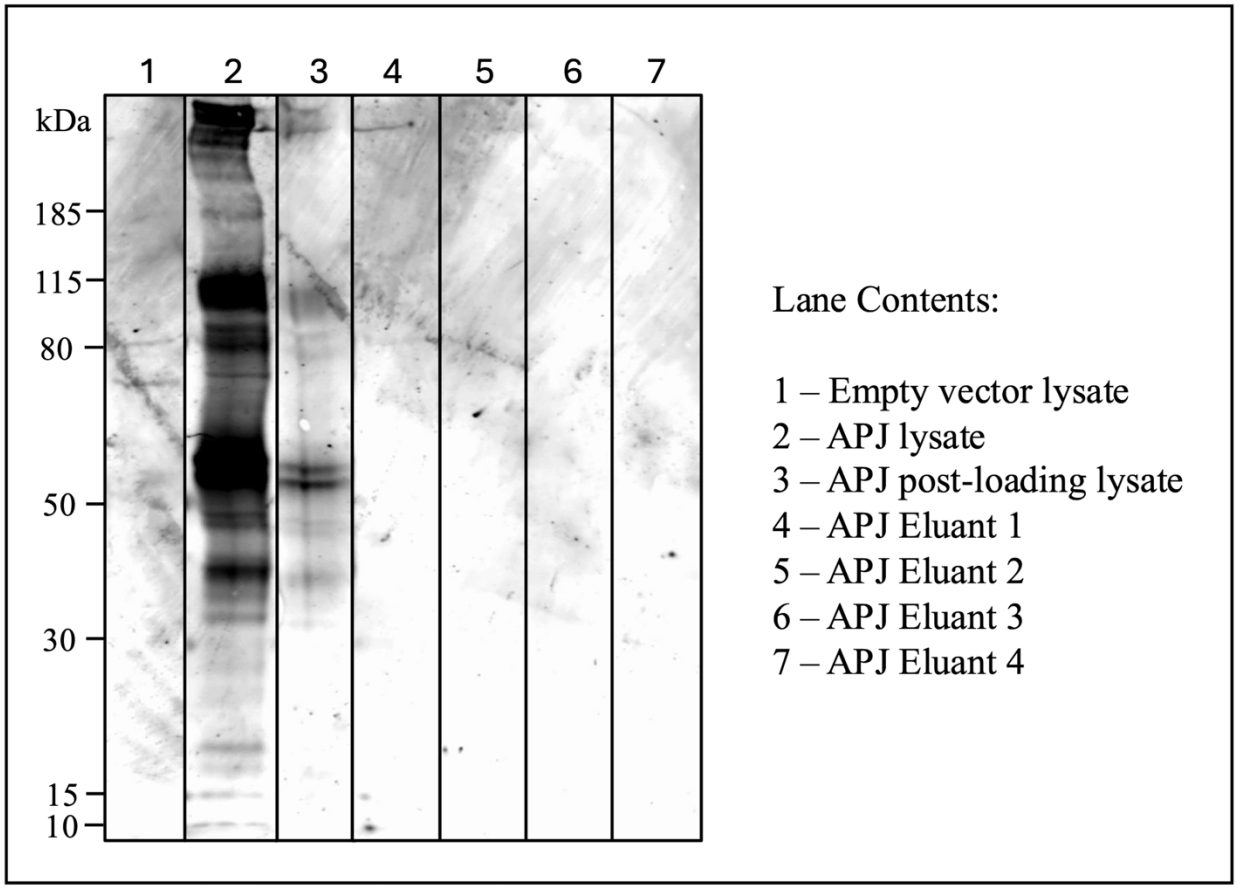

Figure I.1. Validation of the use of SNAP magnetic beads.

Composite western blot using an anti-APJ antibody with HEK293T lysates following an attempt to strip SNAP-APJ off the SNAP-capture beads.

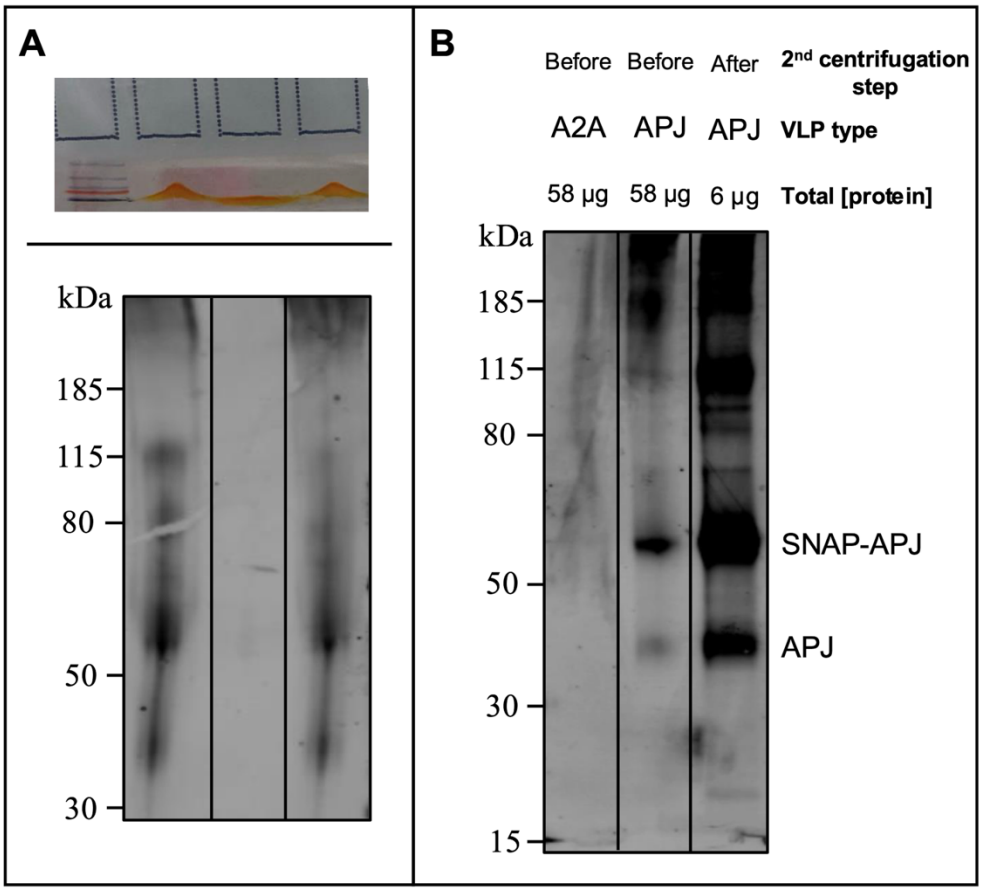

Figure I.2. The importance of the 2nd centrifugation step.

(**A**) "Sample peaking" observed before the implementation of the 2nd centrifugation step, and how that affects western blot quality. (**B**) Visualization of the increased specific protein content with VLP batches after the additional 2nd centrifuge step was added to the protocol. Western blots were incubated with an anti-APJ antibody.

References

1. Grisshammer R. Chapter 36 Purification of Recombinant G-Protein-Coupled Receptors. In: Methods in Enzymology [Internet]. Elsevier; 2009 [cited 2024 Feb 28]. p. 631–45. Available from: https://linkinghub.elsevier.com/retrieve/pii/S0076687909630366

2. Wiseman DN, Otchere A, Patel JH, Uddin R, Pollock NL, Routledge SJ, et al. Expression and purification of recombinant G protein-coupled receptors: A review. Protein Expression and Purification. 2020 Mar;167:105524.

3. Lyukmanova EN, Shenkarev ZO, Khabibullina NF, Kopeina GS, Shulepko MA, Paramonov AS, et al. Lipid–protein nanodiscs for cell-free production of integral membrane proteins in a soluble and folded state: Comparison with detergent micelles, bicelles and liposomes. Biochimica et Biophysica Acta (BBA) - Biomembranes. 2012 Mar;1818(3):349–58.

4. Schagen FHE, Rademaker HJ, Rabelink MJWE, Van Ormondt H, Fallaux FJ, Van Der Eb AJ, et al. Ammonium sulphate precipitation of recombinant adenovirus from culture medium: an easy method to increase the total virus yield. Gene Ther. 2000 Sep 1;7(18):1570–4.

5. Spice AJ, Aw R, Bracewell DG, Polizzi KM. Synthesis and Assembly of Hepatitis B Virus-Like Particles in a Pichia pastoris Cell-Free System. Front Bioeng Biotechnol. 2020 Feb 14;8:72.

6. McGinnes LW, Morrison TG. Newcastle Disease Virus-Like Particles: Preparation, Purification, Quantification, and Incorporation of Foreign Glycoproteins. Current Protocols in Microbiology [Internet]. 2013 Oct [cited 2023 Jan 10];30(1). Available from: https://onlinelibrary.wiley.com/doi/10.1002/9780471729259.mc1802s30